The study of the production of heavy flavour muons as a function of charged-particle multiplicity in proton-proton collisions at 8 TeV with ALICE at the LHC.

Author : **Sibaliso Mhlanga**

A thesis submitted in partial fullfilment of the requirements of
the Master of Science Degree in the Department of Physics,
University of Cape Town.

***Supervisor* :**
Prof. J. Cleymans
University of Cape Town
Private Bag X3
7701
Rondebosch

***Co-supervisor* :**
Dr. Z. Buthelezi
Ithemba LABS
PO Box 722
7129
Somerset West

2015

Declaration

I know the meaning of plagiarism and hereby declare that this thesis is my own work and effort and that it has not been submitted anywhere for any award. Where other sources of information have been used, they have been acknowledged.

Signature:...

Date:...

Abstract

ALICE (A Large Ion Collider Experiment) is a detector designed and optimized to study ultra relativistic heavy-ion collisions in which a hot, dense and strongly interacting Quantum Chromodynamics (QCD) medium called the Quark Gluon Plasma (QGP) is created. ALICE also studies proton-proton collisions both to test for pertubative QCD (pQCD) theories and as reference for comparison with heavy-ion collisions. ALICE measures hadrons, leptons, and photons up to very high transverse momentum (p_T), up to ∼100 GeV/c. It consists of a central barrel which covers a rapidity of $|\eta| < 0.9$ and a Muon Spectrometer which covers the forward rapidity, $-4 < \eta < -2.5$. The Muon Spectrometer measures dimuons from the decay of quarkonia (charm-anti-charm ($c\bar{c}$) e.g. J/Ψ), as well as single muons from heavy flavours (e.g. charm (c) and bottom (b) hadrons) and electroweak bosons ($W^{\pm}$, Z^0), which are tools for studying QGP as well as the initial conditions of the collision.
In this thesis the production of heavy flavours is measured via the contribution of their muonic decays to the inclusive p_T-differential muon yield, reconstructed with the Muon Spectrometer and studied as a function of charged-particle multiplicity in proton-proton collisions at 8 TeV centre-of-mass energy. The charged-particle multiplicity is measured in the central barrel. The aim of the study is to investigate the role of multi-parton interactions in the production of heavy quarks, particularly heavy flavour.

Contents

Acknowledgements

I would like to convey my warmest gratitude firstly to my supervisor, Dr. Zinhle Buthelezi, for her excellent guidance, caring patience, and providing me with an excellent atmosphere for doing research. Am grateful for the encouragement and advice she has provided from the start until the end of my MSc. Her careful editing contributed enormously to the production of this thesis. I would also like to thank Professor Jean Cleymans for supervising me and for the comments and contributions to this thesis.

Secondly, I am thankful to Dr. Francesco Bossù for the guidance and generous contribution of knowledge and experience, for the valuable comments and encouragement. I thank Dr. Massimiliano Marchisione for the valuable thesis corrections and contribution to the analysis. I would also like to thank Mr Kgotlaesele Senosi (PhD Candidate) for the enlightening and joyful discussions about social life, science and most importantly his invaluable help during the use of the analysis software and code.

Thirdly, I would like to thank the Natinal Research Foundation (NRF) for partly sponsoring my research. Also SA-CERN for sponsoring the valuable trips to CERN and the schools and conferences I attended that enhanced my knowledge.

Many friends have helped me stay sane. Their support and care helped me overcome setbacks and stay focused on my studies. I greatly value their friendship and I deeply appreciate their belief in me.

Most importantly, none of this would have been possible without the love and patience of my family. My family, in particular, my mom and dad to whom this thesis is dedicated, have been a constant source of love, concern, support and strength all these years. I would like to express my heart-felt thanks.

Now unto the King eternal, immortal, invisible,
the only wise God, be honour and glory for ever and ever.
Amen. ....1 Tim 1:17

List of Figures

List of Tables

Chapter 1

Introduction

At large baryon densities[1] ($\simeq$ 0.5 - 2 baryons/fm^3) and/or extreme temperatures ($\simeq$ 2 x 10^{12} K), nuclear matter is expected to undergo a phase transition to a state called the quark-gluon plasma (QGP), a Quantum Chromodynamics[2] - QCD medium. In this state fundamental constituents of matter, the quarks and gluons are no longer confined to hadrons[3] instead they move free over the whole high density system. This state is known as de-confinement. Besides this de-confinement, chiral symmetry is expected to be restored in a QGP, which means that quark masses will approach zero. Under such extreme conditions the known structure of matter, where the basic constituents are nuclei and electrons, is disrupted and it is more appropriate to treat quarks as basic degrees of freedom.

At the Large Hadron Collider (LHC) [LHC01], ALICE (A Large Ion Collider Experiment) [ALI01] is a heavy-ion detector designed to study the physics of strongly interacting matter at extreme energy densities, where the QGP is expected to be formed. ALICE also studies proton-proton (pp) collisions as a comparison to heavy-ion (lead-lead (PbPb) and proton-lead (pPb)) collisions. Deviations in the production of quantities measured in pp and pPb collisions as compared to PbPb collisions can serve as probes of the differences between the colliding systems. Therefore, if no QGP is created in pp and pPb collisions [AB+05], then observed differences are useful for directly probing the characteristics of the QGP formed in PbPb collisions. Regardless, of whether or not a QGP is formed in pp collisions, pp measurements do have a full physics motivation. At LHC energies pp collisions are comparable to heavy-ion collisions, e.g. gold-gold (Au-Au) at RHIC [JPL15]. Since the LHC explores an unprecedented energy regime where new physics could be observed, pp collisions are an important part of the program as they give a baseline and reference for pPb and PbPb collisions at these energies. Furthermore, at the LHC, pp collisions are useful for understanding the background [AB+06] in rare phenomena (high transverse momentum (p_{T}) events) such as the search for the Higgs and Super Symmetry (SUSY) [AB+07]. In these events the background is mainly charged particles from minimum bias, [4] pile-up events and low p_{T} events (underlying events[5]) occuring simultenously with high-p_{T}

---

[1] The density of protons and neutrons (which are baryons) minus the density of antibaryons.

[2] Theory of strong interactions.

[3] Composite particles made of quarks and/or anti-quarks and gluons e.g. protons.

[4] Minimum bias refers to the trigger designed not introduce a bias towards events containing high-p_{T} particles as well as events containing many particles.

[5] Underlying events are background to events with an identified hard scatter (actual events of interest).

events. Pile up events refer to multiple minimum bias interactions in the same bunch crossing.

There are four major experiments around the LHC ring, namely, ATLAS (A Toroidal LHC Apparatus) [ATL01], CMS (Compact Muon Spectrometer) [CMS01], LHCb (LHC-beauty) [LHC98] and ALICE [ALI01]. Figure 1.1 shows the pseudorapidity[6] coverage of these experiments. It can be seen that the ALICE detector is placed in the kinematic region which is complementary to these other experiments. In particular, it complements both CMS and ATLAS at midrapidity ($|\eta| < 2$), close to the interaction point where most of the charged particles are measured and complements LHCb at forward rapidity ($-4 < |\eta| < -2.5$), where the ALICE Muon Spectrometer is located and where the measurement of muons takes place. At this rapidity region we will be sensitive to quark Parton Distribution Functions (PDFs) at high momentum transfer Q^2 ($Q \approx M_{b/c}$). Therefore, we will be able to probe small Bjorken-x values, where x is the fraction of the beam particle momentum carried by a parton involved in hard scattering, it is given by 1.1

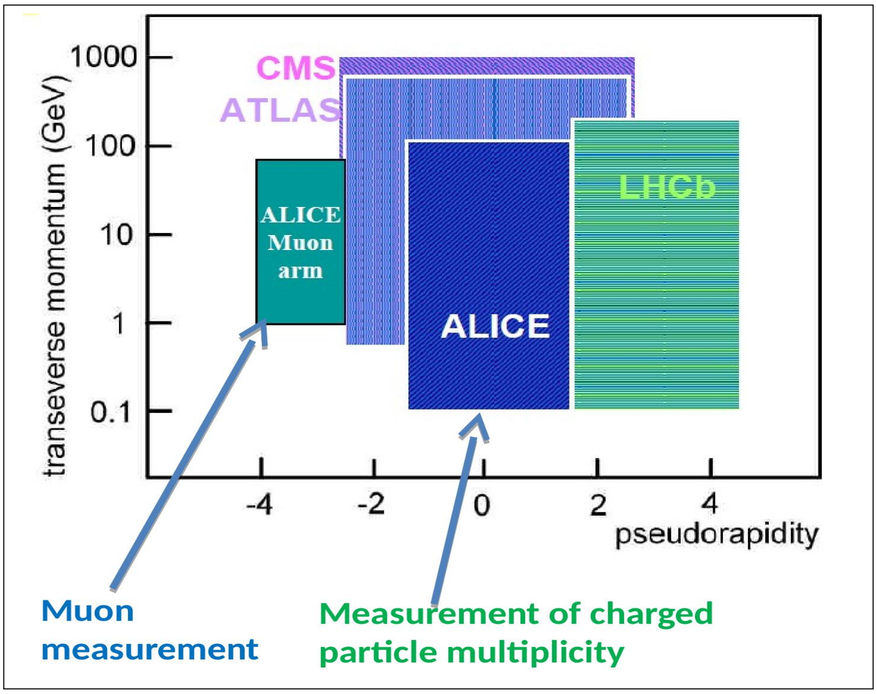

Figure 1.1: The pseudorapity coverage of the four LHC experiments.

$$x_{i,j} = \frac{M_{b/c}}{\sqrt{s_{NN}}} e^{\pm y} \tag{1.1}$$

where $\sqrt{s_{\mathrm{NN}}}$ is the center-of-mass energy, $x_{\mathrm{i,j}}$ is the x of the two partons annihilating to form a particle of mass $M_{\mathrm{b/c}}$ and y is the rapidity.

According to [ALI010], ATLAS measurements for electrons and muons from heavy flavour in pp collisions at 7 TeV are consistent with pQCD theoretical calculations [ALI012]. The electrons and muons are reconstructed at midrapidity, hence it would be

---

[6] Pseudorapidity, η=-ln[tan($\frac{\theta}{2}$)], describes the angle of the particle relative to the beam axis.

interesting to measure muons from heavy flavour in the forward rapidity and compare with models.

In this regard, the ALICE detector is best suited for the measurement of charged particles with respect to other LHC experiments and is a suitable instrument for studying pp collisions at the LHC.

ALICE has been taking data since the start of the LHC in 2009. To date, it has published several papers on multiplicity[7] and on the production of heavy quarks. Since the focus of thus work is studying the correlation of heavy-flavour production with charged-particle multiplicity measurements, therefore in the following we will give a review of studies that have been conducted by ALICE and other LHC experiments.

1.1 Charged-particle multiplicity

Whenever entering a new energy regime, in particular the unprecedented energy domain of the LHC, it is crucial to measure the global characteristics of the collisions. The measurement of multiplicity of the produced particles in an acceptance of a given detector provides essential information about the global characteristics of a collision. In high energy pp collisions the multiplicity of charged particles is a key quantity to characterize the hadronic final state[8].

At LHC energies multiplicity measurements are of importance as they are used to test the ability of theoretical models in particular, those incorporated in Monte Carlo event generators such as PYTHIA [PST13] and PHOJET [PRJ96], to reproduce data at these energies. Event generators are used to simulate particles produced in collisions. They combine theoretical calculations such as perturbative QCD (pQCD) with phenomenological approaches. The properties of the phenomenological models are controlled by a large number of free parameters.To simulate high-energy proton-protons collisions, interactions involving a large momentum transfer (hard processes), are calculated using pQCD, while low momentum transfer interactions (soft processes) are calculated using different phenomenological approaches. Obtaining an accurate simulation of the low momentum component is particularly important because the typical pp collision at the LHC include multi-parton[9] interactions (MPI), which are soft processes. Comparing the multiplicity measurements at LHC energies with predictions of theoretical models allows a better tuning of these models to accurately simulate minimum bias as well as underlying events. The charged-particle multiplicity of these events are used to study the properties of soft interactions. The typically measured distributions are the number of charged particles per event, N_{ch} , the pseudorapidity density, i.e. the number of charged particles as a function of the pseudorapidity, $\frac{dN_{\mathrm{ch}}}{d\eta}$, and as a function of the transverse momentum, $\frac{dN_{\mathrm{ch}}}{dp_{\mathrm{T}}}$, and the average momentum as a function of the number of charged particles.

As mentioned above ALICE has published several papers on multiplicity studies

---

[7] The number of charged particles produced in a pp collision.

[8] Hadrons produced in an event before the decay into charged particles occurs.

[9] Multiple quark and gluon collisions in the same pp collision.

e.g. [RIG13, COL06, A+05, HFP07]. For example, in [RIG13], it was observed that at the LHC the highest charged-particle multiplicities are comparable with those in heavy-ion collisions at lower energies, e.g. UA5 measurements [HFP12] at the same energy shown in Figure 1.2. Also it was observed that the charged-particle multiplicity increases with increasing collisional energy. However, none of the investigated model predictions described the average multiplicities and the multiplicity distributions well, i.e. they underestimated the increase of the average multiplicity seen in the data at different collision energies. In addition, data obtained by ALICE were found to be consistent with those obtained by CMS [HFP13] and when compared to various models for which they provide further constraints. The ATLAS Collaboration [ATL01] also measured the charged particle multiplicity [ALI013, ALI013a], however, with a different event selection than those from ALICE and CMS hence these results are not directly comparable to the ones obtained by ALICE and CMS [HFP13]. These measurements therefore provide important inputs to tuning of such theoretical models.

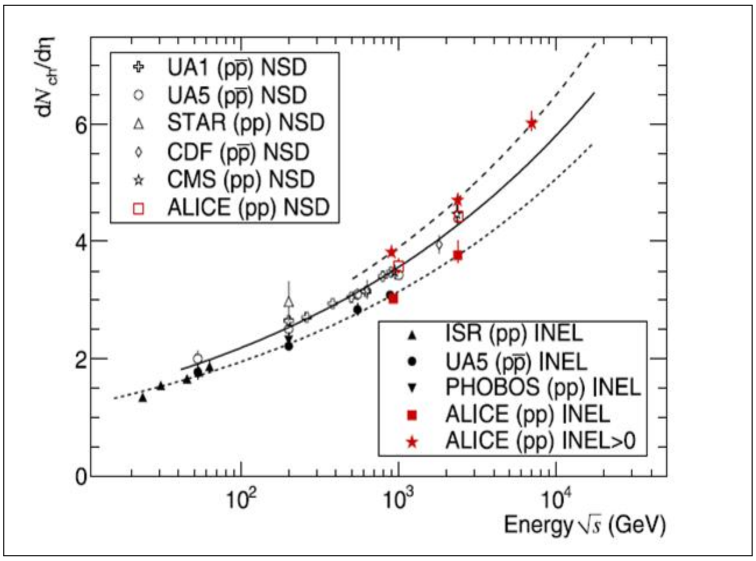

Figure 1.2: Pseudorapidity density of charged particles measured at LHC by different experiments at different collision energies [RIG13].

On the other hand, the results obtained in pp collisions at various LHC energies [HFP02], showed that the charged-particle average transverse momentum ($<p_{\mathrm{T}}>$) spectrum studied as a function of the charged-particle multiplicity ($\mathrm{N_{ch}}$) carries important information about the underlying particle production process. This has been studied by many experiments in hadron colliders in pp and proton-antiproton (p$\bar{p}$) collisions at centre-of-mass energies from 31 GeV up to 7 TeV [A+03]. An increasing $<\mathrm{p_T}>$ with $\mathrm{N_{ch}}$ was observed at central rapidity. This result was well reproduced by PYTHIA 6.4 [SW07] event generator. Although PYTHIA 6.4 gives a good description of the data in this regard, however, a full consistency of models with data is still necessary. The results obtained by the ALICE collaboration for the measurement of $<p_{\mathrm{T}}>$ as a function of the charged-particle multiplicity for pp collisions is shown in Figure 1.3. The average transverse momentum increases linearly with the charged-particle multiplicity. The data at LHC energies provides a broad momentum range starting at low $\mathrm{p_T}$, therefore provides an additional input to the models. In Monte Carlo event generators, high multiplicity events are a result of MPIs [HFP02] therefore the observed strong correlation between the <p_T> and the N_{ch} is attributed to MPIs.

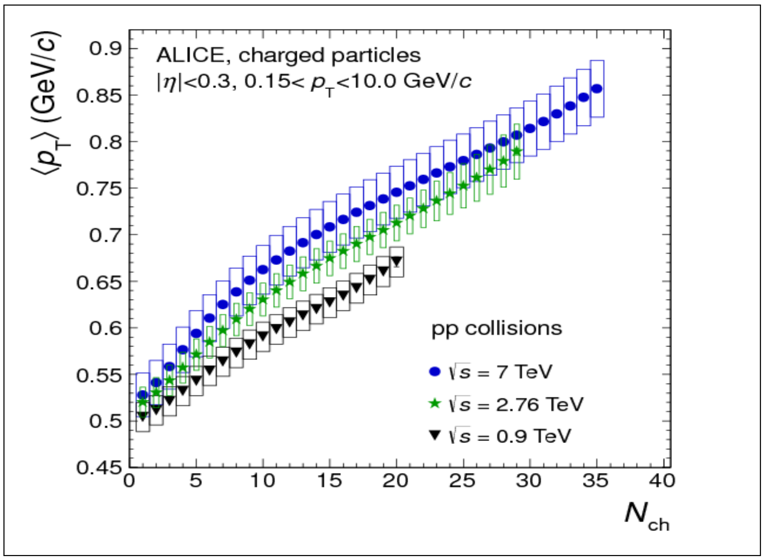

Figure 1.3: Average transverse momentum <p_T> in the range $0.15 < p_T < 10$ GeV/c as a function of charged-particle multiplicity N_{ch} in pp collisions [A+05]

Thus, it is imperative to consider that in high energy pp collisions MPIs can induce a dependence of the particle production on the charged-particle multiplicity of the event. The multiplicity of charged particles becomes a direct measurement of the number of partonic interactions in pp events. However, MPIs are a low momentum transfer process which, according to PYTHIA 6.4, is expected to affect the production of light quarks (e.g. up (u) and down (d) quarks) and gluons. This means that the production of heavy quarks, i.e. both quarkonia (e.g J/Ψ) and heavy flavour (e.g. c and b hadrons) should not be influenced by MPIs and their production rates should then be independent of the charged-particle multiplicity of the event.

1.2 Heavy quark production

Heavy quarks also known as heavy flavours, which consist of open charm (c) and beauty (b) hadrons and their bound or quarkonia states of $c\bar{c}$ (e.g. J/Ψ) and $b\bar{b}$ (e.g. Upsilon) are formed in the initial stages of the collision through gluon fusion, a dominant process at LHC energies [HFP01]. The study of heavy quark production in pp collisions at LHC energies provides an important test of pQCD calculations [NAS03, CGN98] in a new energy domain, where unprecedented small momentum fraction values, so called Bjorken-x, are probed. Furthermore, the investigation of heavy flavour production in pp collisions constitutes an essential baseline for the corresponding measurements in heavy-ion collisions because the production of heavy flavour in heavy-ion collisions, e.g. PbPb collisions, provides a unique tool for studies of the properties of the QGP at the LHC energies [HFP02]. As shown in Figure 1.4, copious amounts of heavy quarks are produced at the LHC [HFP02, HFP14]. With regards to heavy quark production, ALICE has published a few papers on the production of heavy quarks, [HFP03, HFP04, HFP05, HFP06, HFP07, HFP09]. These measurements include heavy-flavour differential cross sections both at mid rapidity and forward rapidity in pp collisions and are well reproduced by pQCD theoretical calculations based on Fixed Order Next to Leading Log (FONLL) [A+04, CNV05] within uncertainties.

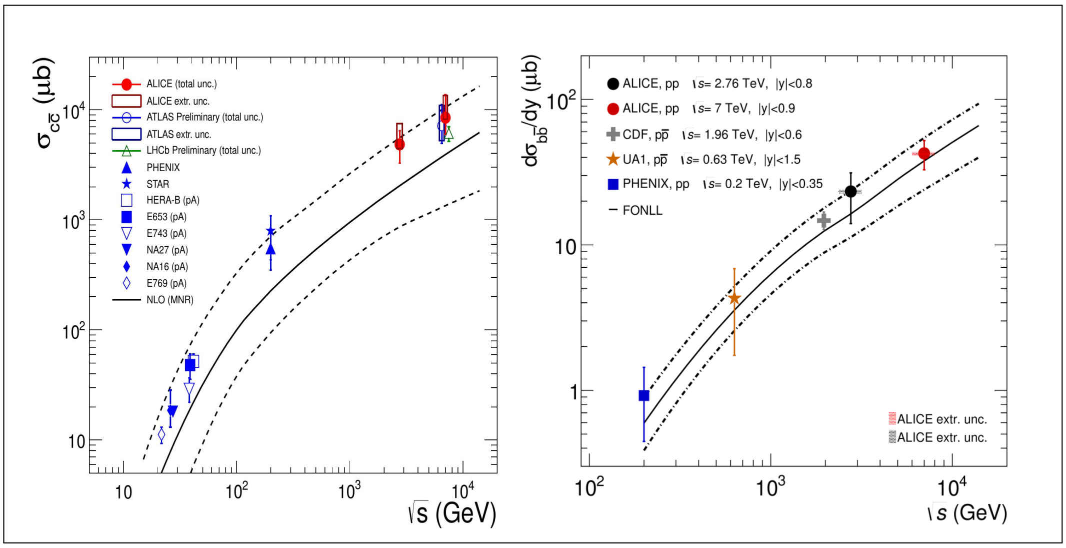

Figure 1.4: Energy dependence of the total nucleon-nucleon charm and beauty production cross section [HFP02, HFP14]

At the high center-of-mass energies reached at the LHC, there might be a substantial contribution of MPIs on the production rates of the heavy quarks in pp collisions. This means that there may be a correlation between the yield of heavy quarks and the total charged-particle multiplicity at LHC energies.

One other interesting study pertains to the results obtained by the ALICE collaboration in the measurement of the relative yield of J/Ψ, at both mid and forward rapidity as a function of the relative charged-particle multiplicity in pp collisions at 7 TeV [COL06]. The result, shown in Figure 1.5, shows that the relative yield of the J/Ψ increases almost linearly with the relative charged-particle multiplicity. This result might be interpreted as either indicating that J/Ψ production in pp collisions is always connected with a strong hadronic activity, or that MPIs could also affect the high momentum scales relevant for J/Ψ and heavy quark production. In the paper, it was concluded that further studies of charged-particle multiplicity dependence of heavy quark production, also as a function of p_T, are therefore necessary to shed more light on the nature of the observed effect. Other studies pertain to the measurement of charm and beauty production multiplicity dependence in the central rapidity of ALICE in pp collisions at 7 TeV via the semi-leptonic channel [SCH09]

1.3 Motivation

Similarly, in this thesis the production of heavy flavours is studied via their muonic decay channel in pp collisions at 8 TeV at forward rapidity, $-4 < \eta < -2.5$, of ALICE, as a function of the charged-particle multiplicity. We are motivated by [COL06, CMS02]

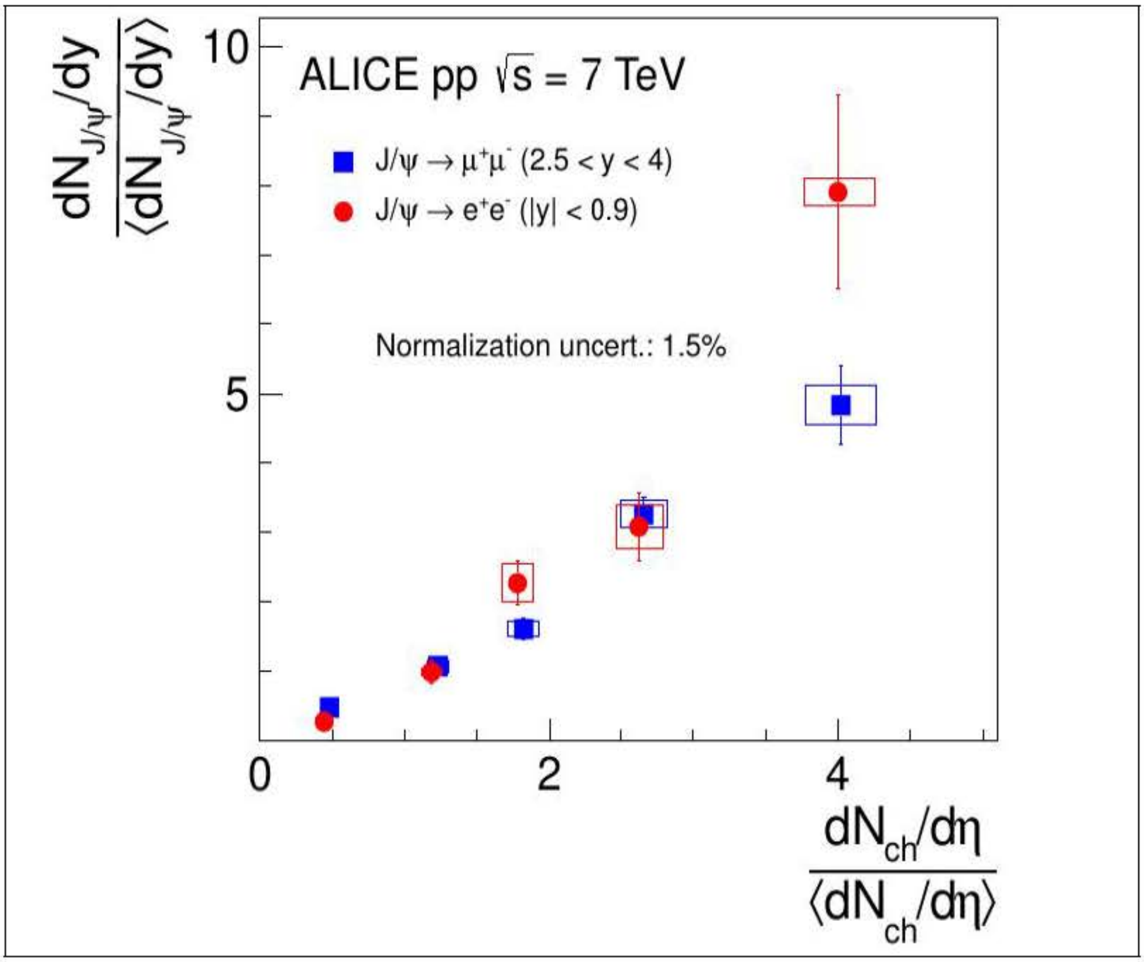

Figure 1.5: The result from [COL06]

to study the correlation of the yield of heavy flavour muons with the charged-particle multiplcity. As discussed above, at LHC energies pp collisions are expected to be dominated by MPI, which involves only light quarks and gluons, (soft processes). Contrary, heavy flavours are produced at the early stages of the interaction, thus it is expected that the production of heavy flavours will not be affected by the MPI, therefore will be independent of the charged-particle multiplicity of the event. This study, very much like the others already is on a quest to provide more insight on the interplay between soft and hard mechanisms in heavy flavour and heavy quark production at LHC energies in pp collisions.

1.4 Objectives and thesis outline

As already discussed above, the objective of the this thesis is to study the correlation between the charged-particle multiplicitity and heavy flavour production in pp collisions with an aim to see if MPIs have an influence on heavy flavour production, i.e. if a linear dependence seen in [COL06] is also seen in the production yields of heavy flavour. Therefore we will analyse data collected by the ALICE experiment in 2012 during pp collisions at the LHC. The charged-particle multiplicity will be measured in the central barrel of ALICE, mainly using the Silicon Pixel Detector at $|\eta| < 1.0$

while the yield of single muons from the decay of charm and beauty hadrons will be measured in the forward rapidity, $-4 < \eta < -2.5$, using the Muon Spectrometer.

The thesis is organised as follows:
Chapter 2 consists of a theoretical discussion relevant for the study.

Chapter 3 gives an outline of the ALICE experiment, with an emphasis on the Muon Spectrometer. Also, a detail of data taking conditions and the ALICE offline framework.

Chapter 4 is dedicated to the charged-particle multiplicity measurement and the extraction of the inclusive muon p_{T} differential yields and Monte Carlo simulation done to correct for detector efficiency.

Chapter 5 consists of the final result of single muon yields as a function of multiplicity a discussion of the result.

Chapter 6 consists of the summary and conclusions.

Chapter 2

Theoretical considerations

This chapter is dedicated to the discussion of the theoretical aspects relevant to this thesis. In particular, we give a brief overview of the Standard Model of particles, provide a basic introduction to Quantum Chromodynamics (QCD) as prelude to the discussion on high energy pp physics as well as heavy flavour production.

2.1 The Standard Model of particles and QCD

Quarks and leptons are the fundamental constituents of matter. In the standard model there are six quark flavours arranged in three families. Quarks and leptons are fermions[1] and are organised into three generations. The six quarks, also called flavours, are: up (u), down (d), strange (s), charm (c), top (t) and bottom (b) and there are six leptons: electron (e), electron neutrino (υ_{e}), muon (μ), muon neutrino (υ_{μ}), tau (τ) and tau neutrino (υ_{τ}). Quarks have fractional charges (-1/3 or +2/3) and have an additional intrinsic property called colour charge. Quarks and leptons are held together by fundamental forces which are represented by the exchange of particles known as gauge bosons and these are photons (γ), gluons (g), W^{+}, W^{-} and Z bosons. Bosons have an integer intrinsic spin. The photon and the Z boson are neutral. The gluon is electrically neutral but like quarks it carries colour charge. The standard model also includes the Higgs boson. which was recently discovered and confirmed by experiments at the LHC [HIG01,HIG02]. The Higgs boson is a spin-0, neutral particle which gives account of the masses of particles. Figure 2.1 shows the standard model particles and their masses.

Gluons are carriers of the strong force,which holds quarks (q) and antiquark ($\overline{q}$) into hadrons[2]. The strong force is governed by the theory of Quantum Chromo Dynamics (QCD), which postulates the existence of the strong colour charge that is associated with quarks and gluons and is responsible for the strong interaction. The force between quarks grows rapidly for large seperations ($>$ 1 femtometre (fm)), confining quarks and gluons to hadrons. To account for all known hadrons, QCD introduces a quantum property called color charge. Each quark (anti-quark) is assigned a color of red, green or blue (anti-red, anti-blue, anti-green). Only colour neutral objects are allowed, e.g. mesons which consist of two quaks, i.e. quark-antiquark pair, and baryons which consist of three quarks eg. qqq or $\overline{qqq}$ etc.

---

[1] Half integer spin particles.

[2] Hadrons are particles made up of quarks/antiquarks and gluons, e.g. a proton.

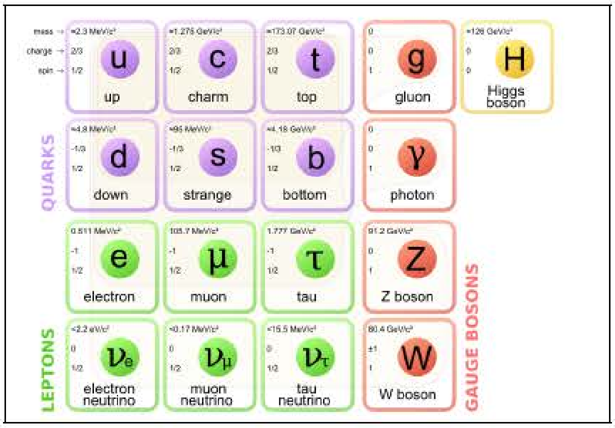

Figure 2.1: The Standard Model Particles [SMO]

Gluons carry one colour charge and one anti-color charge, hence they couple not only to quarks but also to each other. In the framework of the pertubation theory [PNP01], gluons are constantly exchanged between quarks and through a virtual emission and absorption process. When a gluon is transferred between quarks, a colour change occurs in both; e.g. if a red quark emits a red anti-green gluon, it becomes green and if a green quark absorbs a red anti-green quark it becomes red. Even though the quark's color constantly changes, their strong interaction is preserved [FWD01].

Since gluons carry colour charge, they themselves are able to emit and absorb other gluons. As quarks come closer to each other, the chromodynamic binding between them weakens [FWD02]. Conversely, as the distance between quarks increases, the binding force strengthens. The colour field becomes stressed and more gluons of the appropriate colour are spontenously created to strengthen the field. Above a certain threshold, pairs of quarks and anti-quarks are created. These pairs bind the quarks being seperated, causing new hadrons to form. As a consequence, quarks never appear in isolation [FWD03, FWD04]. This process is known as hadronization and occurs before quarks formed in a high energy collision are able to interact in any other way. As the strong interaction does not discriminate between different flavours of the quark. QCD has approximate flavour symmetry (i.e. two or more quarks flavours may be interchanged without affecting the physics in an interaction), which is broken by differing masses of the quarks. There are additional global symmetries whose definitions require the chirality - discrimination between left and right-handed particles. If the spin of a particle has a positive projection on its direction of motion it is called left-handed; otherwise, it is right-handed. Chirality and handedness are not the same but approximately equal at high energies. Chiral symmetries, involve independent transformations of these two types of particles. Chiral symmetry is spontenously broken by the QCD vacuum. Two different types of symmetry exist: one that acts on different colours of quarks (gauge symmetry mediated by gluons) and flavour symmetry which rotates different flavours of quarks to each other, flavour SU(3), which is an approximation of the vacuum of QCD and is not a fundamental symmetry but is an accidental consequence of small mass of the three lightest quarks (u, d and s). The QCD vaccum is characterized by infinitely many non-vanishing condensates such as the gluon or quark condensates that, in turn, characterize the normal phase or confined phase of quark matter. QCD vacuum differs from the Quantum Electrodynamic[3] (QED) one because it concerns the screening of $q\overline{q}$ pairs and anti-screening of gluon pairs, which are coloured charged particles, whereas the photon is neutral. As a result, the intensity of the strong interaction diminishes at short distances (high energies) as shown in Figure 2.2.

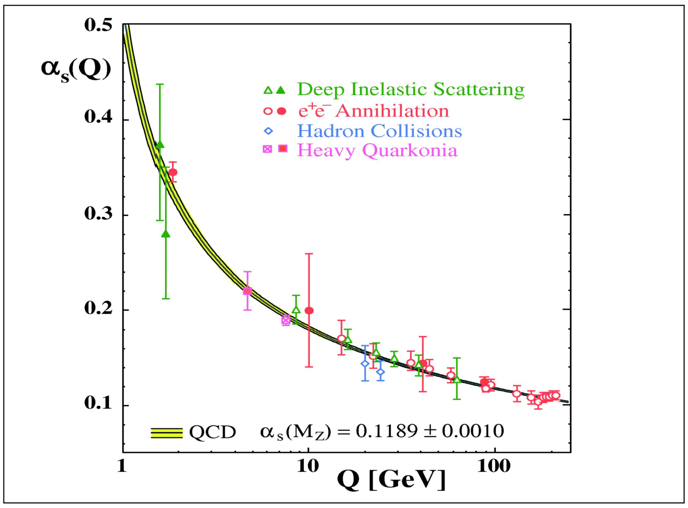

Figure 2.2: The QCD coupling constant α_{QCD} [BET13]

$$\alpha_{QCD}\left(Q^2\right) = \alpha_s = \frac{4\pi}{(11-23n_f)ln(\frac{Q^2}{\Lambda^2_{QCD}})} \tag{2.1}$$

where, Q^2 gives the scale of the interaction, $\alpha_{\mathrm{QCD}}(\mathrm{Q}^2)$ and α_{s} is the QCD coupling constant, $\mathrm{n_f}$ is the number of flavours (e.g. if considering u and d quarks $\mathrm{n_f} = 2$) and Λ_{QCD} is the QCD parameter determined by experiments.

Thus, for small values of Q^2 (small energies), the strong coupling constant has large values $(\alpha_{\mathrm{s}}) \gg 1$. This explains the magnitude of the strong force and the fact that quarks are confined in neutral colour states: the baryons and the mesons. This is known as *colour confinement*. This aspect of QCD is verified with Lattice QCD (lQCD) computations but is not mathematically proven while the other aspect of non-pertubative QCD [PNP01] are the exploration of the phase of quark matter shown in Figure 2.3.

On the contrary, for high energies the momentum transferred is large and α_{s} becomes small; the quarks and gluons interact very weakly. This is known as *asymptotic freedom* [GW73, POL73]. The bag model describes both confinement and asymptotic freedom by modelling hadrons as spherical bags of radius R within which partons (quarks and gluons) can move freely but are prevented to escape outside R by an inward pressure due to colour confinement [SQU79].

Pertubative QCD (pQCD)

Perturbative QCD (pQCD) is the subfield of physics in which QCD is studied by using the fact that the strong coupling constant α_{s} is small at high energy or short-distance interactions, thus allowing perturbation theory [PNP01] techniques to be ap-

---

[3] The quantum field theory of the electromagnetic force.

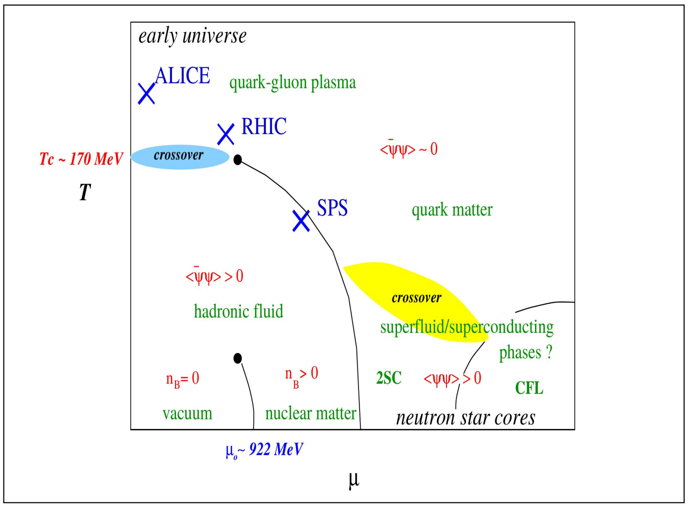

Figure 2.3: The phase diagram of QCD [KAR07]

plied. However, most of the processes cannot be calculated directly with pQCD, since quarks and gluons cannot be observed in isolation due to colour confinement. Hence the hadron structure has a non-perturbative nature. As a general cross section is a combination of short and long distance behaviour, therefore it is not computable directly in pQCD. As a result, physicists developed the QCD factorization theorem [CSS89] which addressed how to calculate high energy cross sections. Factorisation theorems allow physicist to derive predictions for high energy (large momentum transfer) cross sections, by seperating (factorizing) long distance from short distance behaviour in a systematic fashion. Consequently, almost all applications of pQCD use certain factorization properties. They seperate the cross section in two parts;

- the process dependent pQCD calculable short-distance parton cross section,
- the universal long-distance functions, which can be measured with global fits to experiments in order to obtain a partly calculable prediction to particle reaction processes.

Long-distance functions include parton distribution functions (PDFs), fragmentation functions, multi-parton correlations functions, etc. Several good experimental quantitative tests of pQCD at collider facilities include, amongst others, the production of vector bosons, measurement of jet cross section, heavy quark production and so on.

2.2 High energy pp collisions

QCD is the underlying theory for soft and hard processes in high energy proton-proton collisions. For hard processes, e.g. heavy quark production, the rates and event properties can be predicted with good precision using the perturbative theory. For soft processes, e.g. the total cross section, underlying event etc., the rates and properties of the process are dominated by non-perturbative QCD effects[4], which are still not yet well understood. It is important to note that in hard processes, soft interactions occur along with the hard interactions. Therefore, the effects of the soft interactions

---

[4] Effects of QCD at long distance interactions.

must be well understood to allow comparisons with the perturbative predictions. Soft interactions are important for understanding both the signal and backgrounds for the hard process. In a high energy pp collisions, Figure 2.4, the two partons of the incoming protons undergo a hard scattering process, characterized by the cross section, $\hat{\sigma}$.

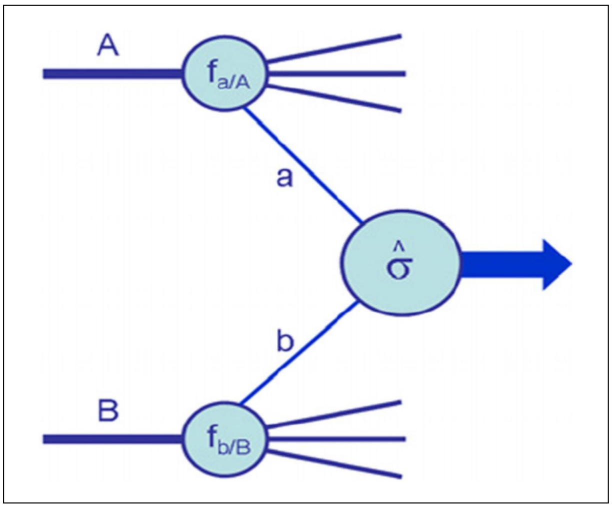

Figure 2.4: Structure of hard process in a pp collision [CHS07a]

The structure of the incoming protons (A and B) is described by their parton distribution functions, (PDFs) $f_{\frac{a}{A}}(x_a,{\mu_F}^2)$ and $f_{\frac{b}{B}}(x_b,{\mu_F}^2)$, respectively. The PDFs give the probability to find a parton a in proton A with a momentum fraction x_a at the energy scale ${\mu_F}^2$. The cross section of this process is determined by obtaining a summation over all possible parton-parton scattering processes and integrating over the momentum fractions as shown in equation 2.2.

$$\sigma_{AB} = \sum_{a,b} \int dx_a dx_b f_{\frac{a}{A}}(x_a, \mu_F^2) f_{\frac{b}{B}}(x_b, \mu_F^2) \hat{\sigma}(x_a, x_b, \alpha_s(\mu_R^2)) \tag{2.2}$$

The calculations of the hard-scattering process cross sections are performed in pQCD and the results depend on the strong coupling constant, α_s, and its renormalization scale ${\mu_F}^2$, which is also the scale that separates long and short distance physics [CHS07b]. Equation 2.2 can only be used to describe hard scattering events where the effective centre-of-mass energy of the interaction is far less than the centre-of-mass energy of the collider. Each interacting parton carries a certain fraction of the proton momentum which depends on its mass and rapidity[5] (y). An example of the parton momentum distributions in a proton is shown in Figure 2.5. As Up (u) and down (d) quarks contribute to the quantum numbers of the protons, they form the *valence quarks*. Therefore, they carry a large fraction of the proton momentum. As can be seen in Figure 2.5 a proton contains also gluons and other quarks that give rise to the so-called "sea" and they carry much smaller momenta. Parton momentum distributions depend on the momentum transfer in the interaction, Q^2. At large Q^2 the interacting particles see the short-distance structure of the proton and hence have access to the "sea" of quarks and gluons inside the proton, in addition to the valence quarks. Consequently, the PDFs are shifted towards small x values, where x is the fraction of the proton momentum carried by the interacting partons, also known as

---

[5] Rapidity is the representation of the speed of motion of the parton.

the Bjorken-x [IAN11]. For small Q^2, only the valence quarks are visible and the PDFs peak at large x values.

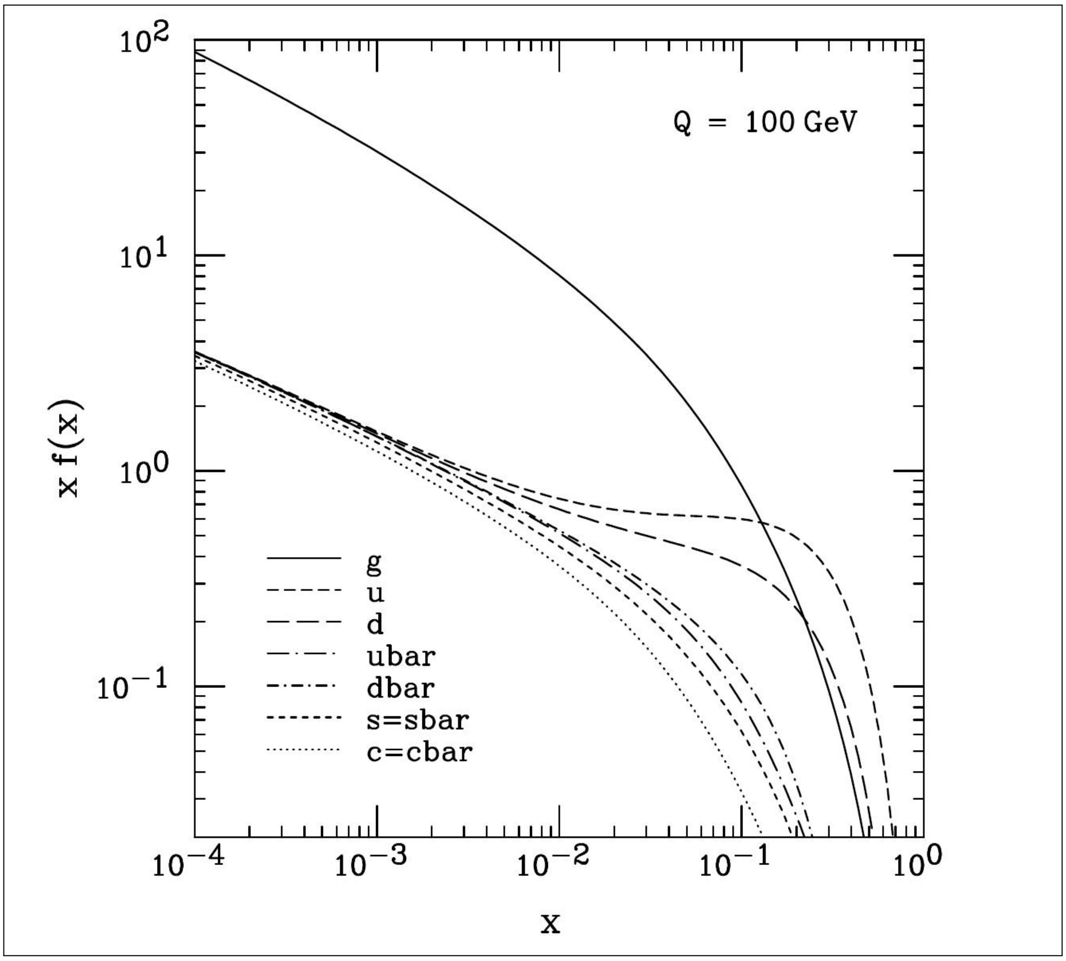

Figure 2.5: Parton Distribution Functions of a proton as a function of Bjorken-x [PSH+02]

At LHC energies where the Q^2 is very large, there is access to more particles in a single pp collision, mostly gluons as they dominate the small x region. Due to the high gluon density in each colliding proton, the short-distance hard scattering process occurs concurrently with multiple parton interactions (MPIs) [B+11] where two or more parton interactions occur simultaneously in a single collision.

2.3 Multi-parton interactions

As discussed above, MPIs, (see schematic depiction in Figure 2.6), describe the phenomenon when a hard primary interaction is accompanied by a second scattering process. MPIs are often split into two groups, soft and hard MPIs i.e. if the resulting particles have a rather high transverse momentum it is called hard MPI, otherwise it is called soft MPI. While hard MPIs occur rather rarely, soft MPIs are a very frequent process. There can be even higher numbers of additional subprocesses which would lead to triple or even higher parton interactions.

As mentioned above, due to the gluon dominated PDFs, pp collisions at the LHC are dominated by MPIs. Most events are due to large distance collisions between the two incoming protons, a non-pertubative process. In this case the momentum transfer of the interaction is small (soft collisions) and therefore particle scattering at large angles is suppressed. The particles produced in the final state of such interactions have large longitudinal momentum, but small transverse momentum (p_T) relative to the beam line. Due to several interactions occuring at parton level in the collision, particle production becomes dependent on the total charged-particle multiplicity. Head-on collisions may occur occasionally between two partons of the incoming protons. These are interactions at small distances, and are characterised by large momentum transfers (hard MPI). In this case, particles in the final state can be produced at large angles with respect to the beam line (high p_T) and massive particles can be created.

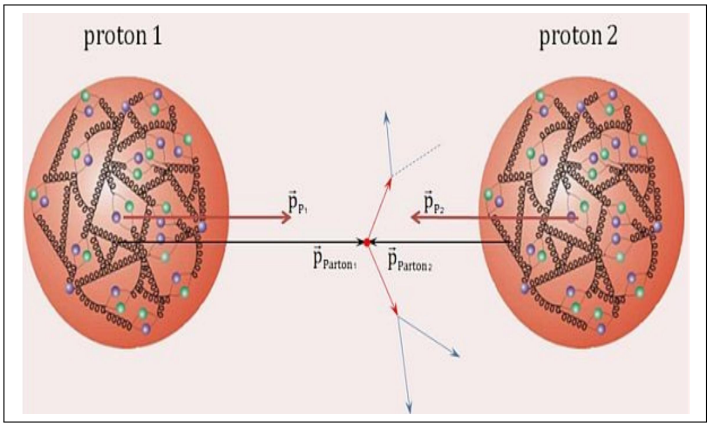

Figure 2.6: A schematic view of multi-parton interactions [ETS]

2.4 Heavy flavour production in high energy pp collisions

Heavy flavours, charm (c) and bottom (b) hadrons, are produced early in the collisions. The production of heavy flavours can be predicted using perturbative QCD, since their masses are large enough ($m_{c,b} \gg \Lambda_{QCD}$[6]) to assure the reliability of the calculations. The measurement of heavy flavour production in pp collisions provides valuable information about the mechanisms involved in the parton interaction. Current theoretical models do not give a complete and accurate description of such mechanisms as non-perturbative phenomena, which have important contribution to heavy flavour production. The available calculations are performed by matching the resummation of logarithms of the transverse momentum over the mass of the quark at first-order-next-to-leading-logarithm (FONLL). The results plus next-to-leading-logarithm (NLO), next-to-next-to-leading-logarithm (NNLO) and FONLL corrections

---

[6] Λ_{QCD} represents the characteristic scale of confinement where the pertubative approach is not valid due to a large α_s.

are currently the basis of the heavy flavour calculations.

The leading order process (LO) in hadronic collisions is flavour creation: quark-antiquark annihilation and gluon-gluon fusion;

$$q\overline{q} \rightarrow Q\overline{Q} \tag{2.3}$$

and

$$gg \rightarrow Q\overline{Q} \tag{2.4}$$

For high partonic energy systems, the cross section of gluon-gluon fusion process is much higher than quark-antiquark annihilation process. So at LHC energies, heavy quark production is dominated by gluon-gluon fusion process. Heavy quarks produced via gluon fusion are back-to-back, i.e. they move in opposite directions with almost similar $\mathrm{p_T}$.

In the LO approximation, three important Feynman diagrams for the gluon-gluon fusion are shown in Figure 2.7.

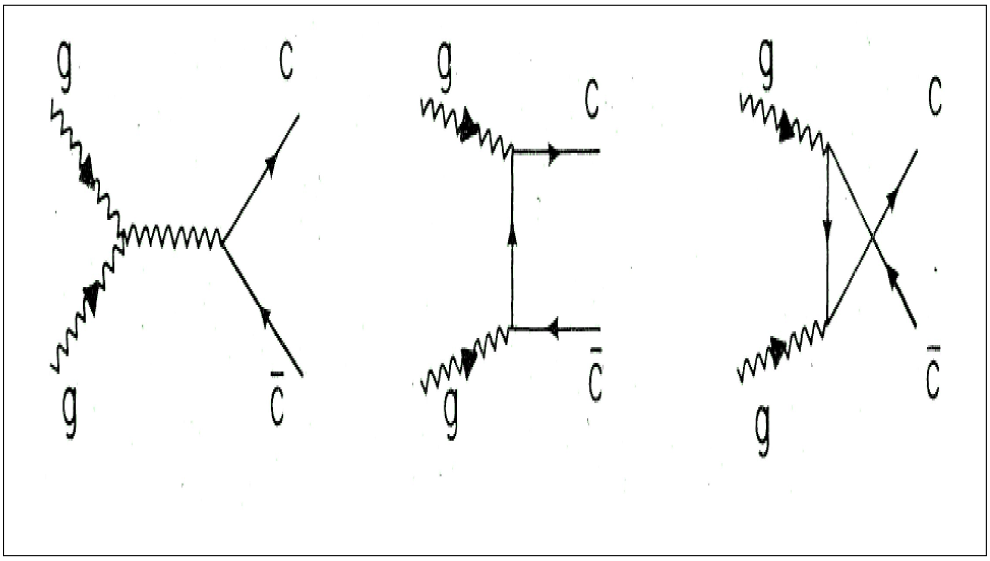

Figure 2.7: Feynman Diagrams of Heavy flavour production via gg fusion

Heavy quarks can be produced via flavour excitation, shown in Figure 2.8. In the flavour excitation process, the heavy quark is considered to be already present in the incoming hadron. It is excited by the exchange of a gluon with the other hadron and appears on mass-shell[7] in the final state. Since the heavy quark is not a valence quark, it must be produced from the exchange of a gluon with the other hadron. The hard scattering in flavour excitation pair-production process, g → $\mathrm{Q}\overline{Q}$, must have a partonic energy virtually above $\mathrm{m_Q}^2$, for the heavy quark to be present in the initial state. The heavy quark final states do not need to be back-to-back as the third parton can carry away some transverse momentum.

In experiments, the presence of hadrons containing heavy quarks is deduced by their decay products. They can decay to other lighter hadrons, (e.g. pions, Kaons etc.) or to leptons (e.g. electrons, muons). In a first approximation of heavy-flavoured

---

[7] The relation between the momentum and energy for a particle of a given mass.

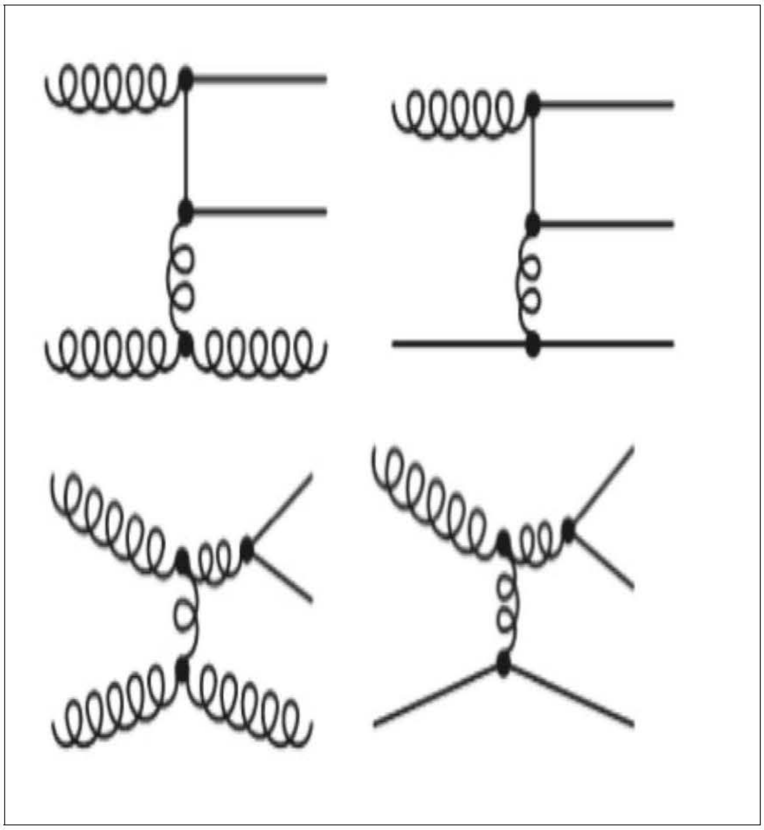

Figure 2.8: Feynman Diagram of Heavy flavour production via flavour excitation

hadron decays, only heavy quark participates in the transition while the other quarks in the hadrons act as spectators. The heavy quarks decay via weak interaction i.e. a b-quark may decay into a c or u-quark, while a c-quark may decay into an s or d-quark. Semi-leptonic decay of heavy flavours into muons are thoroughly studied in this analysis because the muon provides a clean signature which is relatively easy to detect experimentally.

In the following chapter we discuss the details of the experiment.

Chapter 3

Experimental setup

3.1 The Large Hadron Collider (LHC)

The Large Hadron Collider [LHC01] is presently the largest particle accelerator in the world. It is situated in a 27-kilometer circumference tunnel and about 100 meters underground between Switzerland and France. The LHC is designed to accelerate proton and lead bunches[1] up to a nominal centre-of-mass energy of 14 TeV and 5.5 TeV per nucleon pair, respectively.

The LHC, shown in Figure 3.1, is the last stage of the acceleration procedure involving many other machines. The particles to be accelerated are extracted from a source, i.e. hydrogen, for proton-proton (pp) collisions and ionised isotopically-enriched lead for lead-lead (PbPb) collisions. Protons are injected into LINAC2 where they are accelerated to 50 MeV and then passed to the Proton Synchrotron Booster (PSB), the Proton Synchrotron (PS), the Super Proton Synchrotron (SPS) and finally to the LHC, acquiring more energy at each step. When the protons are extracted from the SPS to be injected into the LHC ring they have an energy of 450 GeV. For example, for pp collisions in 2010 and 2011 the LHC accelerated each proton beam to the final energy of 3.5 TeV. Figure 3.1 shows the LHC and each acceleration stage.

The LHC ring hosts four experiments, shown in Figure 3.2. (ATLAS [ATL01] and the CMS [CMS01] are two big multi-purpose experiments whose main research goal is the detection of the Higgs boson and the study of Standard Model physics and beyond. LHCb [LHC98] experiment specializes in the investigation the slight differences between matter and antimatter by studying the bottom (b) quark. Lastly, ALICE [ALI01] whose detailed description is given in the following sections.

3.2 The ALICE experiment

ALICE is a heavy ion detector on LHC ring designed to study the properties of the Quark Gluon Plasma (QGP) formed by colliding heavy ions (e.g. Pb ions). Physicists are studying the QGP because they want to understand QCD - the theory of strong interactions as well as deconfinement in the Standard Model.

---

[1] A bunch is a beam of squeezed groups of particles, in this case protons or lead ions.

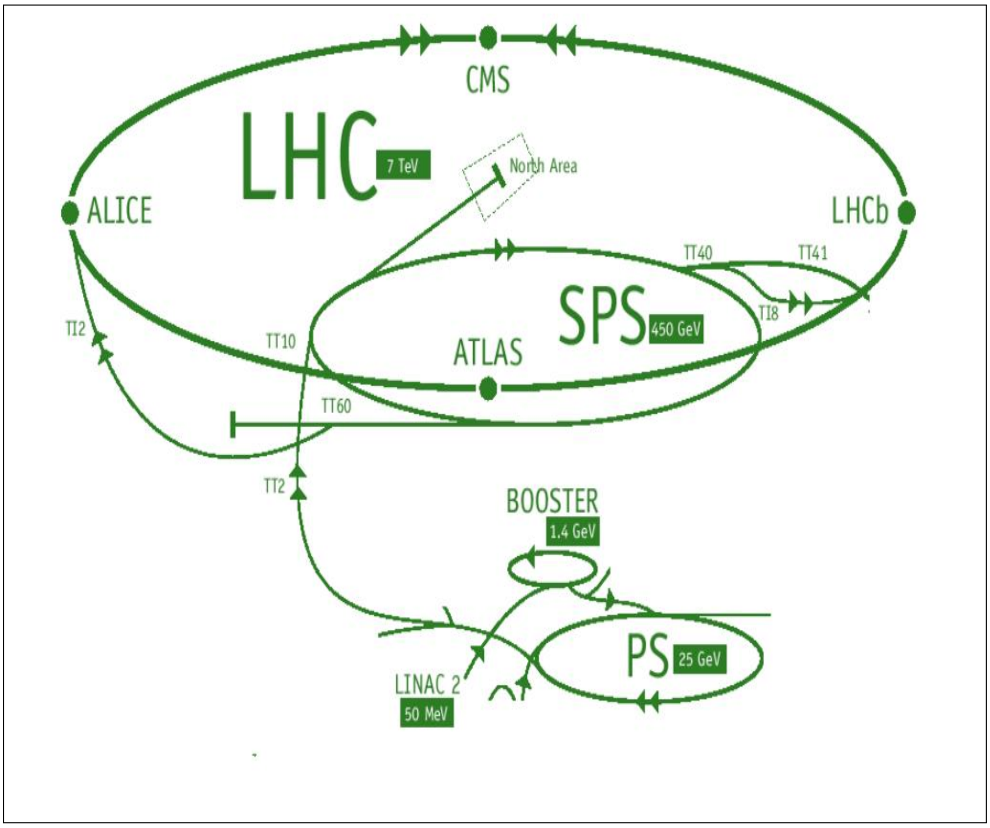

Figure 3.1: The LHC and accelerators at CERN [CER01]

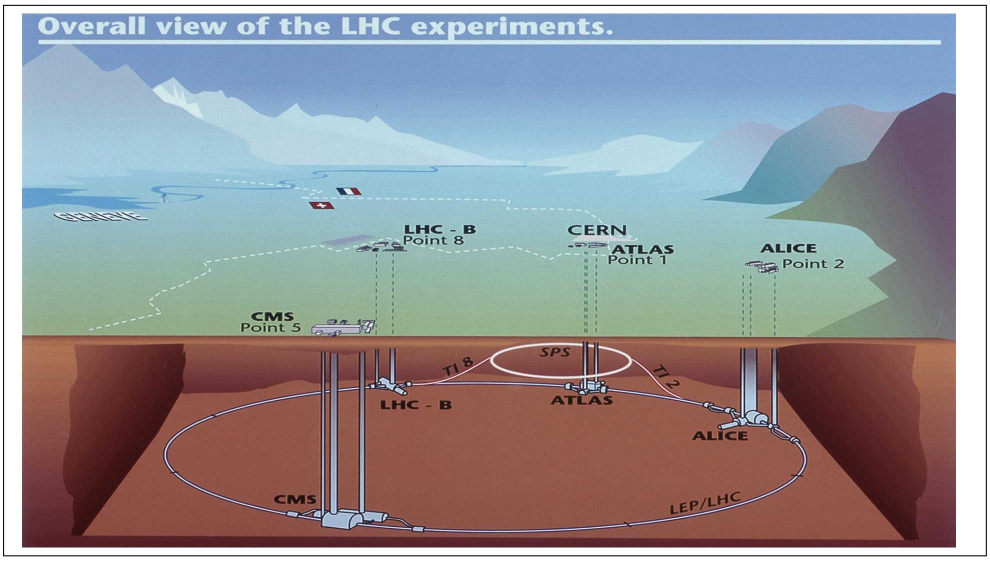

Figure 3.2: The overall view of the 27 km CERN Large Hadron Collider (LHC), showing the location of the four main experiments [CER02]

The layout of the ALICE detector is shown in Figure 3.3. The detector is made up of three components, namely, the central barrel detectors, global detectors and the forward muon spectrometer.

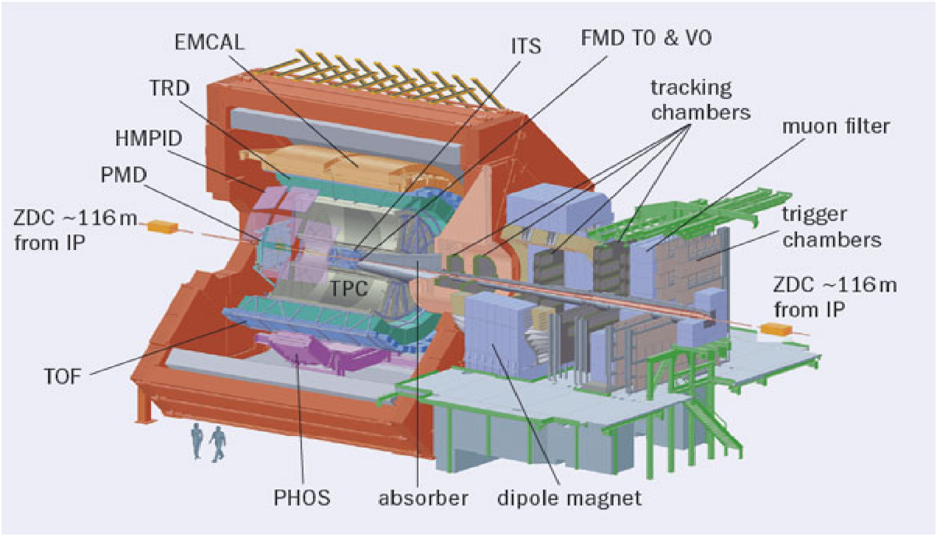

Figure 3.3: The ALICE Detector [COL07]

3.2.1 ALICE cordinate system

In the standard ALICE co-ordinate system, the Interaction Point (IP), where the particles collide is at the origin of the right handed cartesian co-ordinate system [COO]. From the IP the z-axis is along the beam pipe, the x-axis points to the center of the LHC, φ is the angle around the beam axis and θ indicates the angle from the beam axis. The coordinate system is shown in Figure 3.4. On the A and C side are the ATLAS and CMS experiments, respectively.

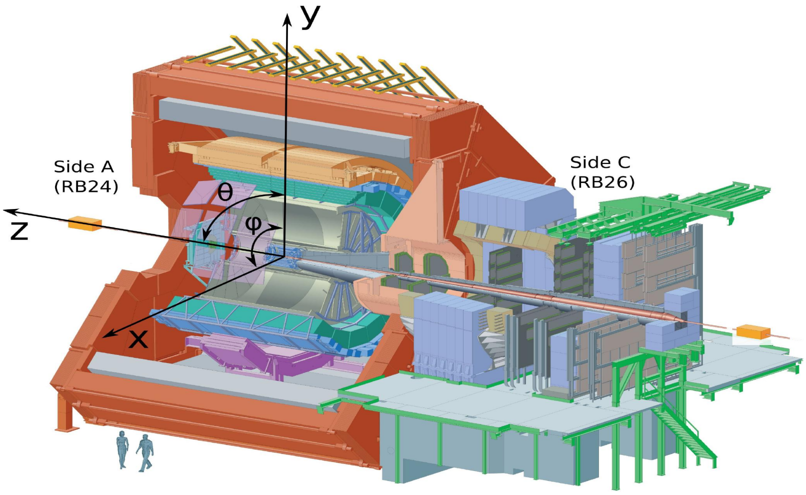

Figure 3.4: The ALICE coordinate system [COO]

Pseudorapidity, η, describes the angle of the particle relative to the beam axis. It is mathematically defined as;

$$\eta = -ln[tan(\theta/2)] \tag{3.1}$$

3.2.2 The central barrel detectors

The L3 magnet houses the central barrel detectors that cover the pseudorapidity range $-0.9 < \eta < 0.9$, a polar angle $45^o < \theta < 135^o$. From the inside out, the central barrel consists of the Inner Tracking System (ITS), made up of six planes of high resolution Silicon Pixel Detectors(SPD), Silicon Drift Detectors (SDD) and Silicon Strip Detectors (SSD), a cylindrical Time Projection Chamber, (TPC), a Transition Radiation Detector, (TRD), the Time of Flight Detector, (TOF), the High Momentum Particle Identification Detector, (HMPID) and two ElectroMagnetic Calorimeters (EMCal) and the Photon Spectrometer (PHOS). These detectors allow for primary vertex reconstruction, charged-particle tracking over a momentum range of 10 MeV to 100 GeV and particle identification for charged hadrons, electrons and photons.

3.2.2.1 The Inner Tracking System (ITS)

The ITS, shown in Figure 3.5, consists of 6 semiconductor-based detectors at the centre of the Central Barrel [ALI09]. From the beam pipe going radially outwards, there are two layers of SPD, two SDD and finally two SSD. The ITS provides primary and secondary vertex information as well as tranverse momentum (p_T) spectrum for particles with low p_T.

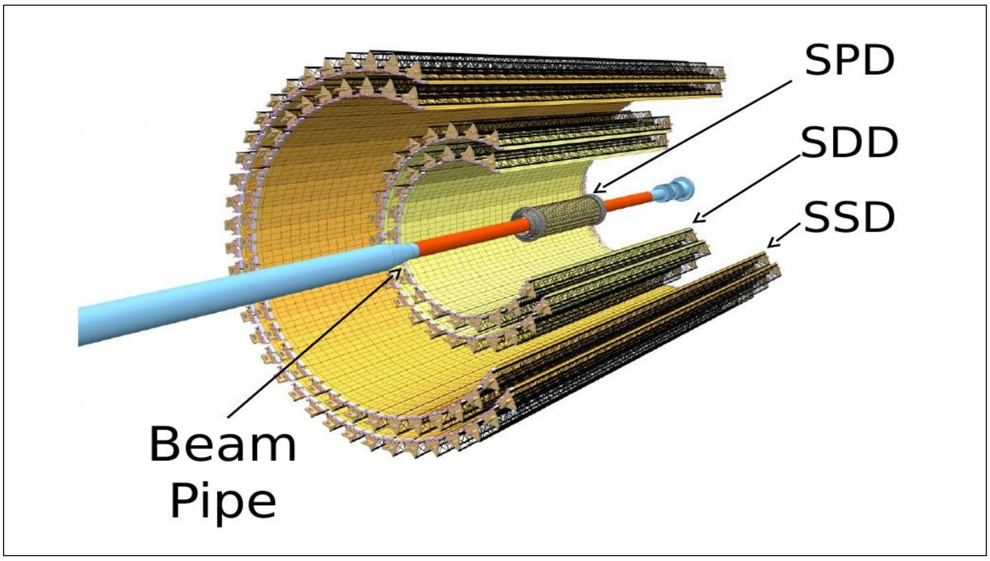

Figure 3.5: The Inner Tracking System [A+02]

3.2.2.2 Silicon Pixel Detectors (SPD)

The SPD covers the pseudorapidity of $\eta < 1.95$ and $\eta < 1.4$ for the inner and outer layers, respectively. This is so that in combination with the Foward Multiplicity Detector (FMD), charged-particle multiplicity can be provided over a full rapidity range. The inner most detector plays an important role of determining the primary and secondary vertices in order to reconstruct the decay of baryons which contain either charm or strange quarks. The SPD is very thin (750 μm), allowing minimum energy to be deposited onto it and is designed to withstand high radiation doses since it is near the IP.

3.2.2.3 Silicon Drift Detectors (SDD)

The SDD covers the pseudorapidity of $\eta < 0.9$. As a charged particle passes through the silicon, it excites electrons and leaves a trail of them. These electrons are then attracted to the n-type semiconductor. It gives a high precision position information and also provides energy loss ($\frac{dE}{dx}$) information which can be used for particle identification (PID).

3.2.2.4 Silicon Strip Detectors (SSD)

The SSD covers the pseudorapidity of $\eta < 0.97$. It is the outermost layer of the ITS. It has n and p type semiconductors like the SDD, on the top and bottom of the detector. Holes and electrons are released as the particle goes through the detector, which are attracted towards the semiconductor readout. The SDD is used for position information and particle identification.

3.2.2.5 The Time Projection Chamber(TPC)

The TPC is a cylinder shape around the beam axis. The cylinder contains 90 m^3 Ne/CO$_3$N$_2$ gas mixture in it and consists of Multi Wire Proportinal Chambers (MWPC) with a cathode readout mounted on them. It has an inner radius of 85 cm and an outer one of about 250 cm with a total length of about 500 cm [RNWG07]. The TPC is designed to handle high multiplicities produced in heavy ion collisions. It generates most of the tracking information within ALICE and provides large amounts of data. It is used mainly for tracking but also measures $\frac{dE}{dx}$ and momentum information which helps PID. It allows the measurement of charged particles from a p_T of 100 MeV to 100 GeV.

3.2.2.6 The Transition Radiation Detector (TRD)

The TRD consists of 18 sectors of 6 layers with a 5-fold segment along the beam direction for a total of 540 detector modules. Each module consists of a radiator 4.8 cm thickness and MWPC readout with cathode pad readout [PAC14].

When charged particles pass through two media of different dielectric constants radiation is produced. The innermost layer of the TRD is a radiator, the charged particle passes through this and since it is foam the dielectric constant alternates between that of air and the foam material. This will generate a transition radation X-ray. If the momentum of the particle is large enough, these are then absorbed in the beggining of the module's drift chamber. The drift chamber contains a strong electric field and a gas consisting of Xe/CO$_2$ in a 85/15 ratio.

When charged particles enter this region they produce an ionization trail unlike the photons which will all be absorbed near the radiator. The electrons from the ionisation drift towards the outer part of the chamber and are amplified in the amplification region, read out by the pads on the outside of the detector and analysed by the front-end electronics on the top of the chamber. The TRD differentiates between high and low energy pions and electrons - when the electron or pion goes through the drift chamber, the ionisation produced by each of them is different. The TRD also increases the ALICE pion rejection capabilities and allows a mass resolution of 100 MeV at the Upsilon (Υ) region for a magnetic field (B) = 0.4 T.

3.2.2.7 The Time Of Flight (TOF)

The TOF detector has a cylindrical shape, covering polar angles between 45° and 135°. It has a modular structure with 18 sectors. Each of these sectors is divided into 5 modules along the beam direction. The modules contain a total of 1 638 Multi-gap Resistive Plate Chambers (MRPC), covering an area of 160 m^2 with 157 248 readout channels (pads) [COL02]. When particles pass through the detector an avalanche of electrons are created and readout by the pads. It is located at a radius between 370 cm and 399 cm and has a length of 745 m.
MRPCs provide an intrinsic time resolution of better than 40 pico seconds (ps) and an efficiency close to 100%. The TOF allows for particle identification in the intermediate momentum range from 0.2 GeV to 2.5 GeV. The detectors work by measuring the time particles take to go through the detector and hence work out their speed. At this point the momentum of the particle is already known, therefore, the mass of the particle can be determined allowing particle identification of pions, kaons and protons.

3.2.2.8 High Momentum Particle Identification (HMPID)

The HMPID covers the pseudorapidity range $\eta < 0.6$. The detector is based on proximity focusing Ring Imaging Cherenkov counters and consists of 7 modules of about 15 x 15 m^2 for each [COL01]. It uses CsI photocathode to detect ultraviolet Cherenkov photons emitted by C_6F_{14} radiator. The photons go through a quartz window into a MWPC as in the TRD and are detected by a photo-cathode which is sensitive to hadrons traversing it, so it acts as a charged particle veto, removing events in the photocathode caused by hadrons. It was designed to complement particle identification of the TPC, ITS and TOF which operate up to $p_T \sim 1.4$ GeV. The HMPID works in the region 1-5 GeV to identify pions (π), kaons (K) and rho (ρ). Since the yield of the particles with $p_T > 1$ GeV is expected to be low it does not need to cover the whole central barrel region.

3.2.2.9 The Photon Spectrometer (PHOS)

The PHOS is a single arm spectrometer including a highly segmented electromagnetic calorimeter made of Lead-Tungstenate crystals coupled to an Avalanche Photo Diode followed by a low noise pre-amplifier and a charged particle veto detector consisting of a MWPC with cathode pad readout. It covers a pseudorapidity range of $\eta < 0.12$ and is positioned at 460 cm from the IP [ALI08]. It detects photons that enter it and is sensitive to charged and neutral hadrons.

3.2.3 The Electromagnetic Calorimeter (EMCal)

The EMCal covers the pseudorapidity range of $\eta < 0.7$. It is made up of scintillator towers tapped towards the beam pipe and slanted towards the IP. This increases the path length the particle travels inside the calorimeter and so maximises the total energy deposited in it. The energy that is deposited by either hadrons or photons is turned into more photons by the scintillators. The photons are picked up by the optical fibres and read out on the outside of the detetctor by the avalanche photodiode sensor. It is focused on measuring photons from hard jets. It enables triggering on high energy jets, improves jet energy resolution and increases ALICE capabilities to measure high momentum photons and electrons [A+01]. It has a high momentum resolution for charged particles in the range 100 MeV to 100 GeV which is ideally suited for measuring the full range of hard (High p_T) and soft (Low p_T) jets.

3.2.4 The Global Detectors

These are small detectors namely the Zero Degree Calorimeter (ZDC), the Photon Multiplicity Detector (PMD), the Forward Multiplicity Detector (FMD), T0 and V0 detectors, shown in Figure 3.6. They are located at the forward and backward pseudorapidity regions and are used for the global characterization of the collisions, i.e. centrality determination, multiplicity measurements and event plane reconstruction. They are also used for triggering purposes.

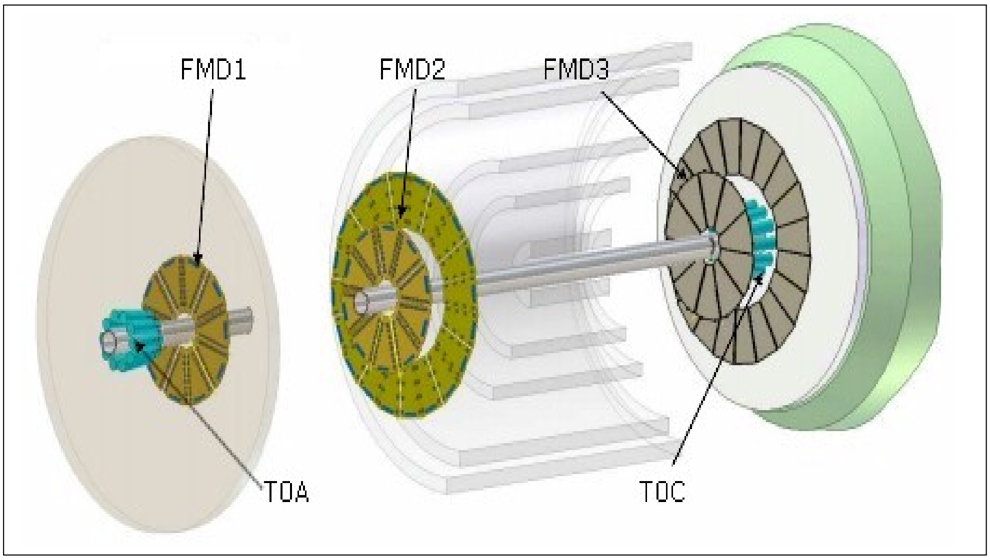

Figure 3.6: The Global Detectors [CAR01]

3.2.4.1 The Photon Multiplicity Detector (PMD)

The PMD covers a pseudorapidity range of $2.3 < \eta < 3.7$. It consists of two identical planes of detectors made of a proportional counter with honeycomb structure and wire readout with a $3X_o{}^2$ thick lead converter inbetween them [ALI07]. The front detector plane is used as charged particle veto to suppress the detection of charged particles hitting the front surface while the detector plane behind the converter is the preshower plane and registers hits from both photons and charged hadrons. It measures the multiplicity and spatial distributions of photons on an event-by-event basis. It also provides approximations for the transverse electromagnetic energy and the reaction plane of the system using the information about anisotropy and radial flow [SRA01].

3.2.4.2 The Forward Multiplicity Detector (FMD)

The FMD covers the pseudorapidity range of $-3.4 < \eta < -1.7$ on the muon spectrometer side and $1.7 < \eta < 5.0$ on the PMD side [ALI07]. FMD 1 consist of a ring of inner-

---

[2] X_o is the radiation length - the distance over which the energy of an electron or photon is reduced by a factor $\frac{1}{e}$ due to radiation only.

type Silicon (Si) sensors while FMD2 and FMD3 each consist of a ring of inner-type Si sensors and a ring of outer-type Si sensor. Each detector ring consists of 10 (for inner rings) or 20 (for outer rings) Si sensors. The full FMD contains 51200 pixel strips to be readout [CBN13]. The overlap of the FMD with the ITS pixel detectors provides redundancy, cross checks of measurements between subdetectors and ensures that continuous coverage for a distribution of vertices along the z-axis. The high radial detector segmentation allows for the study of multiplicity fluctuations on event by event basis and also for the determination of the reaction plane for each of the events as well as the analysis of flow with the FMD's pseudorapidity coverage.

3.2.4.3 TZERO (T0) detector

The T0 detector covers the pseudorapidity range of -3.28 < η < -2.97 and 4.61 < η < 4.92 on the A and C side of ALICE respectively [COL03]. It is made up of two identical detectors on each side of the IP, T0-A on the A side and T0-C on the C side. Each of the two detectors consists of a series of Cherenkov radiators which uses quartz to produce the Cherenkov radiation[3]. The T0 detector provides a trigger on the collision events, calculates an approximation of the vertex position and provides a rough measure of the multiplicity of the events in order to measure centrality. It also provides a T0 signal for the TOF detector to measure the vertex position with a precision of ±1.5 cm.

3.2.4.4 VZERO (V0) detector

The V0 detector covers a pseudorapidity range of -3.7 < η < -1.7 and 2.8 < η < 5.1. It is also split into two, V0-A and V0-C which are two arrays of scintillators located at 90 cm (muon spectrometer side) and 340 cm (PMD side) from the IP [COL03]. Each detector is segmented into 32 elementary counters distributed in 4 rings and 8 sectors. It is a triggering detector, i.e. it triggers after a certain amount of energy has been deposited onto it. This is related the centrality of the collision. It also provides a background rejection capability for the muon spectrometer and rejection of beam-gas events where the energy deposited on each side of the V0 detector is not symmetric.

3.2.4.5 The Zero Degree Calorimeter (ZDC)

There are two ZDC detectors which are placed 116 m on either side of the IP and directly in line with it. The ZDC is a hadron calorimeter made up of a very dense material with quartz fibre going through it. When neutrons pass through the boundary between the metal and the quartz fibre, they produce Cherenkov radiation, - photons are totally internally reflected down the quartz fibre into a photomultiplier tube and they produce an electrical signal that can be analysed by the Front End Electronics [A+01].

The neutrons and protons left in the beam after collisions are measured independently to determine the number of nucleons that were involved in the collision. This is done by splitting the beam into 3 parts, namely, positively charged, negatively charged and neutral. The neutral beam will contain the neutrons and the positive beam will consist

---

[3] Electromagnetic radiation emitted when a charged particle (e.g. electron) passes through a dielectric medium at a speed greater than the phase velocity of light in that medium.

of protons while the negatively charged beam will be used as a reference in order to subtract the background from the other two.

3.2.5 The Forward Muon Spectrometer

The Muon Spectrometer shown in figure 3.7, is designed to detect muons in the forward pseudorapidity region $-4 < \eta < -2.5$. It detects J/ψ, Υ and ϕ and excited states (ψ', Υ', Υ") through their decays into dimuons ($\mu^+\mu^-$) [A+01]. Also, it allows studies of the production of charm and beauty hadrons (heavy flavours) and weak interaction probes (W$^{+/-}$ and Z^0) via their decay into single muons. Furthermore, studies of low mass vector mesons (ρ, ω and ϕ) via dimuon decays are also done. The spectrometer consists of a composite absorber made with layers of both high and low Z-materials, carbon and concrete placed 90 cm from the IP, a large dipole magnet with a 3 Tm field integral placed outside the L3 magnet, 10 planes of thin, high granularity tracking stations followed by a second absorber (iron filter) at the end of the spectrometer and lastly, four more detector planes used for muon identification and triggering. The spectrometer is shielded throughout its length by a dense absorber tube of about 60 cm outer diameter, which surrounds the beam pipe.

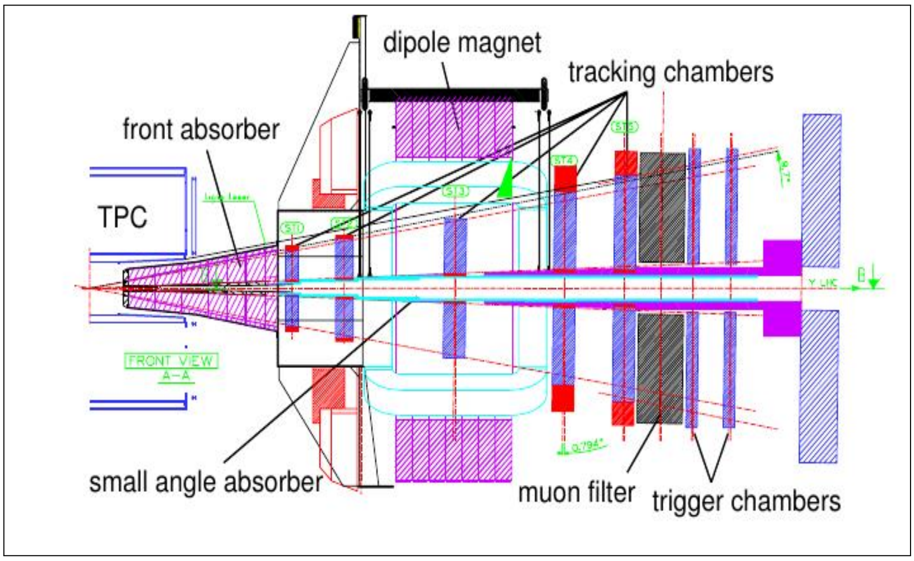

Figure 3.7: The Forward Muon Spectrometer [MUSP]

3.2.5.1 The absorbers

The muon spectrometer contains three absorber sections : the front absober in the pseudorapidity range $-4 < \eta < -2.5$, the beam shield which surrounds the beam pipe and the muon filter between the tracking and the trigger chambers.

3.2.5.2 The front absorber

The front absorber, shown in Figure 3.8, is situated at a distance of z = 90 cm from the IP, in order to minimize muon decay background from pions and kaons and reduce the particle flux into the muon spectrometer. The composite structure of the front absorber has been optimized in order to stop hadrons that punch through to the muon chambers

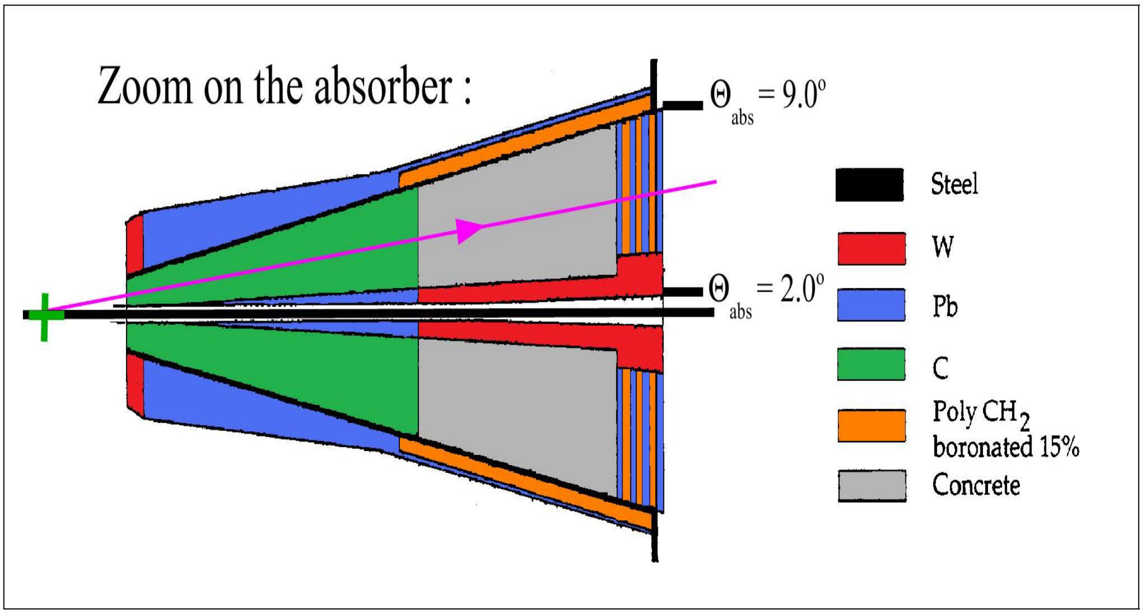

Figure 3.8: The Front Absorber [ABS]

and back-splash into the TPC region as small as possible. The front section consists of dense low-Z materials (carbon and concrete) to limit multiple scattering. The rear section contains multiple alternating layers of neutron moderator and absorber (boronated polyethylene) and a high-Z material (lead) to shield against neutrons and photons. Outside the muon arm acceptance, a tungsten cone located at an angle $\theta_{\text{abs}} < 2^{\text{o}}$ absorbs particles emanating from the beam pipe. At $\theta_{\text{abs}} > 10^{\text{o}}$ the absorber material is mainly lead, tungsten and boronated polyethlylene to reduce the particle load in the TPC. The Front absorber has a length of 4.13 m and a total weight of approximately 34 tonnes.

3.2.5.3 Small-angle beam shield

The small-angle beam shield is made of dense materials, that is, pure tungsten in the most critical regions nearest to the IP and a tungsten-lead mixture in other regions, further away from the IP, encased in a 4 cm thick stainless steel tube. Its outer envelop is pencil shaped, that is, follows the 2^{o} acceptance line up to a maximum radius of 30 cm and then stays constant up to the end of the spectrometer. The small angle absorber shields the beam pipe along the spectrometer extension. It protects the tracking detectors from particles produced at very small angles and from secondaries generated in the beam-pipe due to the beam gas interaction. The small angle absorber ends with an iron plug of 1.1 m in diameter and 1 m thick, which protects the trigger detectors against background particles.

3.2.5.4 Muon filter

The muon filter is a 5.6 x 5.6 x 1.2 m^3 iron wall placed at 15 m from the interaction point, between the last tracking station and the first trigger station. It reduces the background on the trigger stations by absorbing pions and low momentum muons. The combined effect of the front absorber and the muon filter prevents muons with momentum less than 4 GeV/c from reaching the trigger station and enhances the trigger chamber performance. A depth of 2.97 m of the trigger reduces punch-through high energy hadrons to a negligible level and improves the performance of the muon trigger.

3.2.5.5 The dipole magnet

The dipole magnet shown in Figure 3.9 is placed 7 m from the interaction vertex. The size is defined by the requirements on the angular acceptance of the spectrometer. The magnetic flux density (3 Tm field integral between IP and muon filter) is defined by the requirements on the mass resolution. It provides a horizontal magnetic field perpendicular to the beam axis. Its polarity can be inverted. The magnet yoke is constructed from 28 low-carbon steel modules made, for cost reasons, from existing steel stacks which consist of 3 m thick steel sheets welded to each other. The vertical poles are oriented at an angle of 9° with respect to the vertical symmetry plane. The two saddle-type coils have semi-cylindrical coil ends. They are constructed from hollow aluminium conductor with square cross-section of 25 x 5 cm^2 and an internal hole for cooling with demineralised water at a rate of some 130 m^3/hr. Each coil is assembled from 3 sub-coils with 4 layers of 14 turns each. They delimit the overall length of the magnet to 5 m. The distance of the centre of the dipole yoke from the interaction vertex is 9.87 m. The magnet was installed in its final position on a 3 m high reinforced concrete platform. The close distance between the solenoid magnet and the dipole leads to a strong magnetic force between the two magnets.

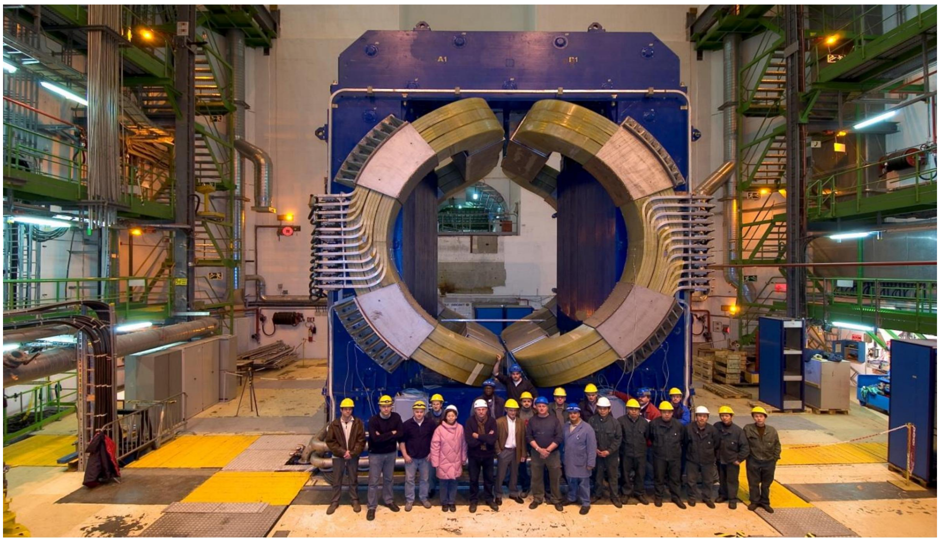

Figure 3.9: The dipole magnet [SWO98]

3.2.5.6 The tracking stations

The tracking stations [PAL07] shown in Figure 3.10 are MWPC with segmented Cathode Plate Chambers (CPC). Each plane is made up of 2 chamber planes, with 2 CPCs which are both read via the front-end electronics in order to obtain the two-dimensional hit information. The first station is placed right behind the absorber to measure the exit points of the muons as precisely possible. CPCs are chosen because they can be equipped with high granularity read-out needed to keep the occupancy at about 5 %.

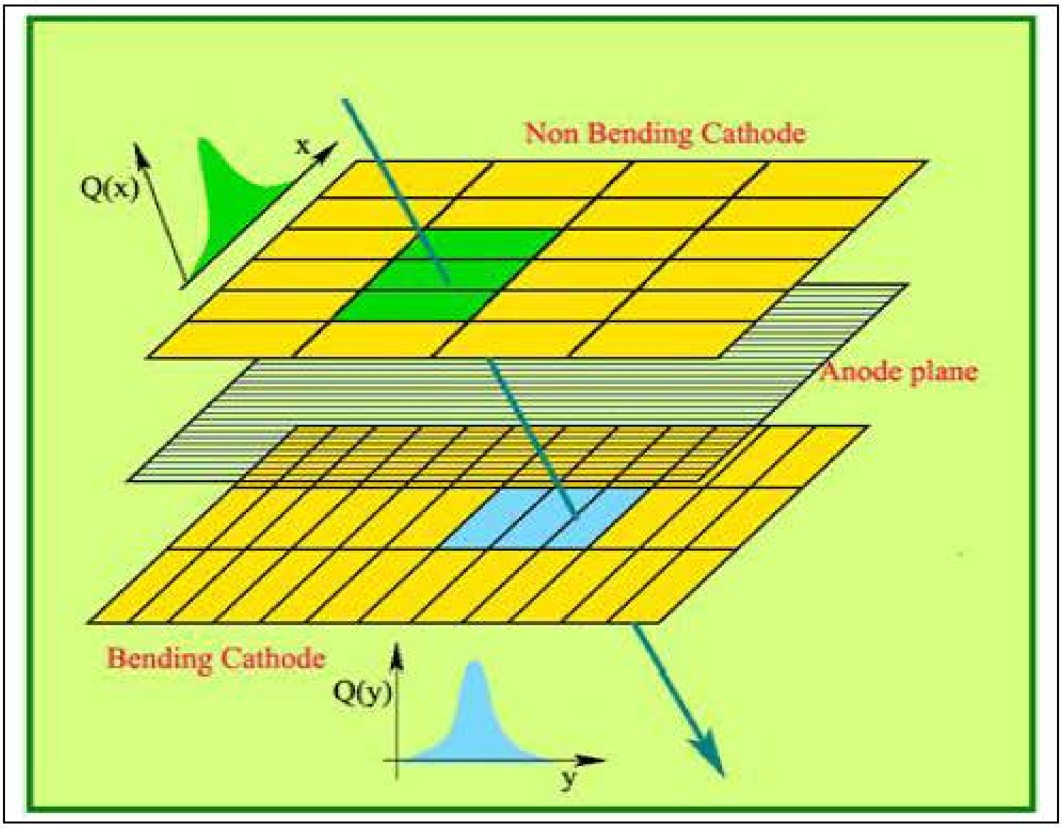

Figure 3.10: The Cathode Pad Chambers [PAL07]

Cathode pad chambers are used to determined the position of muons traversing the detector. When a muon (a charged particle) passes through the active gas volume of the detector, it produces ionization (electron ion pair) along its trajectories. These primary electrons drift towards the nearest anode wire where the avalanche takes place. The resulting ion cloud induces a charge distribution on the cathode pads close to the avalanche location by capacitive coupling. The pads of specific geometric shape are used to sample the charge induced on the cathode planes. The relative values of the induced charges on the pads determine the position of the charged particle passing through the detector.
Stations 1 and 2 are located between the front absorber and the dipole magnet. Each chamber of stations 1 and 2 consists of four independent quadrants. The four quadrants of each chamber are mounted into two independent support structures (aluminium frames) thus defining two independent half chambers at each side of the beam axis along the non-bending direction (x). The quadrants of stations 1 and 2 add-up to a total of 16 independent detection elements. Station 3 is located inside the dipole magnet and plays a crucial role in determining the track bending. In view of the large surface covered by station 3 a modular design based on a slat geometry is therefore used. Each chamber consists of 18 independent slats (see example in Figure 3.11) that are also mounted onto two independent support structures (carbon/epoxyfibre panels). Station 3 consists of a total of 36 detection elements. Finally, stations 4 and 5 are located between the dipole magnet and the muon filter wall. A slat geometry is also used for stations 4 and 5 and each chamber consists of 26 independent slats mounted onto two half chambers as in station 3. A total of 104 detection elements compose stations 4 and 5. Therefore, in total the tracking system consists of 156

independent detection elements, each providing two-dimensional hit positions. All detection elements were designed to provide a combined spatial resolution of 100 μm for the bending co-ordinate and 1 mm for the non-bending co-ordinate.

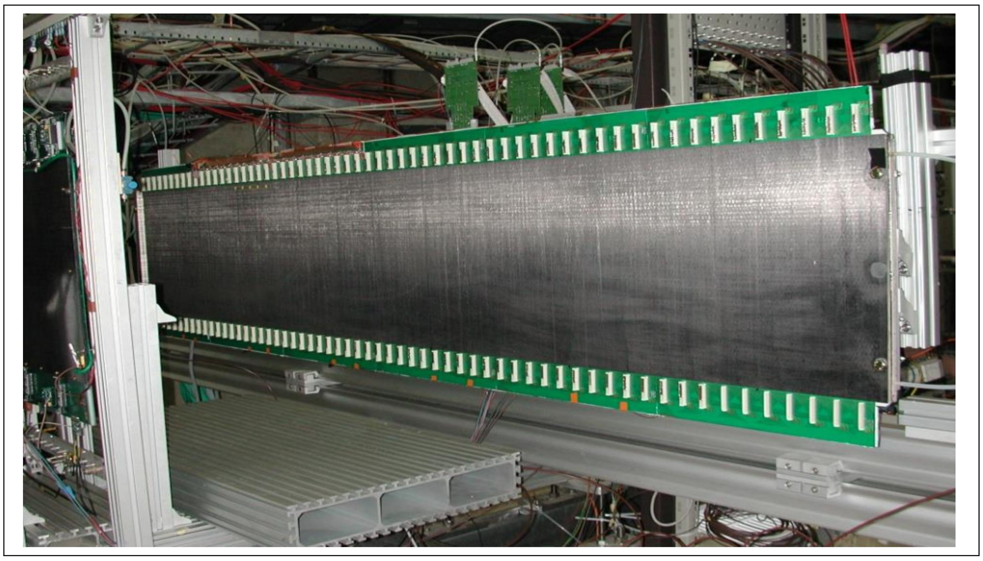

Figure 3.11: An example of the tracking chamber slat of the Muon Spectrometer [SER02]

3.2.5.7 The trigger system

The trigger system [BEV12] consists of four Resistive Plate Chamber (RPC) arranged in two stations placed 1 m apart from each other and located immediately behind the muon filter . The two stations MT1 and MT2, are placed at 16 m and 17 m respectively, from the IP. Each station is made of two parallel detection planes of 18 single-gap RPCs separated by 15cm, so that the total number of Resisistive Plate Chambers (RPCs) is 72. The active area covered by the first station is 6.12 x 5.44 m^2 and the second is 6.50 x 5.78 m^2. The larger dimension of the detection planes is along the vertical direction (bending plane), where the acceptance of the system extends from 2^o to 10^o, while in the non-bending plane it is in the range 2^o to 9^o. To avoid the inactive zones, the RPCs are positioned on a mechanical structure in two parallel planes, to allow superposition of active and dead areas. RPCs are read on both sides with copper strips. The horizontal strips (X) measure the coordinate along y direction (bending plane), while the vertical strips (Y) measure the coordinate along x direction (non- bending plane). In order to ensure a flat occupancy throughout the detection plane, the pitch and length of the strips increases with distance from the beam pipe, in proportion to the hit-rate per unit area. The pitch of the strips is also governed by the momentum resolution of better than 1 cm required for the p_T cut.
A total of 2100 RPCs, front-end channel and fast-decision electronics covering an area of 140 cm^2 are arranged in the 2 stations. RPCs are fast gaseous detectors that provide a muon trigger system. They consist of two parallel plates, a positively charged anode and a negatively charged cathode, both made of a very high resistivity plastic material and separated by a gas volume, see Figure 3.12. So when a muon passes through the chamber, electrons are knocked out of gas atoms and in turn hit other atoms, causing

an avalanche of electrons. The electrodes are transparent to the signal (the electrons), which are instead picked up by external metallic strips after a small but precise time delay. The pattern of hit strips gives a quick measure of the muon momentum, which is then used by the trigger to make immediate decisions on whether the measured muon satisfies the set criteria.

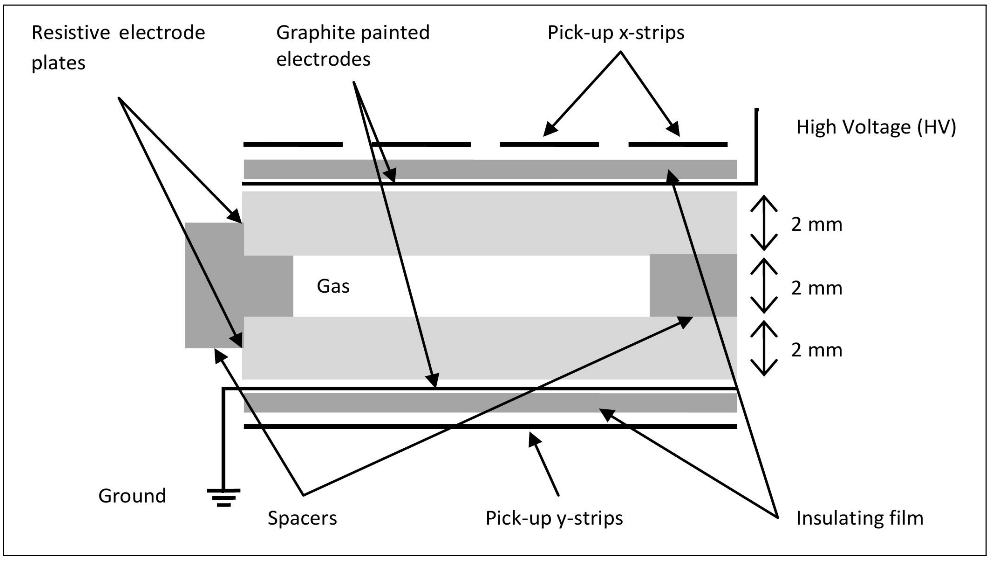

Figure 3.12: The Resistive Plate Chambers (RPCs) [CAR01]

The goal of the muon trigger system is to select unlike sign muon pairs from the decay of quarkonia and low-mass vector meson resonances, single muons from heavy flavors as well as $W^{\pm}$ and Z^0 bosons and like sign muon pairs for combinatorial background studies. Despite the momentum selection by the spectrometer, still a large number of background muons reach the trigger stations. The expected collision rate in Pb-Pb collision at nominal luminosity is about 8 KHz. The maximum trigger rate that can be handled by the Data Acquisition (DAQ) system is 2 KHz, so a simple trigger selection based on the presence of two muons is not sufficient. The majority of background is due to muons from pion and kaon decays and most of these muons have low p_T ($p_T < 1$ GeV/c). Therefore, to minimize the probability of triggering on these background events, a selection on the muon p_T value is applied according to the physics of interest.

3.2.5.8 Misalignment effects on the muon tracking and trigger system

The momentum and charge determination of muons relies on the position of the particle in the tracking and trigger stations. For example, to determine the momentum of the muon, the deflection of the particle track by the dipole magnet is considered and compared with the path of a particle with an infinite momentum. The infinite momentum muon fires the trigger with the same ID in both trigger chambers. The deviation between the position of this track and the deflected muon track is related to the momentum and charge of the muon. This relation has been studied using simulations [CAS07] and is stored in Look Up Tables which are read out during the trigger decision. The identification of the muon is done by matching the triggering muon in the tracking chambers. Therefore any misalignment of the detector elements will affect the geometry of the system and result in the mis-determination of the p_T and hence compromises the efficiency of both the tracking and trigger system.

3.2.5.9 The Geometry Monitoring System (GMS)

The p_{T} and the rapidity of the muons depends on the global position of the Spectrometer. Therefore the goal of the geometry monitoring system is to measure the displacements of the muon chambers starting from their initial positions measured during calibration runs (with straight muon tracks) done while the magnets are off. The geometry monitoring system, shown in Figure 3.13, is an array of 460 optical sensors placed on platforms at each corner of the tracking chambers. During the physics runs, when the magnets are switched on, images from all the optical lines are periodically recorded and compared to the references (initial positions). The image displacements obtained give information on the chamber displacements and deformations due to the magnetic field and the thermal expansion which can then be corrected.

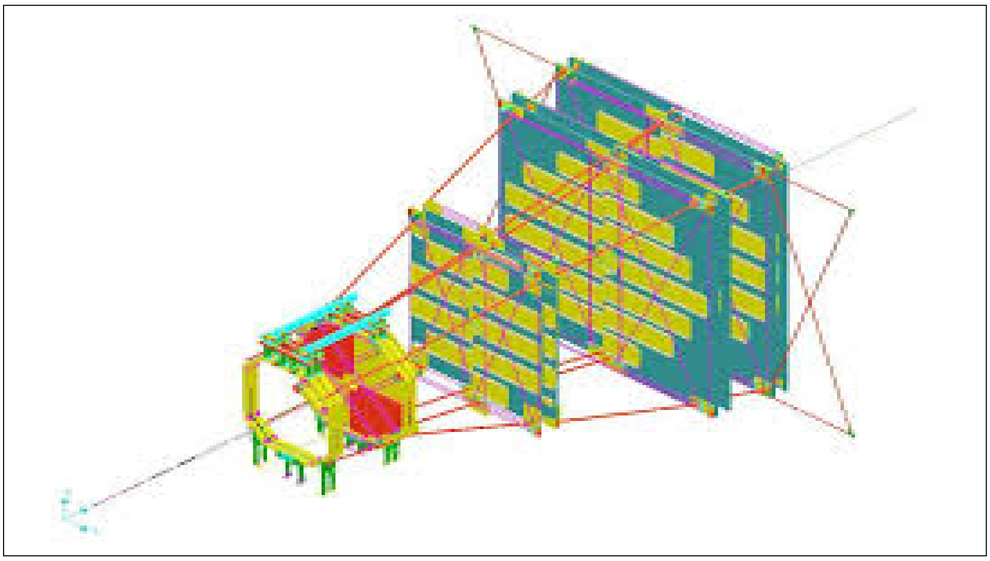

Figure 3.13: General view of the GMS setup showing the optical lines used to produce the images [GMS05]

3.3 The ALICE online data taking

The schematic representation of the Experiment Control System (ECS) shown in Figure 3.14 provides a unified view of the ALICE experiment and a central point from where all operations are initiated and controlled. It permits independent, concurrent activities on all parts of the experiment by different operators and coordinates the functions of the online systems for all the detectors within every partition (a group of particle detectors). The ECS handles the global operations by monitoring the Detector Control System (DCS) status of all the active detectors by interacting with the Run Control (RC) process that steers the data acquisition for the whole partition and by sending commands to the Trigger Partition Agent (TPA) that links the partition to the Central Trigger Processor (CTP).

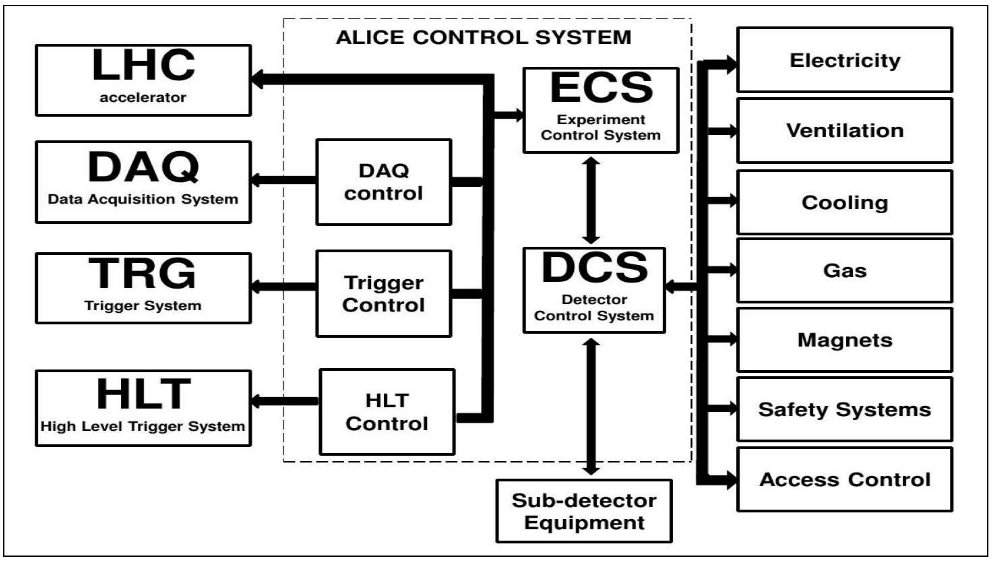

Figure 3.14: The ALICE Experiment Control System [ALI011].

3.3.1 The Central Trigger Processor (CTP)

The trigger signals from the detectors are collected and processed by the ALICE Central Trigger Processor (CTP). The CTP is designed to select physics events having a variety of different features and rates as well as to perform a scaling down of these rates in order to fit the bandwidth requirements of the acquisition system. It also has to cope with many different detectors which are busy at different periods following a valid trigger. The first trigger signal, called Level 0 (L0), arrives at about 1.2 μs after the collision. The L0 signals (24 L0 inputs) from the fastest detectors, such as the SPD, V0, T0 and the muon trigger system, are treated with a three states logic, i.e. asserted, not relevant and negated combined with logic AND and OR in order to select a certain class of events. The information of slower detectors is used to create a Level 1 trigger signal (L1) that is dispatched after 6.5 μs. The ALICE trigger system has been provided with a past-future protection circuit which looks for other events of requested types in a time window before and after the collision under investigation. This helps to reject pile-up events and improves the readout of the detectors. The last level of trigger is the Level 2, which waits for the past-future protection and arrives after 88 μs. The CTP data are stored both in the raw data stream and in dedicated scalers. In particular, there are scalers for all the inputs and for each trigger class that store the number of events passing each stage of the trigger (L0, L1, L2).

3.3.2 Data AcQuisition (DAQ) System

The ALICE DAQ system, whose architecture is shown in Figure 3.15, has been designed to cope with extremely challenging conditions. On one hand, it has to cope with the high interaction rate in proton-proton collisions with a relatively small event size and on the other hand it must provide resources for the smaller collision rate for lead-lead beams, but with a large amount of data, up to 1.25 GB/s sent to the storage facility. Also the design has been driven by the requirement of sharing the resources between different clusters of detectors which are set up to study different physics observables that have different cross sections and, consequently, different trigger rates.

For every bunch crossing in the LHC machine, the CTP decides within less than 1 μs whether to collect the data resulting from a particular collision. Once the CTP has decided to acquire a particular event, the trigger signal is dispatched to the front-end read-out electronics (FERO) of the involved detectors. The data is then injected in the Detector Data Link (DDL)[4] and sent to a farm of computers, called Local Data Concentrators (LDCs). The LDCs build the event fragments from the front-end electronics (FEE) into sub-events that are then shipped through an event-building network to the Global Data Collectors (GDCs) that take all the sub-events from the various LDCs and build the whole event and eventually send it to the storage facilities.

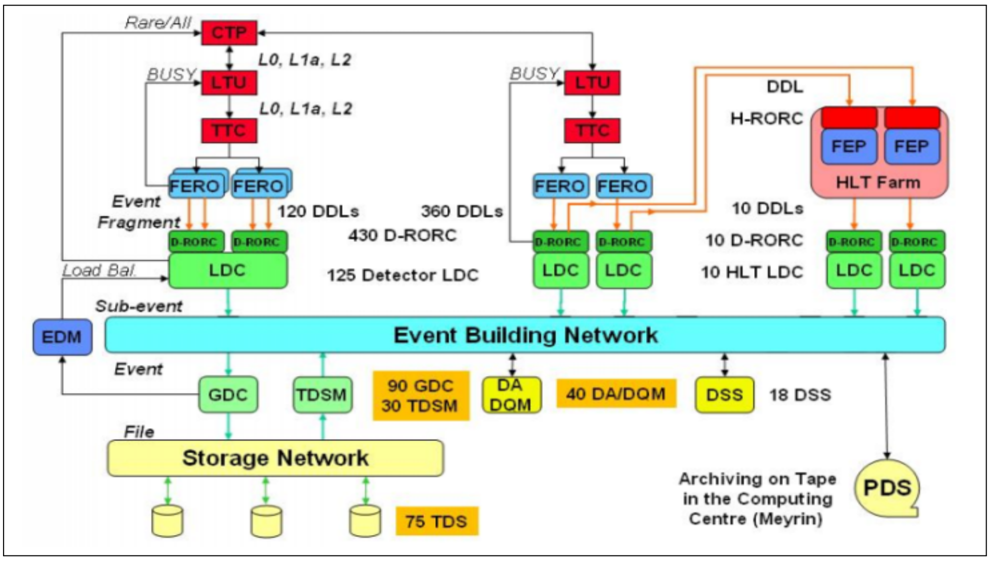

Figure 3.15: The Data Acquisition architecture [COL08]

3.3.3 The High-Level Trigger (HLT)

The need of a selection of interesting events and a data compression comes from the fact that the huge amount of data coming from the detectors (up to 25 GB/s in central events) cannot be treated by the DAQ and the storage facility because the bandwidth limit for sending data to the storage is about 1.25 GB/s. The High-Level Trigger (HLT) has been designed to collect raw data from the LDCs, to perform local pattern recognition and fast tracking, as well as primary vertex localization, and to build up the global event. The trigger decision, the Event Summary Data (ESD) of the event and the compressed data are sent back to the DAQ via the HLT DDL output. In order to meet these requirements the HLT consists of a farm of more than 1000 multi-processor computers. The HLT also has an online event display front-end that allows visualizing of events and monitoring the wellness of the data taking.

3.3.4 Detector Control System (DCS)

The primary task of the Detector Control System (DCS) is to ensure safe and correct operation of the ALICE experiment. It provides configuration, remote control, and

---

[4] DDL are an ALICE-standard, in ALICE there are more than 450 optical DDLs.

monitoring of all experimental equipment. The DCS is operational, throughout all operational phases of the experiment, including shutdown periods. Therefore, it is always available and reliable. In order to ensure a consistent control system and limit the resources needed to develop it, common solutions are developed for subdetectors and used wherever possible. The DCS hardware architecture is divided into three layers namely, the supervisory layer (PCs) which provide the user interface and the connection to disk servers or ALICE external systems; the intermediate control layer (PCs and PLCs) that collect and process information from the lowest (field) layer via field buses or the Local Area Network and forward them to the supervisor (and vice versa). The field layer contains all field devices (e.g. power supplies), sensors and actuators. The software architecture is built as a tree-like structure representing the structure of sub-detectors, their sub-systems and devices. The basic building blocks for implementation of the control hierarchy are Control and Device Units. The DCS uses an implementation based on Finite-State Machines (FSMs). These provide a mechanism to model the functionality and behaviour of a component. The architecture allows for the implementation of hierarchies of FSM working in parallel providing automation and error recovery. The software framework is based on the commercial SCADA (Supervisory Controls And Data Acquisition) system WINCC. The communication with the experiment's equipment uses a direct interface to WINCC as well as alternatives based on industrial standards or a specific CERN development. In addition to controlling all sub-detector equipment, the DCS also provides the interface to the various external services needed for the operation of the experiment such as gas, cooling, electricity, safety, etc.

As discussed above, the ALICE DCS is responsible for the coordination and monitoring of the various detectors and of central systems, for collecting and managing alarms, data and commands. Furthermore, it is the central tool to monitor and verify the beam status with special emphasis on safety. In particular, it is important to ensure that the detectors are brought to and stay in a safe state, e.g. reduced voltages during the injection, acceleration, and adjusting phases of the LHC beams. Some routine operations are executed when a particular beam mode is declared by the LHC, which represents a safety concern. These beam driven operations are implemented by the experiment as a tool for optimizing the efficiency of data taking, while improving the safety of the experiment. To successfully carry out these operations the LHC and the experiment control rooms communicate via the "handshake" following a predefined protocol to announce some beam operations. In the following sections I will discuss some aspects of the "handshake" in relation to the LHC modes and some of the important beam modes relevant for data taking in ALICE.

3.3.5 LHC operations

The LHC has two modes namely, the accelerator mode and the beam mode. The accelerator mode, summarised in Table 3.1 provides a summary of the LHC machine state.

The LHC assumes different beam modes [BCG+14], shown in Figure 3.16, in its operation which follow a strict sequence to enable its transition to the next step. The following is a description of beam modes and handshakes that occur at each transition between the LHC and the ALICE experiment.

Accelerator Mode	Description	
Shut Down	Cold magnets floating	No Beam
Proton Physics	Beam based operation aimed at proton physics	Beam
Ion Physics	Beam based operation aimed at physics	Beam
Proton-Ion Physics	Beam based operation aimed at proton-ion physics	Beam

Table 3.1: Examples Of LHC Accelerator Modes [BCG+14]

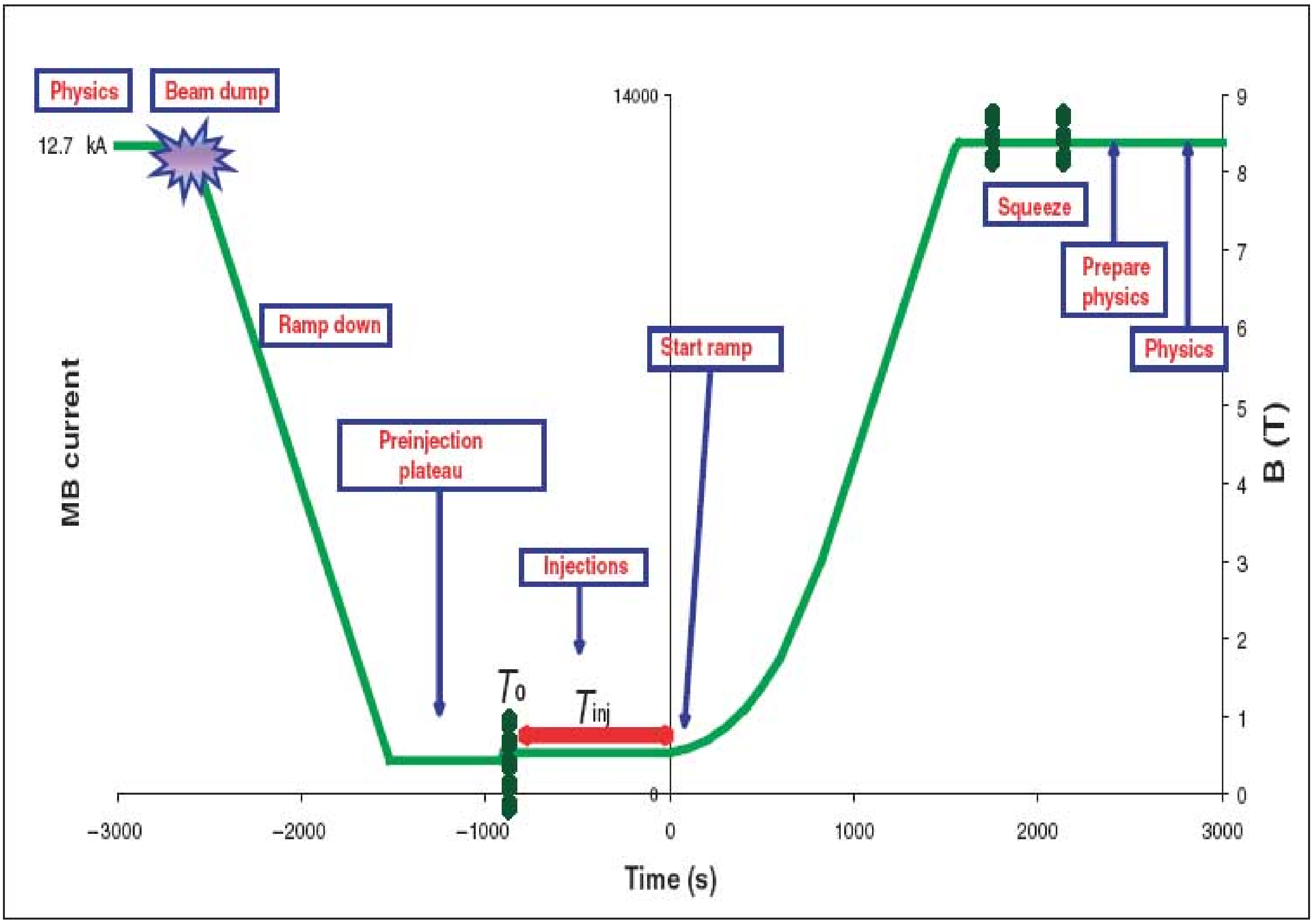

Figure 3.16: The LHC beam modes [LHC12]

- SETUP

In the SETUP mode the beam is in the transfer lines. This includes pre-injection plateau and injection plateau (see Figure 3.16). In this mode there is no beam in the LHC ring.

- INJECTION PROBE BEAM

Either ring 1 or ring 2 will be injected with a beam or has a safe beam circulating. Some checks are done on the subsystems of the accelerator before injecting higher beam intensities. The aim of this mode is to establish a safe circulating beam with a given lifetime.

- INJECTION SET-UP BEAM

During this mode measurements are possible but with very limited precision. In order to make more precise measurements before filling for physics, a SET-UP BEAM may be used. The beam will be wholly representative of the physics beam to follow, just with fewer bunches to stay below the damage threshold. The LHC opens the INJECTION HANDSHAKE [BC03], announcing the injection of beam, the ALICE experiment moves to an operation mode SAFE which requires that all detectors are in a similar state called SAFE, which is a specific condition for every detector and is associated with a specific High Voltage (HV) data point.

- INJECTION PHYSICS BEAM

At this stage the machine has been optimized and has circulating beams with the appropriate lifetimes and it is ready to accept higher intensities needed for physics. At this mode the accelerator is empty, therefore, prior to high intensity beam injection, a pilot beam is injected.

- PREPARE RAMP AND RAMP

When the injection is complete, the machine is preparing to RAMP. This means that the beam energy is brought to the required value by increasing the currents of the superconducting magnets of the LHC. At this stage, a particular set of detectors (the luminometers e.g. V0s and timing detectors e.g. T0) is activated, but the other detectors stay SAFE. The transition to LHC beam mode RAMP automatically triggers the DCS and CTP to check the LHC clock quality, and to raise a DCS alarm and perform an automatic resynchronization of the LHC and ALICE clocks.

- FLAT TOP

FLAT TOP occurs when the machine has finished ramping and the beam is at the required energy. This mode ensures that the optimal energy reached can be maintained consistently for the required period of the collisions.

- SQUEEZE AND ADJUST

The beams are focused by adjusting the emittance[5] to ensure collisions, thereby raising the intensity of the beam. This is the SQUEEZE mode. This is followed by ADJUST which implies that the path of the beam is being adjusted in order to enable collisions. When the beam mode is FLAT TOP, SQUEEZE, or ADJUST calibration runs are performed in preparation for data taking. For example, at this point the muon tracking chambers take a pedestal run - noise calibration for the front-end electronics (FEE) of the tracking chambers. At this stage the LHC CTP clock should be synchronized with the LHC clock.

---

[5] The smallest opening the beam can be squeezed through.

- STABLE BEAMS

The STABLE BEAMS mode means that collisions are occurring at the experiments with backgrounds and lifetimes under control. When the STABLE BEAMS condition is declared and the background conditions allow i.e. the ALICE target instantaneous luminosity has been set accordingly by the LHC, all the remaining detectors are sent to READY. Small adjustments of beam parameters are allowed in this mode. In case of degradation, all experiments are warned and the machine is switched to the ADJUST mode when all experiments have confirmed to be ready for the switch, however the UNSTABLE BEAMS mode may be assumed without prior warning to the experiments in case of beam degradation. It is an emergency mode. The machine is switched to RAMP DOWN mode at the end of each physics fill (See section 3.3.6). A programmed dump is executed, followed by beam energy ramp down. A BEAM DUMP may also occur, either programmed or not, the data taking is stopped and the experiment is brought to a SAFE condition in case a new injection is expected. A pedestal run may be done also to calibrate the FEE again in case of a BEAM DUMP.

When stable beams have been declared all detectors may be turned on to start data taking. The configuration of the detectors depends on the interaction rates measured by the V0 detectors and the filling scheme. The experiment can then be monitored to make sure that its configuration is correct and all the detectors taking part in data taking are configured correctly. Other parameters to be monitored during the collisions and data taking are the event and data sizes as well as the busy time of the detectors.

3.3.6 LHC Automatic Filling Scheme (AFS)

Each period of data taking has a different bunch filling scheme[6] which depends on the luminosity and the cross section required for the physics of interest for each experiment. Bunch filling schemes allow the tuning of the luminosity[7] to meet the requirements of experiments. The 25 ns scheme is the principal scheme for high luminosity operation. The characteristics of each scheme determine the number of bunches in the LHC ring. The general configuration for bunch filling is as follows;
Base structure: [COL05]
<spacing> _ < Nb > b _ < IP1/5 > _ < IP2 >_ < IP8 > _ < code >

Where:

< spacing > = Single, or 2025ns, or 525ns, or 75ns, or 50ns, or 25ns, etc. This refers to the characteristic bunch spacing, given in time units, in the main injector batches used for the given filling scheme. Single means that single bunches are injected into the LHC.

< Nb > = total number of bunches per beam for the given filling scheme (normally, identical for both beams). If a probe bunch is kept (i.e. not overinjected), it is not counted in the total number. The presence of a non-overinjected probe bunch is encoded in the suffix < code >.

---

[6] Trains of proton bunches injected at regular intervals into the LHC ring.

[7] The ratio of the number of events detected (N) in a certain time (t) to the interaction cross section (σ) L = $\frac{1}{\sigma}\frac{dN}{dt}$).

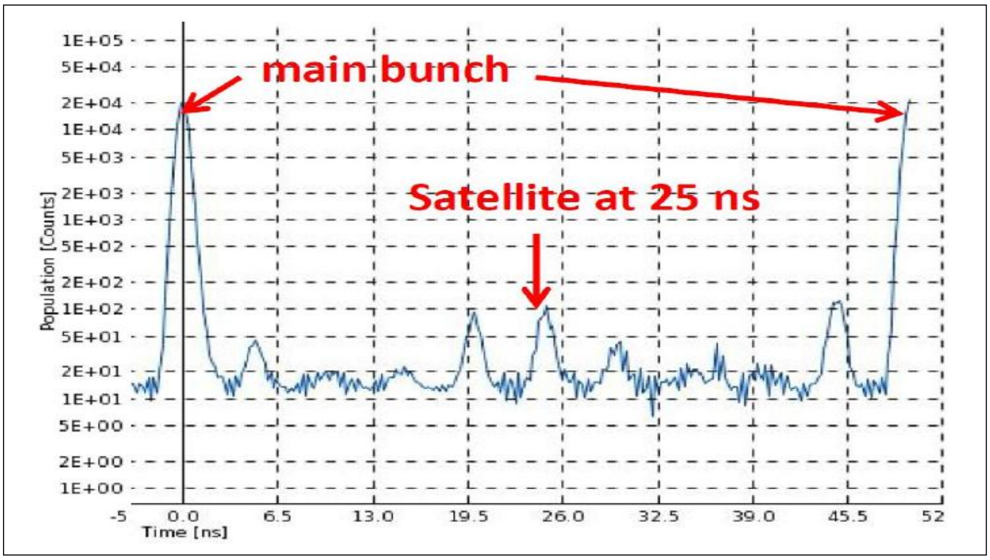

Figure 3.17: Main and satelite bunches [JAK14]

< IP1/5 > = expected number of colliding bunch pairs in IP1 (or IP5) for the given filling scheme. IP1 and IP5 are where ATLAS and CMS detectors are located in the LHC ring respectively.

< IP2 > = expected number of colliding bunch pairs in IP2 for the given filling scheme. IP2 is where ALICE is located.

< IP8 > = expected number of colliding bunch pairs in IP8 for the given filling scheme. IP8 is where LHCb is located.

< code > = a free suffix to encode variants of a filling scheme.

3.3.7 ALICE run conditions for pp collisions in 2012

The filling scheme used in 2012 for the V0 triggered data collected considered in this analysis is as follows:-

50ns_1374_1368_0_1262_144bpi12inj

The characteristic bunch spacing was 50ns. The total number of beam bunches was 1374, with 1368 beams colliding in ATLAS and CMS and only 1262 in LHCb. The zero given for the bunches colliding in ALICE means that instead of main-main beam collisions the LHC delivered what is reffered to as **main-satellite** collisions to ALICE at IP2. This is because the ALICE experiment is optimized for heavy-ion collisions therefore cannot handle instantaneous luminosities above 10^{29} cm^{2}s^{-1} for pp collisions. This is partly solved by allowing collisions between high intensity proton bunches (main bunch) and low intensity ones (satellite bunches) Figure3.17. These collisions are called main-satellite collisions.

Different trigger classes are used to describe the beam interactions. The trigger clusters[8], as well as trigger requirements during data taking depend on the require-

---

[8] Group of detectors read together in the CTP.

ments of the physics of interest. For example, for the data taking period of interest in this study, the data sample from period LHC12h and LHC12i pp collisions triggered by the V0 detector, the following trigger classes were used :-

CINT7-S-NOPF-ALLNOTRD and CMSH7-S-NOPF-ALLNOTRD.

In the above configuration the first term i.e. CINT7 refers to the minimum bias (MB) trigger which is a coincidence of the V0-A and V0-C with the SPD and measures the minimum events and CMSH7 refers to the muon trigger for high-p_T single-muon measurement, which in addition to the V0-A and V0-C includes the muon trigger. The p_{T} threshold for the two triggers is $\gtrsim$ 1 GeV/c and $\gtrsim$ 4.2 GeV/c respectively. The S denotes satellite collisions, NOPF means there is no-past-future-protection and lastly ALLNOTRD shows the trigger cluster to be read if trigger conditions are satisfied. A summary of the detector conditions during data taking in pp collisions in 2012 is shown in Table 3.2

Table 3.2: A summary of the data taking conditions for pp collisions in 2012.

Beam Type	pp
Beam Mode	Stable Beams
Beam Energy	4 TeV
Beta Star	3 m
Interacting bunches	0
L3 Magnet Current	-30 kA
Dipole Magnet Current	-6 kA
Partition	Physics

3.4 ALICE offline framework

AliRoot is the ALICE offline framework for simulation, reconstruction, and analysis of experimental and simulated data. Its architecture is shown in Figure 3.4. It is based on the ROOT [BRU95] framework and the code is written in C++. The AliRoot functionalities are summarized in two main steps: simulation and reconstruction. Figure 3.4 shows the interaction of the reconstruction code with the other parts of AliRoot. In the simulation, event generation, transport and digitization are performed while in the reconstruction, raw data are produced and cluster (see section 3.4.4.1) finding and track reconstruction are applied.

3.4.1 Event generation

A hadron collision is simulated by an event generator (PYTHIA [PST13], PHOJET [PRJ96], or HIJING [HXM94]) that is interfaced with AliRoot. The kinematic-tree produced stores the full information about the generated particles (type, momentum, charge, production process, originating particle and decay products).

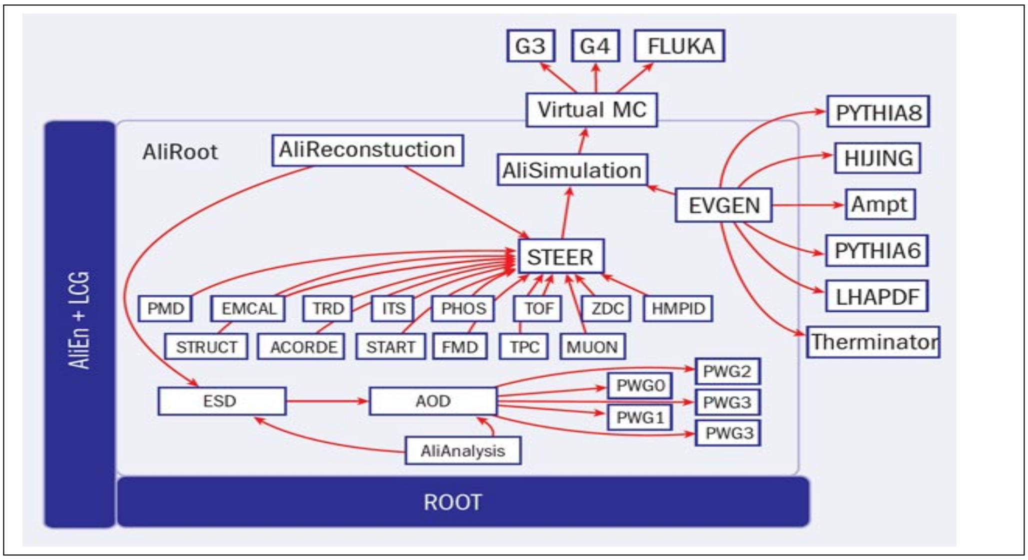

Figure 3.18: The AliRoot Framework [ALI02]

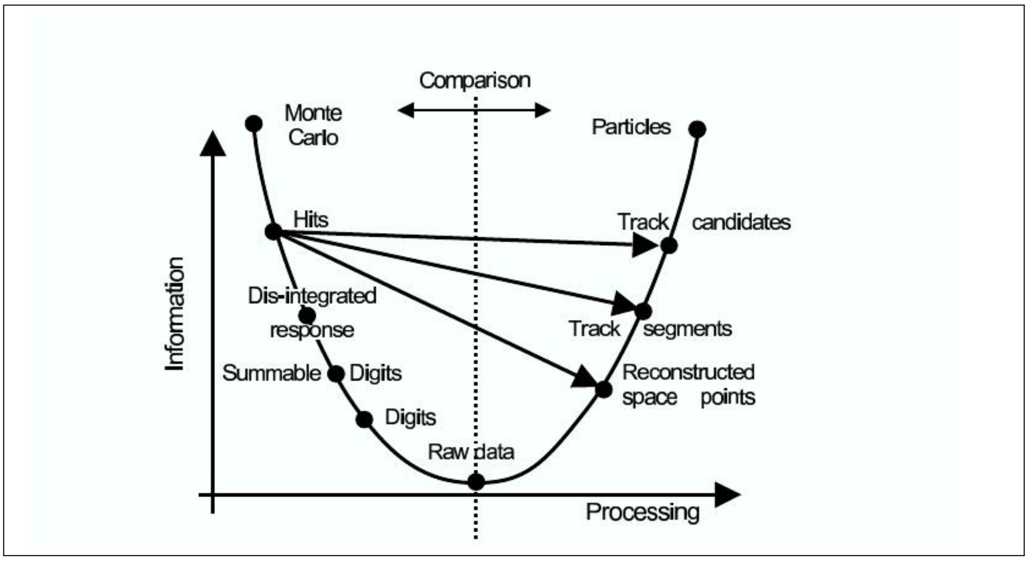

Figure 3.19: A schematic depiction of the functionality of AliRoot Framework [ALI02]

3.4.2 Particle transport

When particles are propagated through the detector material they can interact with matter, decay and create additional particles. These new particles have to be propagated through the detector as well. Consequently, the total number of particles after the transport process is significantly larger than the number of particles created in the initial generation step. During this process all interactions of particles with sensitive detector parts are recorded as hits that contain the position, time and energy deposit of the respective interaction. The track references are stored, mainly needed for the debugging of the reconstruction algorithms. Programs that perform the transportation of particles and interfaced with AliRoot are GEANT3 [APO94] and FLUKA [FER05].

3.4.3 Digitization

If a particle produces a signal in a detector element (hit), objects are created that consist of the sum of the deposited energy by all hits so that there is only one digit. The energy in this digit is transformed into Analogue-to-Digital Converter (ADC) amplitude units. The corresponding digital output of the detector is stored as a summable digit, taking into account the detector's response function. The electronic noise is added and digits whose energy does not pass the required energy threshold are eliminated. Summable digits allow events to be merged without duplication of electronic noise. In the last step, the data is stored in the specific hardware format of the detector (raw data). At this stage the raw data corresponds to the signals that would be produced by an interaction of the same kind within the detector.

3.4.4 Raw data

Raw data corresponds to the signals produced by an interaction within the detector. The subsequent reconstruction is identical, both for simulated as well as real events and consists of the following steps.

3.4.4.1 Cluster finding

Particles that interact with the detector usually leave a signal in several adjacent detecting elements or in several time bins of the detector. In this step these signals are combined to form clusters. This allows the exact position or time of the traversing particle to be determined and reduces the effect of random noise. Overlapping signals from several particles in a single cluster are unfolded. This step is performed for each subdetector where, due to the different nature of the subdetectors, the implementations vary significantly.

3.4.4.2 Track reconstruction

The track reconstruction starts when the clusters are combined to form tracks that allow the track curvature and energy loss to be calculated with the aim of determining their momentum and particle type. The tracking is a complex global procedure, but at the same time individual per detector. The global central barrel tracking starts from track seeds in the TPC, which are found by combining information from the few outermost pad rows under the assumption that the track originates from the primary vertex, which is defined as the point where the interaction happened. Tracks are then followed inwards using a procedure called the Kalman filter. Further information is updated on the track, for example, a noise term is added. It represents the information loss by random processes such as multiple scattering and energy-loss fluctuations. In the final step all clusters already associated to tracks are removed and the procedure is repeated without requiring that the seeds point to the primary vertex. The result, the so-called TPC-only tracks to which only TPC information contributes, is saved in the reconstruction output. Subsequently, these tracks are complemented with information from the ITS, TRD, and TOF as well as HMPID if the track is in the detector acceptance which produces so-called global tracks.

Among the track finding algorithm in single detectors is the SPD tracklet finding. The event vertex as well as the tracklets are reconstructed by forming straight lines out of a cluster in each of the two SPD layers. The event vertex is reconstructed where most of these lines intersect as shown in Figure 3.20.

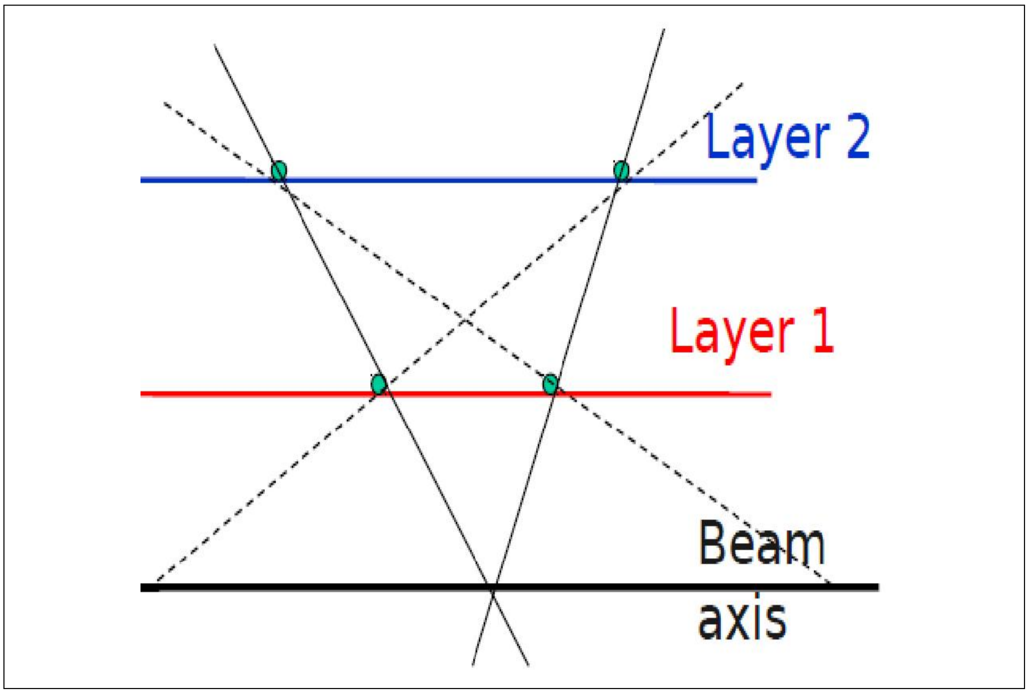

Figure 3.20: A schematic of the vertex reconstruction

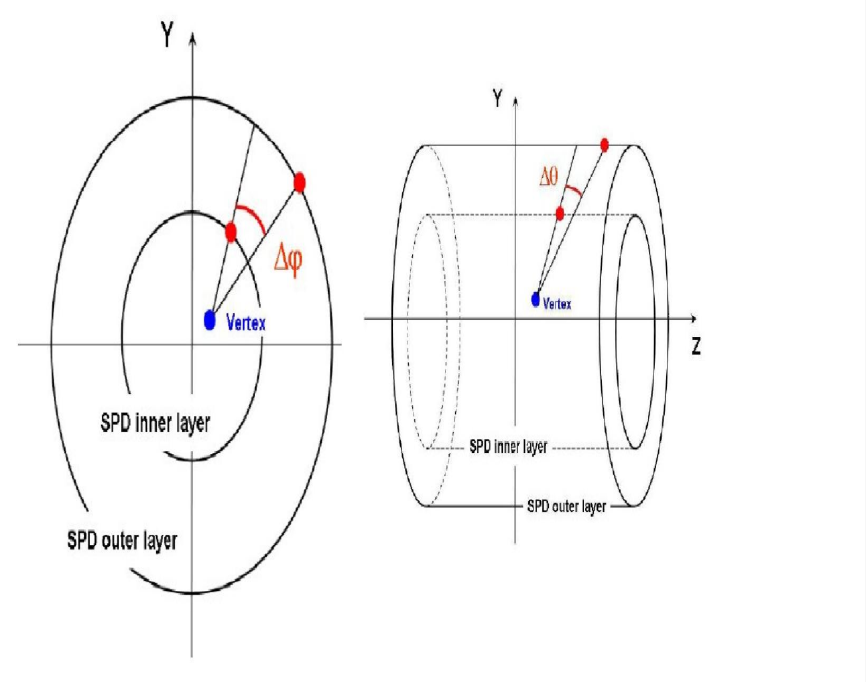

Figure 3.21: A schematic of the tracklets reconstruction

A tracklet is identified by drawing a line joining two hits deposited by the charged particle on the two layers of the SPD, extrapolated to the interaction vertex, as shown in Figure 3.20. A tracklet is represented by η, φ, $\Delta\varphi$[9], the quality parameter of the tracklet and the primary vertex position because tracklets originate by constructing from the vertex, as shown in Figure 3.21.

Primary-vertex reconstruction
Information from clusters in the SPD, tracks in the TPC and global tracks are used to find the primary vertex position of the interaction. The vertex position can also be used to estimate the track parameters.

Secondary-vertex reconstruction
Tracks are combined to find secondary vertices in order to reconstruct, for instance, particles like pions (π) and protons (p) from lambda (Λ) decay, $\mathit{\Lambda}^0 \rightarrow p\pi$. For this purpose, opposite-sign tracks that originate sufficiently far away from the primary vertex are combined. If the closest approach and the topology of the two tracks is consistent with a decay, the pair is accepted as a potential secondary vertex.

The output of the reconstruction is called Event-Summary Data (ESD) and contains only high-level information such as the position of the event vertex, parameters of reconstructed charged particles together with their PID information, positions of secondary vertex candidates, parameters of particles reconstructed in the calorimeters and integrated signals of some subdetectors. This data is further reduced to Analysis-Object Data (AOD) format which is a summary of the reconstructed event and contains sufficient information for common analysis. Therefore, the transformation procedure may already contain a part of the analysis algorithm, for example track selection. Several AODs, focusing on different physics studies, can be created for a given event. The reconstruction framework is shown in Figure 3.22. It shows the stages from digits through to ESDs.

The ALICE Collaboration has different Physics Working Groups (PWGs) that require different information on the data to satisfy their analysis needs. Both ESDs and AODs are stored on the ALICE Grid described in detail below and accessible to users as **.root** files[10]. In this work we analysed AOD data from muon_calo_pass2 reconstruction.

3.5 The ALICE grid

The grid is a global collaboration of computer centres around the world that provide resources to store, distribute and analyse data generated by the ALICE experiment. The structure of the ALICE grid is shown in Figure 3.23. To access these resources a user is required to have a grid certificate which is obtained via an authorised administrator of the Virtual Organisation (VO) subscribed to the ALICE grid. Access is granted via ALIEN - the ALICE Environment. Users make job requests from one of the many entry points into the system. A job request can be storage, processing capacity, or availability of analysis software. The grid establishes the identity of the user,

---

[9] $\Delta\varphi$ is defined as $\varphi1$ - $\varphi2$, where $\varphi1$ ($\varphi2$) is the azimuthal angle between the event vertex position and the cluster in the first (second) layer.

[10] A file in which ROOT stores information.

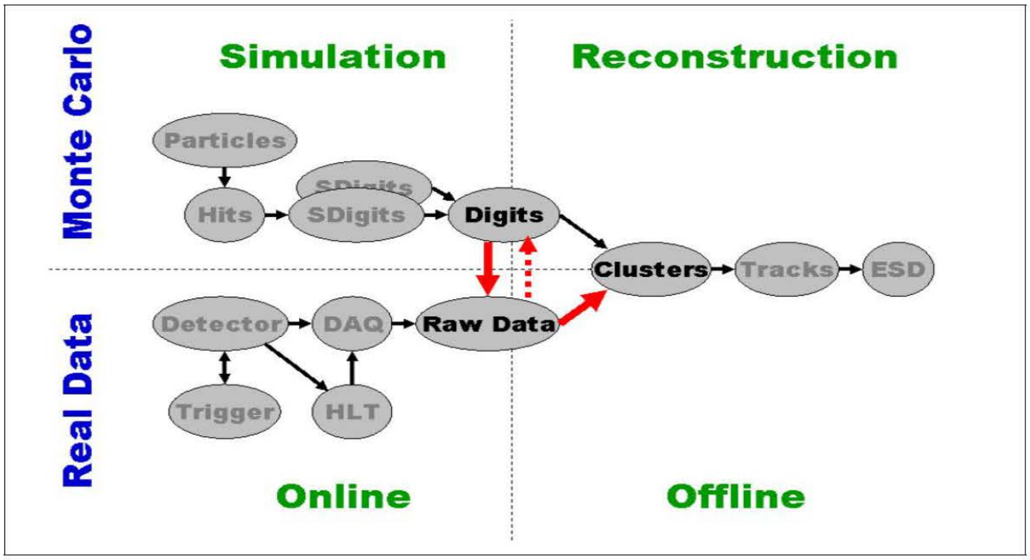

Figure 3.22: The Reconstruction Framework [ALI03]

checks their credentials and searches for available sites that can provide the resources requested. The Tier-0 is the computing centre at CERN, the site hosting the experiment. Its computing centre has a special role, it records all original data to permanent storage and performs the initial processing of the data to provide rapid feedback to the operation. The processed data is then sent to other computing centres for analysis. Tier-0 also provides analysis capacity for local users. The Tier-1 consists of eleven large computing centres around the world. They receive data directly from CERN and provide additional permanent storage and the computing resources for reprocessing of the data, required at a later stage in the analysis. The centres are also responsible for the collection of simulated events produced at higher Tier centres. Tier-2 consists of even a large number of computing centres (about a hundred) whose role is to provide the bulk of computing resources for simulation and analysis. Typically they are associated with large disk storage to provide temporary storage of data that is required for analysis. A Tier-3 centre consists of a large number of smaller computing centres at various universities and laboratories, whose main role is to provide analysis capacity for local users.
ALICE approved software, AliRoot [ALI02] is supported on LINUX (UBUNTU, Scientific Linux) and other Open Source operating systems. The ALICE grid is monitored on the web via MonALISA. Both data and analysis packages are made available to users who possess ALICE approved grid certificates.

The data analysis of the V0-triggered data sample, comprising of the minimum bias events as well as high p_{T} single muon triggered events using the AliRoot framework on the ALICE grid will be discussed in Chapter 4.

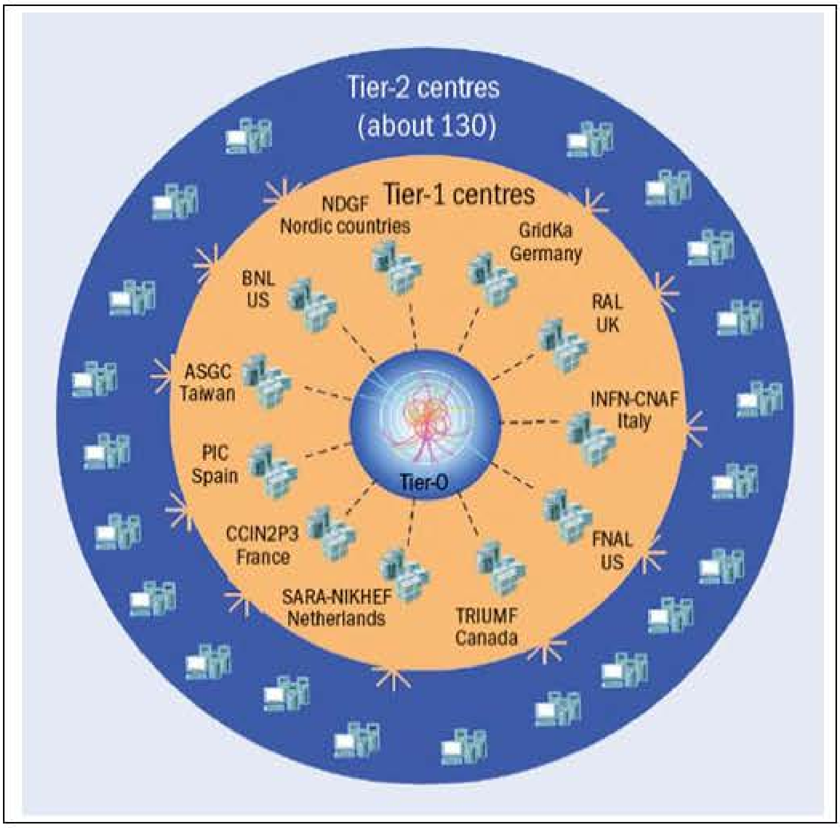

Figure 3.23: The GRID Tiers [ALI04]

Chapter 4

Analysis : Heavy flavour muons vs charged-particle multiplicity

Here we discuss the details of the analysis of data collected by ALICE in 2012 during pp collisions at 8 TeV centre-of-mass energy at the LHC. The aim of this analysis is to investigate the correlation between the production yield of single muons from heavy flavour decays and charged-particle multiplicity. The analysis strategy, method used to compute the multiplicity of charged particles and to determine the number of high-p_{T} single muons as well as their yields and cross sections are given. The simulation procedure by means of Monte Carlo based event generator is also discussed.

The analysis procedure followed in this study is based on the AliRoot [ALI02] offline framework discussed in detail in section 3.4.

4.1 Event selection cuts

The details that follow in this discussion concern the criteria adopted to select runs and events used in the data sample analysed in this study. Henceforth we discuss the offline event selection implemented in the analysis task used for charged-particle multiplicity.

4.1.1 Data sample

The data analysed in this study was recorded by ALICE during pp collisions at 8 TeV at the LHC in 2012. The sample is composed of data taken from two periods of interest in this study namely LHC12h and LHC12i data in which the V0 detector provided the minimum bias (MB) trigger. The corresponding integrated luminosity was 583 ± 29 nb^{-1} [ABT].

Only runs that passed the ALICE Quality Assurance (QA) checks of the physics analysis are selected. The conditions to be satisfied in the QA are listed in Table 4.1, while Table 4.2 shows the number of runs per period considered for this analysis. The final runlists can be found in Appendix A.1

Table 4.1: Quality Assurance (QA) physics analysis

Period	LHC12h and 12i
Run Type	Physics
Beam Mode	Stable
Trigger Detectors	At least Muon Trigger
Readout Detectors	At least Muon Tracking, Muon Trigger and SPD
Run Quality	Not bad for readout detectors
Run Duration	$\geq$ 10 min

Table 4.2: Total number of runs per period finally used in this analysis.

Period	**Number of runs**
LHC12h	114
LHC12i	17

4.1.2 Event selection cuts

To make sure that the data sample contains events of interest to this study, i.e. high transverse momentum (high-p_{T}) single muons, specific selection cuts are applied to the events and tracks offline. The following cuts are applied for multiplicity measurement.

- **Physics selection**

  The physics selection is a tool used to reject background and poor quality events. This helps to keep beam-induced backgrounds at a minimum during the creation of AODs. The tool selects the physics events and the interaction trigger i.e.

events that have trigger on bunch crossings. Furthermore, the events should satisfy the online trigger conditions replayed using offline signals. The events should be flagged as valid by either the V0A or V0C 3.2.4.4. After the physics selection, quality assurance checks are performed on the created AODs from the muon_calo_pass2 reconstruction, see Table 4.1.

- **Trigger selection**

  The data sample consists of minimum bias (MB) and Single Muon High $\mathrm{p_T}$ (CMSH) triggered events. The two triggers are described in Chapter 3, section 3.3.6. The MB trigger ensures the measurement of all allowed events while the CMSH trigger ensures the measurement of events that have at least a high-p_{T} single muon accomplished by checking that the triggering detectors include V0A and V0C and the muon trigger system.

- **Reconstructed vertex**

  Only events coming from the primary vertex, $\mathrm{Z_v}$, and inside the SPD vertex are considered, $|\mathrm{Z_v}^{\mathrm{SPD}}| < 10$ cm. At this region the efficiency of the detector is well defined for vertex determination. In addition to the vertex and SPD geometry, it is required that all considered events should contain at least a charged particle and the number of contributing tracklets ($\mathrm{N_{contributors}}$) to the reconstructed SPD vertex is required to be greater than zero. In this way events without any charged particles are rejected. To ensure accurate estimation of the charged particles measured per event, the resolution of the SPD should be better than 0.25 cm. Furthermore, since the primary vertex is more accurate in estimating the vertex position, a cut which requires that the difference between the primary vertex and the SPD vertex of each accepted event be less than 0.5 cm, is applied. The ”vertexer tracks” and the ”vertexer : Z” are labels tagged on events with more than one reconstructed tracklet. Applying these cuts further improves the measurement by rejecting events with one tracklet. A summary of the cuts applied in the vertex selection are listed in Table 4.3.

Table 4.3: ”Good vertex” selection cuts

$\lvert\mathrm{Z_{vtx}}\rvert < 10.0$ cm
$\mathrm{N_{contributors}} > 0$
$\sigma_{\mathrm{Z_v}^{\mathrm{SPD}}} < 0.25$ cm
$\lvert\ \mathrm{Z_v}\ \text{-}\mathrm{Z_v}^{\mathrm{SPD}}\ \rvert < 0.5$ cm
Vertex title does not contain ”VertexerTracks”
Vertex title does not contain ”vertexer: Z”

The complete structure of the analysis task (AliAnalysisTaskPtCMSH.cxx) is shown in Appendix A.2. Here we give only relevant pieces of the code utilised in the analysis. The cuts are implemented as follows in the analysis task;

```
// retrive the AOD event
fAOD = dynamic_cast<AliAODEvent*>(InputEvent());
if (!fAOD) {
printf("ERROR: fAOD not available\n");
return;
}

// trigger classes selection

TString trclasses = fAOD->GetFiredTriggerClasses();
if( ! trclasses.Contains(ftrclasses) ) return;

// check for a good vertex
const AliAODVertex* trkVtx = fAOD->GetPrimaryVertex();
if (!trkVtx || trkVtx->GetNContributors()<=0) return;
TString vtxTtl = trkVtx->GetTitle();
if (!vtxTtl.Contains("VertexerTracks")) return;
AliAODVertex *vz = fAOD->GetPrimaryVertexSPD();
if (vz->GetNContributors()<=0) return; // number of contributors
TString vtxTyp = vz->GetTitle();
Double_t cov[6]={0};
vz->GetCovarianceMatrix(cov);
Double_t zRes = TMath::Sqrt(cov[5]);
if (vtxTyp.Contains("vertexer: Z")&&(zRes>0.25)) return;// resolution
 cut
if (TMath::Abs(trkVtx->GetZ() - vz->GetZ())>0.5) return; //difference
 between the main vertex and the SPD
if ( vz->GetZ() < -10. || vz->GetZ() > 10. ) return;  //SPD vertex cut
```

Table 4.4 shows the summary of the number of events obtained before and after the event and track selection in this study. About 6% and 3% MB events are rejected in period LHC12h and LHC12i, respectively and about 4% CMSH events are rejected for both periods after event and track selection is applied. The distribution of events as a function of the vertex position for both periods LHC12h and LHC12i are shown in Figure 4.1. The distributions follow a Gaussian shape in the optimised region of $\mathrm{Z_v}^{\mathrm{SPD}} = 10$ cm.

4.2 Measurement of charged-particle multiplicity

Multiplicity is the number of charged particles produced in an event. In this study the charged-particle multiplicity is estimated using the number of tracklets from charged primary particles[1] reconstructed in the SPD extending the pseudorapidity to $|\eta|< 1.0$ and vertex position $|\mathrm{Z_{vtx}}| \leq 10$ cm to minimize loss of events. Particles that hit the two layers of the SPD in conjuction with the SPD vertex position are used to reconstruct tracklets. A straight line joining the two hits and pointing to the SPD vertex

---

[1] Charged primary particles are all charged particles produced in the collision, including their decay products, but excluding products of weak decays of strange particles.

is considered as a candidate tracklet from a charged particle.
The number of reconstructed tracklets is the estimator of the multiplicity. The raw multiplicity distributions measured for both the MB and CMSH triggers in the acceptance of the SPD, are shown in Figure 4.2. The slope of the figures show that CMSH events select a higher number of reconstructed tracklets (multiplicity) than MB events. This is because CMSH select high-p_{T} muons ($p_{\mathrm{T}} \gtrsim 4$ GeV/c), which includes all single muons resulting from hard scattering processes e.g. decays of heavy flavours, W and Z bosons which allow access to many parton-parton interactions leading to the production of more charged particles.

Table 4.4: Summary of the number of events before and after event and track selection.

Period	**Trigger name**	**No. of events before event and track selection**	**No. of events after event and track selection**
LHC12h	CINT7-S-NOPF-ALLNOTRD	21 333 315	20 083 045
	CMSH7-S-NOPF	11 697 343	11 257 084
LHC12i	CINT7-S-NOPF-ALLNOTRD	2 453 904	2 307 298
	CMSH7-S-NOPF	1 698 708	1 637 144
TOTAL	**CINT7-S-NOPF-ALLNOTRD**	**23 032 023**	**22 390 343**
	CMSH7-S-NOPF	**13 396 051**	**12 894 228**

The multiplicity determination is implemented as follows in the analysis task;

```
// count the tracklet multiplicity
//********************************
Int_t multiplicity = 0;

AliAODTracklets *tracklets = fAOD->GetTracklets();

Int_t nTracklets = tracklets->GetNumberOfTracklets();
for (Int_t nn = 0; nn < nTracklets; nn++)
```

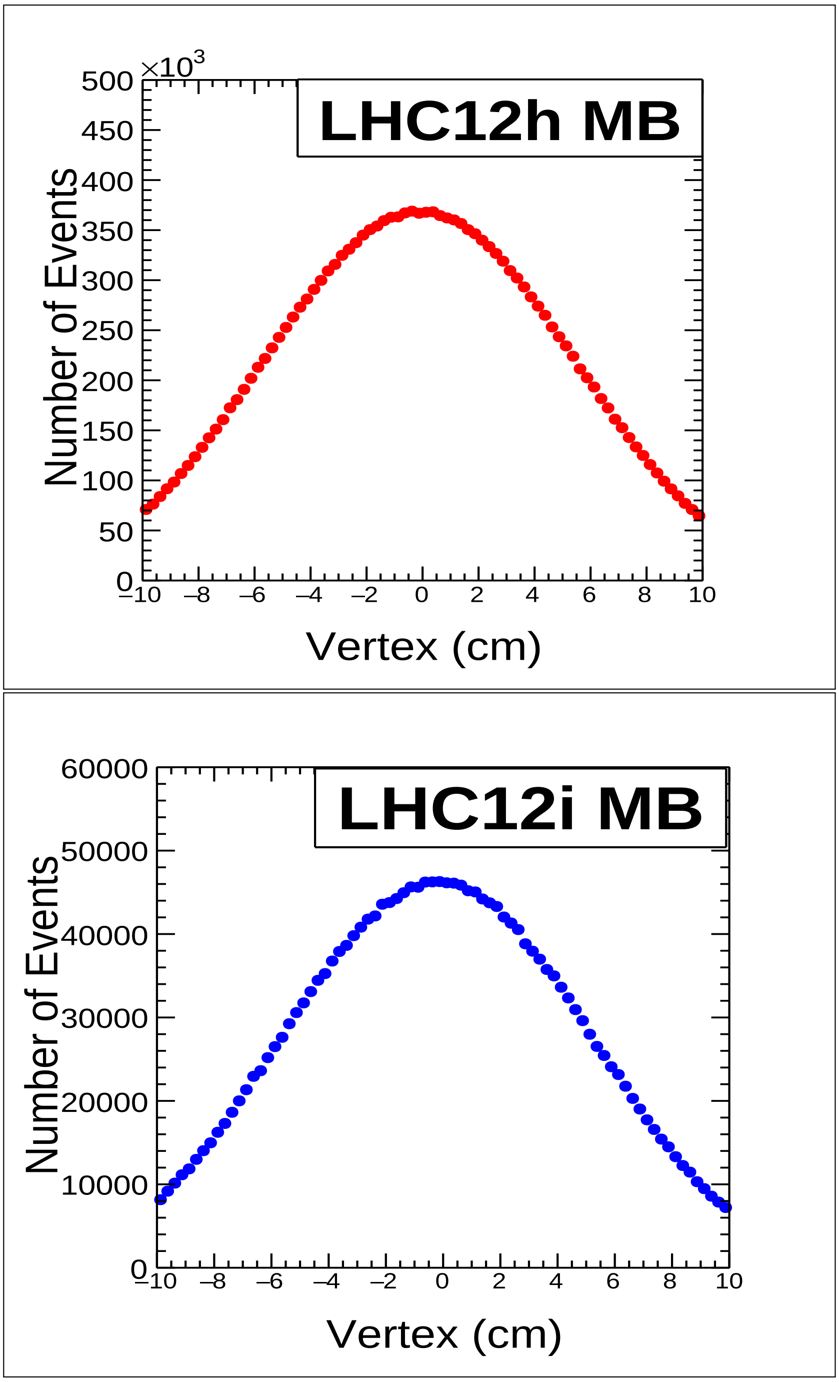

Figure 4.1: The distribution of events as a function of the vertex position for MB triggered events in the periods of interest

```
 {
// consider only tracklets in the good eta range
Double_t theta = tracklets->GetTheta(nn);
Double_t eta = -TMath::Log(TMath::Tan(theta/2.0));
if ( TMath::Abs(eta) > 1.0) continue; // Eta Cut implemented here
 multiplicity += 1;
} // end tracklets loop
if ( multiplicity < 1 ) return; // skip event with 0 tracklets
```

The multiplicity (number of tracklets) is plotted as a function of the vertex position as shown in Figure 4.3. This is done in order to evaluate the variation of the SPD efficiency per given data taking period. On the right-hand side of the 2D plots in Figure 4.3 is the intensity scale which represents the concentration of the events per vertex position - red signifies high concentration of events. For both periods LHC12h and LHC12i, most MB events are in the region -4 $<$ $\mathrm{Z_{vtx}}$ $<$ 7 cm, shown by the red colour. From Figure 4.3 we then compute the average number of tracklets as a function of the vertex position - so called tracklet profile, shown in Figure 4.4. Since the number of tracklets produced per event is independent of the vertex position, the shapes of the tracklet profiles are expected to be constant (flat profile) across the vertex positions. However, as observed in Figure 4.4, the tracklet profiles have a structure which shows a ”non-flat” trend, implying that the SPD efficiency varies with the vertex position. The average number of tracklets increases with the vertex position in the region -10 $<$ $\mathrm{Z_{vtx}}$ $<$ 7 cm and decreases thereafter. This is due to the fact that during data taking in 2012 the performance of the SPD was compromised due to problems in the cooling system. The measured multiplicity distributions must be corrected for the SPD efficiency.

Figure 4.5 shows the multiplicity plotted as a function of the vertex for CMSH events. The average number of tracklets per vertex position is computed in the same way as done for MB events. The obtained tracklet profiles are shown in Figure 4.6. This is done in order to ascertain whether the same trend observed in Figure 4.4 for MB events is also seen for CMSH events and if a correction is also needed for CMSH triggered events. A similar variation with the vertex position as seen for MB events is also observed here. The average number of tracklets increases with the vertex position at -10 $<$ $\mathrm{Z_{vtx}}$ $<$ 6 cm and decreases outside this region. Therefore, the same correction procedure must be applied to both MB and CMSH events.

4.2.1 Multiplicity correction

Since the SPD efficiency is varying with the vertex position, a correction must be implemented in order to ensure the same efficiency at each vertex position. As discussed early in this chapter, two different periods were considered in this study. The runlist for period LHC12h and LHC12i consist of MB events (CINT7-S-NOPF-ALLNOTRD) and high-p_{T} single muon triggered events (CMSH7-S-NOPF-ALLNOTRD). For the correction we consider the period with the highest average number of tracklets and use this value as a reference, $<\mathrm{N_{ref}}>$, in the correction formula in, equation 4.1. In Figure 4.4 we compare tracklet profiles of LHC12h and LHC12i, for MB events. Accordingly, period LHC12h has the highest average number of tracklets per vertex position compared to LHC12i. For this reason the reference, $<\mathrm{N_{ref}}>$ is taken from LHC12h, as shown in Figure 4.4. The value of $<\mathrm{N_{ref}}>$ = 11.3 at $\mathrm{Z_{vtx}}$ = 6.52 cm. This value is used in the correction formular given in equation 4.1.

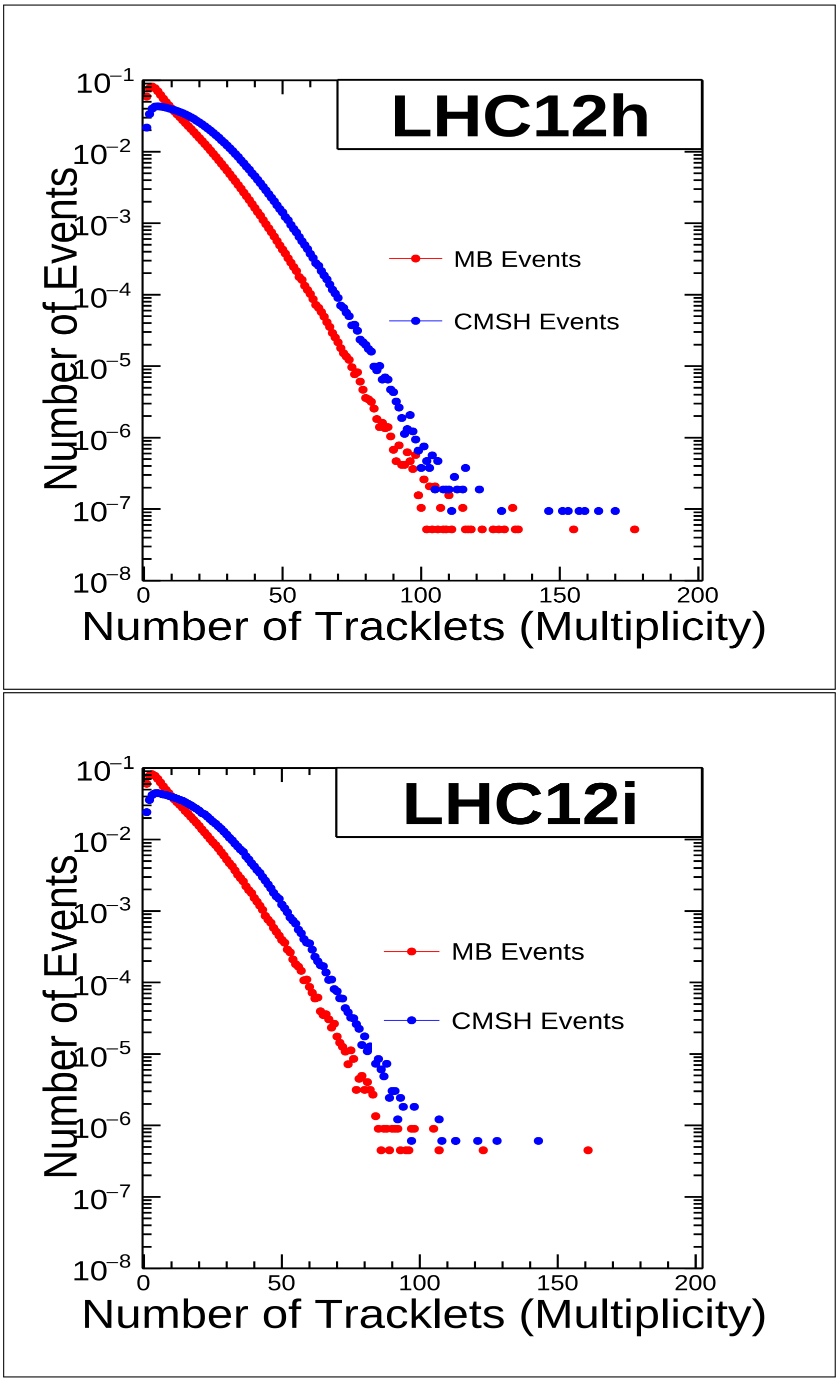

Figure 4.2: The raw multiplicity distributions normalised to unity

$$N^{\mathrm{corr}} = \frac{< N_{\mathrm{ref}} >}{< N_{\mathrm{period}}(z) >} N_{\mathrm{raw}} \tag{4.1}$$

N^{corr} is the corrected number of tracklets (corrected multiplicity distribution), $<N_{\mathrm{ref}}>$ is the reference average number of tracklets, $<N_{\mathrm{period}}(z)>$ is the average number of tracklets for events at vertex position z and N_{raw} is the measured raw number of tracklets (raw multiplicity distribution). The correction is implemented as follows in the analysis task;

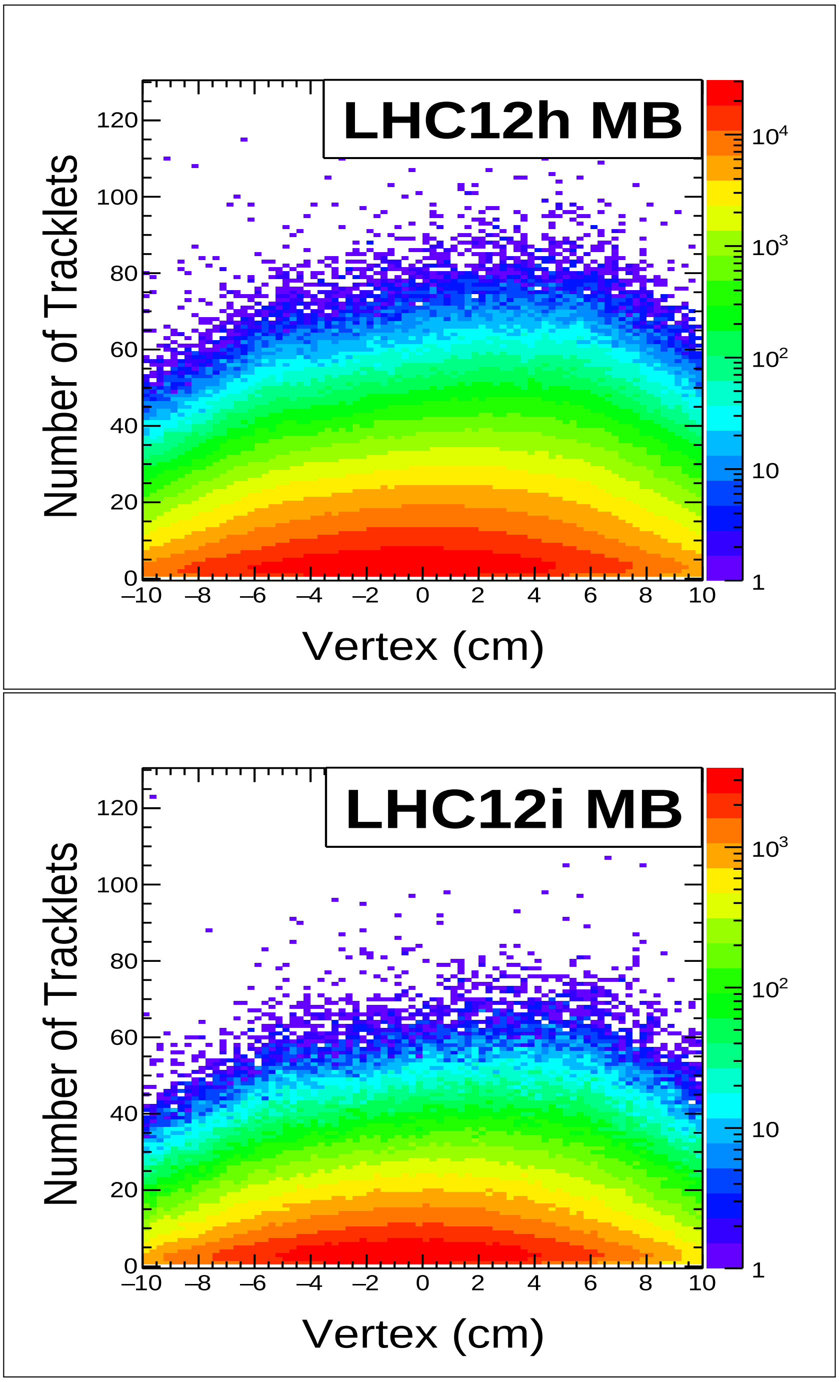

Figure 4.3: The raw number of tracklets as a function of vertex for MB events. The colours represent the concentration of events as shown in the scale on the right-hand side of each figure where red represents high number of events.

```
// correction for the SPD acceptance
double corrfactor = 1.;
if( hmultprofile) corrfactor =
hmultprofile->GetMaximum()/hmultprofile->
GetBinContent(hmultprofile->FindBin(vz->GetZ()));
cout << "Nref = " << hmultprofile->GetMaximum() << endl;
double deltaN = (corrfactor * multiplicity) - multiplicity;
```

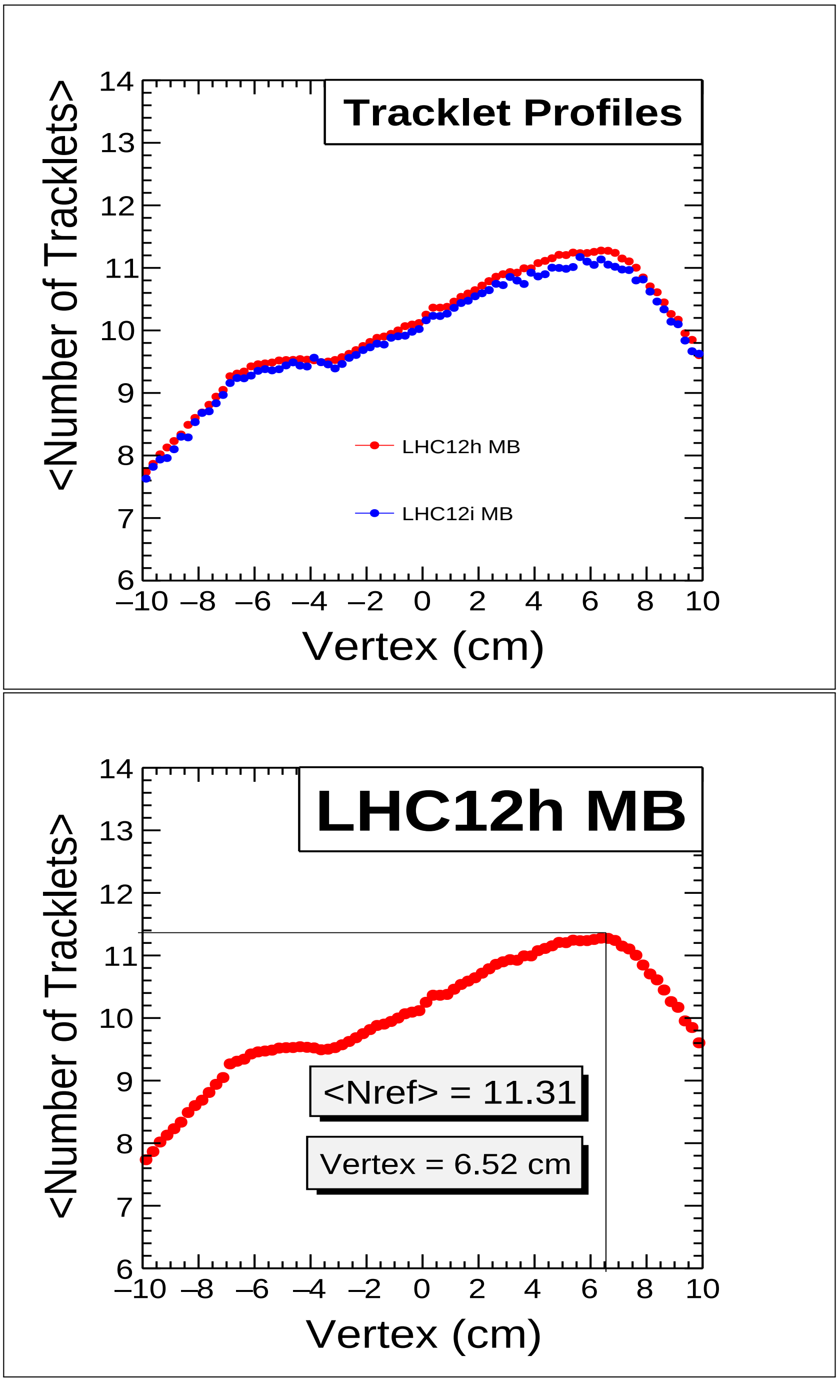

Figure 4.4: Comparison of the tracklet profiles for period LHC12h and LHC12i for the MB triggered events is shown on the top figure. The figure below shows the value of the <N_{ref}> and its vertex position.

```
int missingtracklets = Nrand->PoissonD(TMath::Abs(deltaN));
int corrmult = multiplicity + missingtracklets; //corrected ntracklets
// fill the multiplicity vs vertex histogram
fNtracklets->Fill(vz->GetZ(),corrmult);
```

The corrected number of tracklets is plotted again as a function of the vertex position as shown in Figure 4.7. The results do not exhibit a flat trend across the vertex

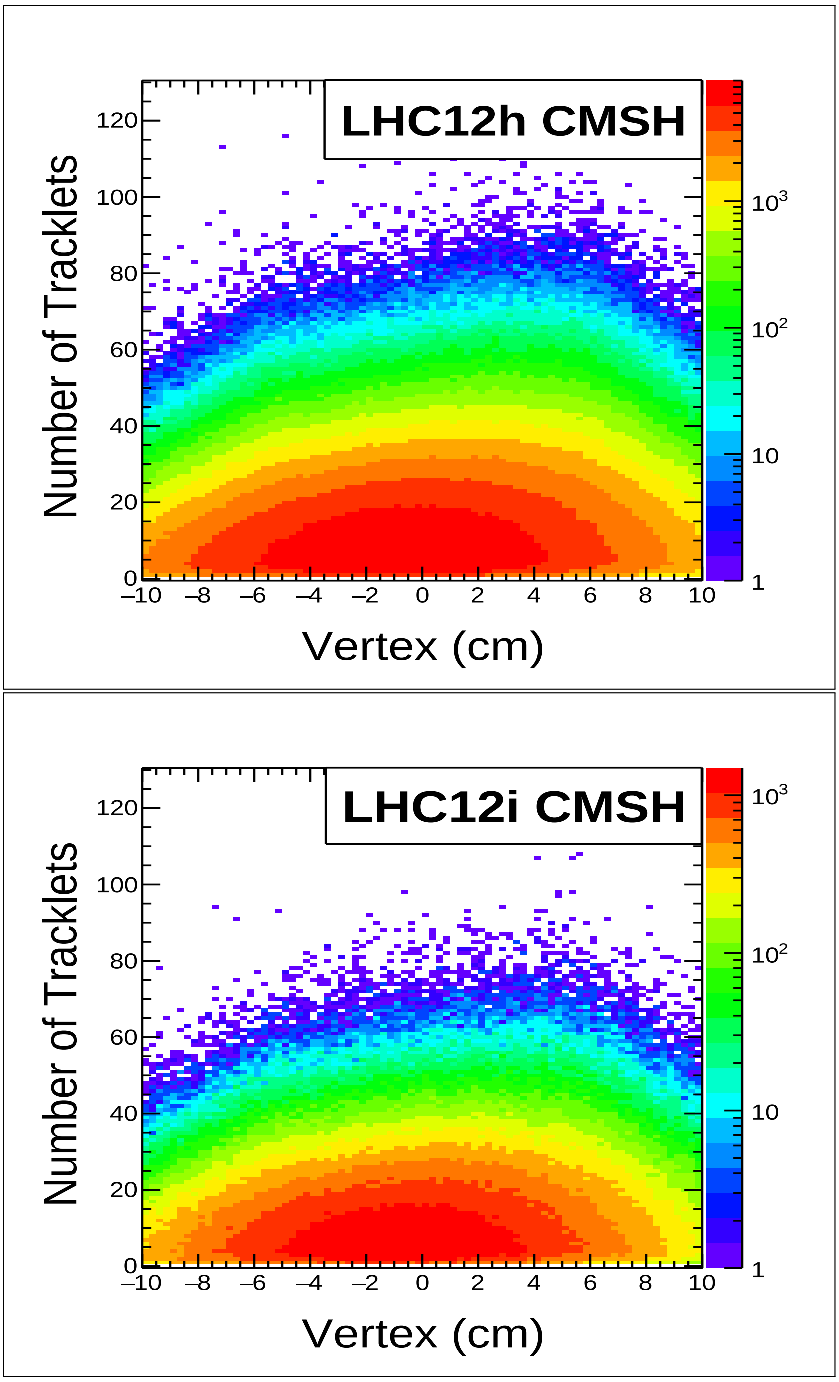

Figure 4.5: Raw number of tracklets as a function of vertex for CMSH events. The colours represent the concentration of events as shown in the scale on the right-hand side of each figure where red represents high number of events.

positions, in particular at $2 < Z_{\mathrm{vtx}} < 8$ cm where a bump is observed. Ideally, the corrected tracklet profile should be flat across the vertex position since the correction is aimed at making the efficiency of the SPD to be equal at all positions in the region $|Z_{\mathrm{SPD}}| < 10$ cm. The following is a discussion of the improvements implemented on the multiplicity measurement in order to obtain a flatter tracklet profile after the correction.

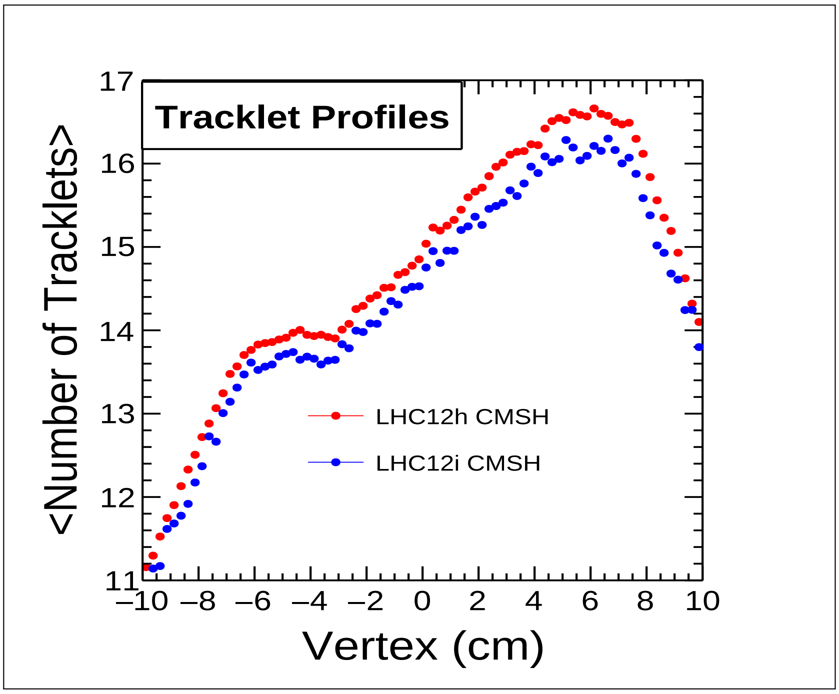

Figure 4.6: The comparison of the tracklet profiles for LHC12h and LHC12i for the CMSH triggered events.

4.3 Improvements on the correction method

To improve the correction of the measured charged-particle multiplicity discussed in section 4.2, we investigate the changes of the SPD configuration per run for both period LHC12h and LHC12i. This accounts for the variation of the SPD efficiency per run during data taking. Figure 4.8 shows the number of active modules in the outer and inner layers of the SPD as a function of the run numbers. Overall, the total number of active modules for the inner and outer layer of the SPD is 80 and 160, respectively. Of those, about 8 and 10 were missing for the outer and inner layers respectively, during these specific data taking periods. Also, the number of active modules in the inner layer of SPD is the same for all the runs while it is not the case with the outer layer. The runs with the same SPD configuration are then grouped in sub-periods and analysed seperately to ensure that the acceptance and hence the efficiency of the SPD is the same. Table 4.5 shows the final four sub-periods used to build the data sample in this case. The measurement of the multiplicity is done considering only the minimum bias trigger as it gives an accurate account of the events and all the charged particles in the events because it includes the SPD.

The event selection cuts discussed in section 4.1.2 are applied and the average number of tracklets extracted as a function of the vertex position (tracklet profiles) from each sub-period are shown in Figure 4.9.

The variation of the SPD vertex position with the mean number of tracklets is similar to the one observed in section 4.2. For all the sub-periods, the average number of tracklets is minimum at Z_{SPD} = -10 cm, however, the position of the highest average number of tracklets varies between 6.2 cm and 6.8 cm for each subperiod. Table 4.6 shows the minimum and maximum number of tracklets for each subperiod and the relative difference (as a percentage). The spread of the 5 minima and the 5 maxima is very small (i.e. 0.85 and 0.56, respectively).

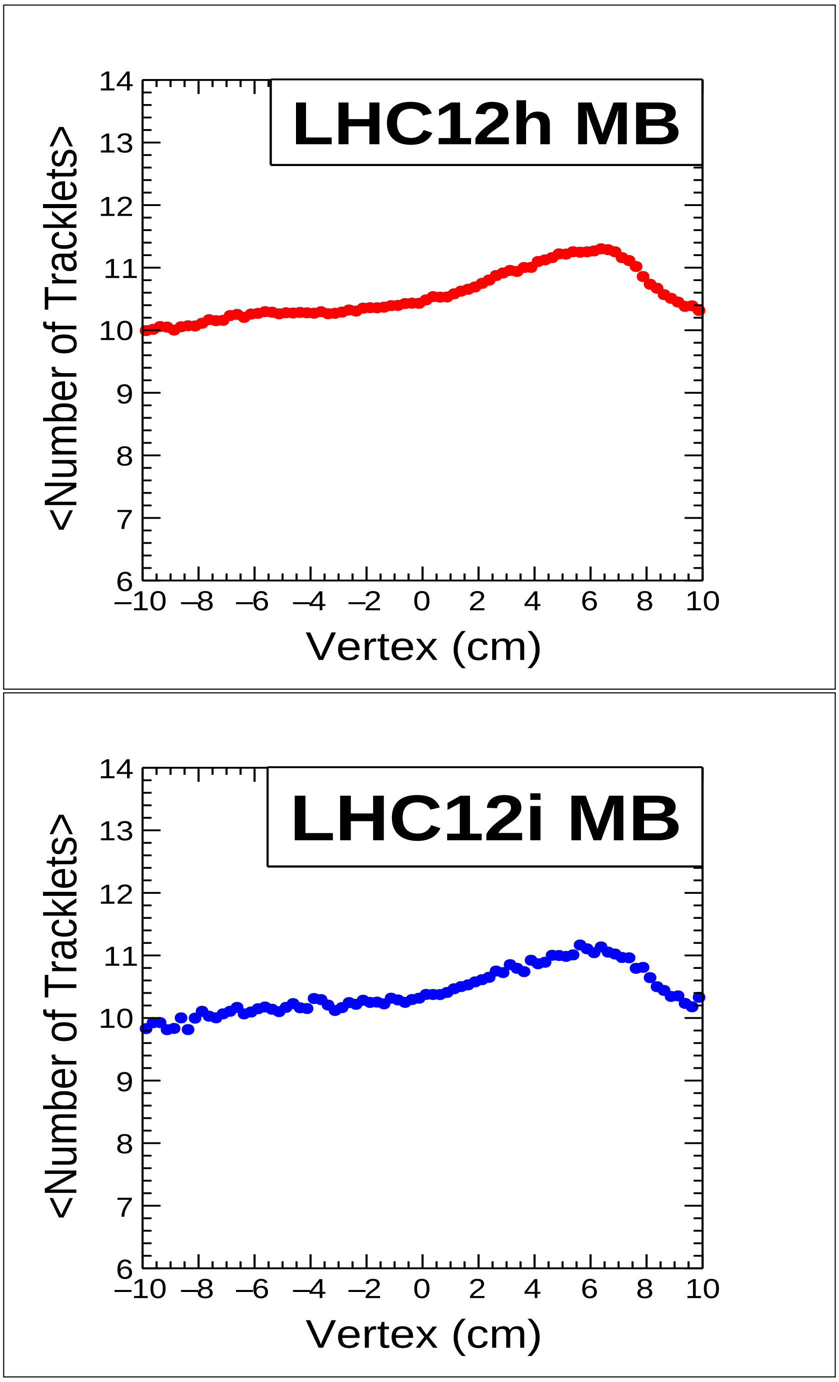

Figure 4.7: Corrected Tracklet profiles for MB Events

The correction described in Section 4.2.1 gives the same value for all events reconstructed with the same number of tracklets at a given vertex position. This results in a non-flat distribution observed in the corrected tracklet profiles shown in Figure 4.7. To obtain a flat distribution, the correction is done by choosing the maximum average number of tracklets as a reference (<N_{ref}>) and taking the difference between the corrected number of tracklets computed using equation 4.1 and the raw multiplicity distribution, ΔN;

$$\Delta N = N_{\mathrm{raw}} \frac{< N_{\mathrm{ref}} > - < N_{\mathrm{period}}(z) >}{< N_{\mathrm{period}}(z) >} \tag{4.2}$$

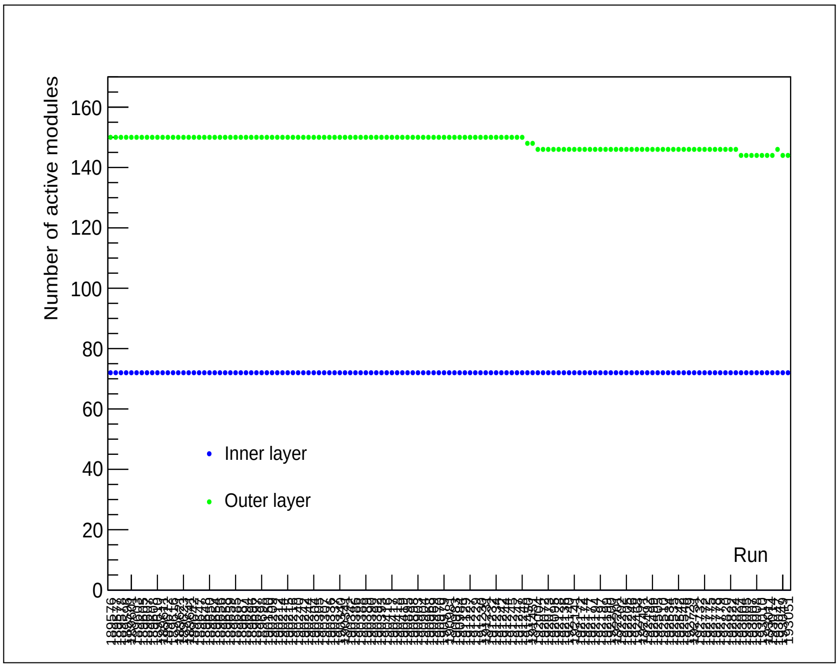

Figure 4.8: SPD active modules as a function of the run numbers

Table 4.5: Sub-periods obtained from the number of active modules in the outer layer of the SPD in pp runs considered in LHC12h and LHC12i periods

Number of active modules	**LHC12h runs**	**LHC12i runs**
144	-	11
146	32	7
148	2	-
150	80	-

then we generate the correction ($\Delta\mathrm{N}_{\mathrm{rand}}$) randomly with a Poissonian distribution centered at $\Delta\mathrm{N}$. Therefore, the correction is given by:

$$N^{\mathrm{corr}} = N_{\mathrm{period}}(z) + \Delta N_{\mathrm{rand}} \tag{4.3}$$

$\Delta\mathrm{N}_{\mathrm{rand}}$ is positive when the average number of tracklets is less than the reference value. This allows the number of tracklets to be added in order to produce a flat multiplicity distribution along the SPD vertex position. The corrected tracklet profiles, resulting from the use of equation 4.3, for each sub-period are shown in Figure 4.10. The difference between the maximum and the minimum average number of tracklets after the correction is given in Table 4.7 and will be used as systematic uncertainty.

Since there is no major difference between periods LHC12h and LHC12i, the results

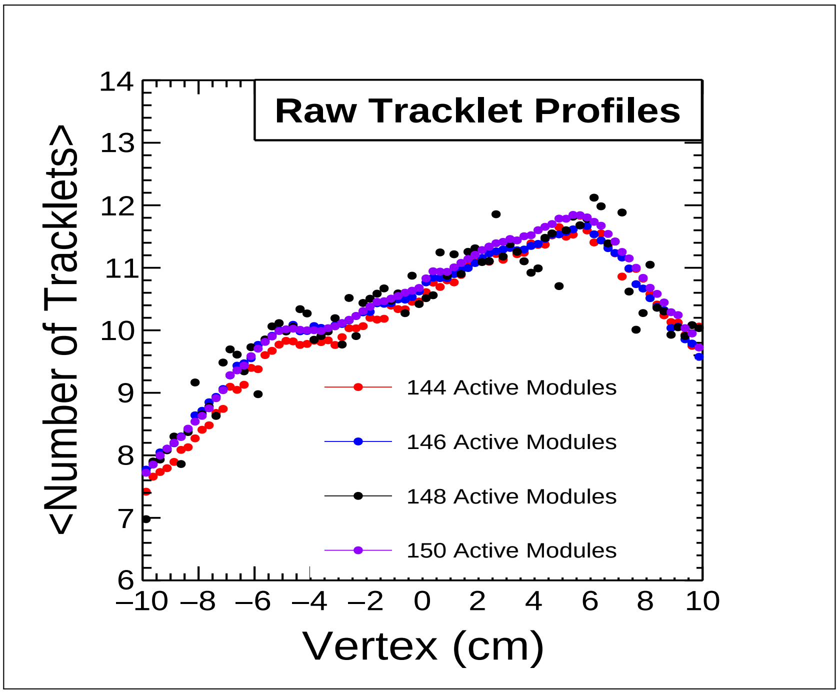

Figure 4.9: The raw tracklet profiles for the 5 subperiods.

Table 4.6: Minimum and maximum average number of tracklets per sub-period

Number of active modules	**<Ntracklets>$_{\text{min}}$**	**<Ntracklets>$_{\text{max}}$**	**% difference**
144	7.42	11.83	37.3
146	7.76	11.67	33.5
148	6.98	12.12	42,4
150	7.72	11.85	33.1

obtained from the correction can be merged. The corrected tracklet profile with merged statistics is shown in Figure 4.11. The corrected tracklet profile is perfectly flat, the difference between the maximum (11.93) and the minimum (11.81) $<N_{\text{period}}(z)>$ is 0.12 ($\simeq$ 1%) .

The corrected multiplicity distributions in Figure 4.12 show a shift towards higher multiplicity. This could be attributed to the choice of the reference value i.e. maximum as opposed to minimum value of $<N_{\text{ref}}>$. For the next step, the corrected multiplicity distribution is divided into bins containing approximately the same number of events

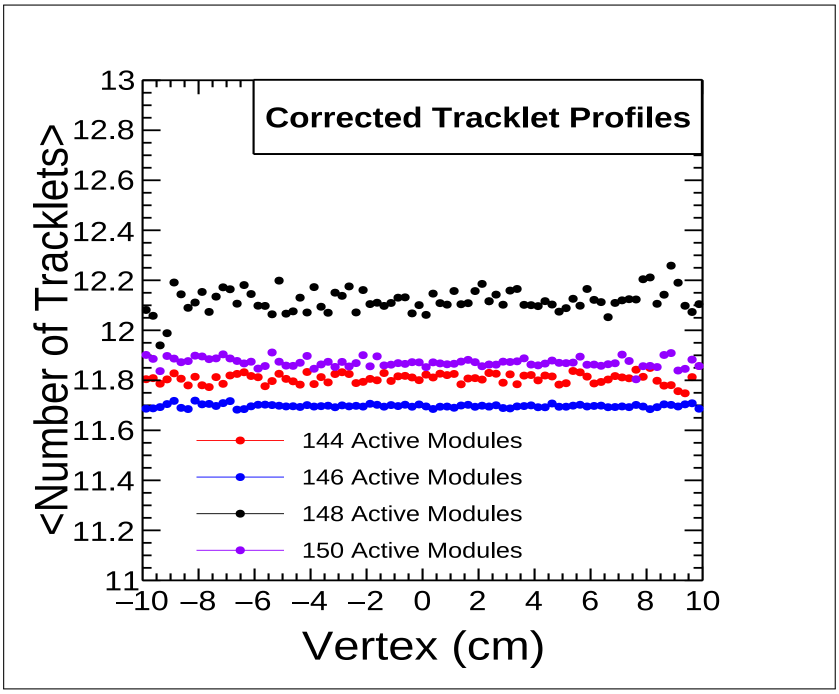

Figure 4.10: Corrected tracklet profiles for the 5 sub-periods

Table 4.7: Minimum and maximum average number of tracklets per sub-period after the correction using equation 4.3

Number of active modules	**<Ntracklets>$_{\mathbf{min}}$**	**<Ntracklets>$_{\mathbf{max}}$**	**% difference**
144	11.75	11.85	0.9
146	11.66	11.70	0.3
148	11.93	12.25	2.6
150	11.86	12.05	1.5

as shown in Table 4.8.

It must be noted that the corrected multiplicity is not the actual produced multipicity since we still need to correct for the detector efficiency to account and/or ensure that no charged particles are missed. The produced charged-particle multiplicity can be represented as follows;

$$N^{produced}_{tracklets} = \alpha \cdot N^{corrected}_{tracklets} \tag{4.4}$$

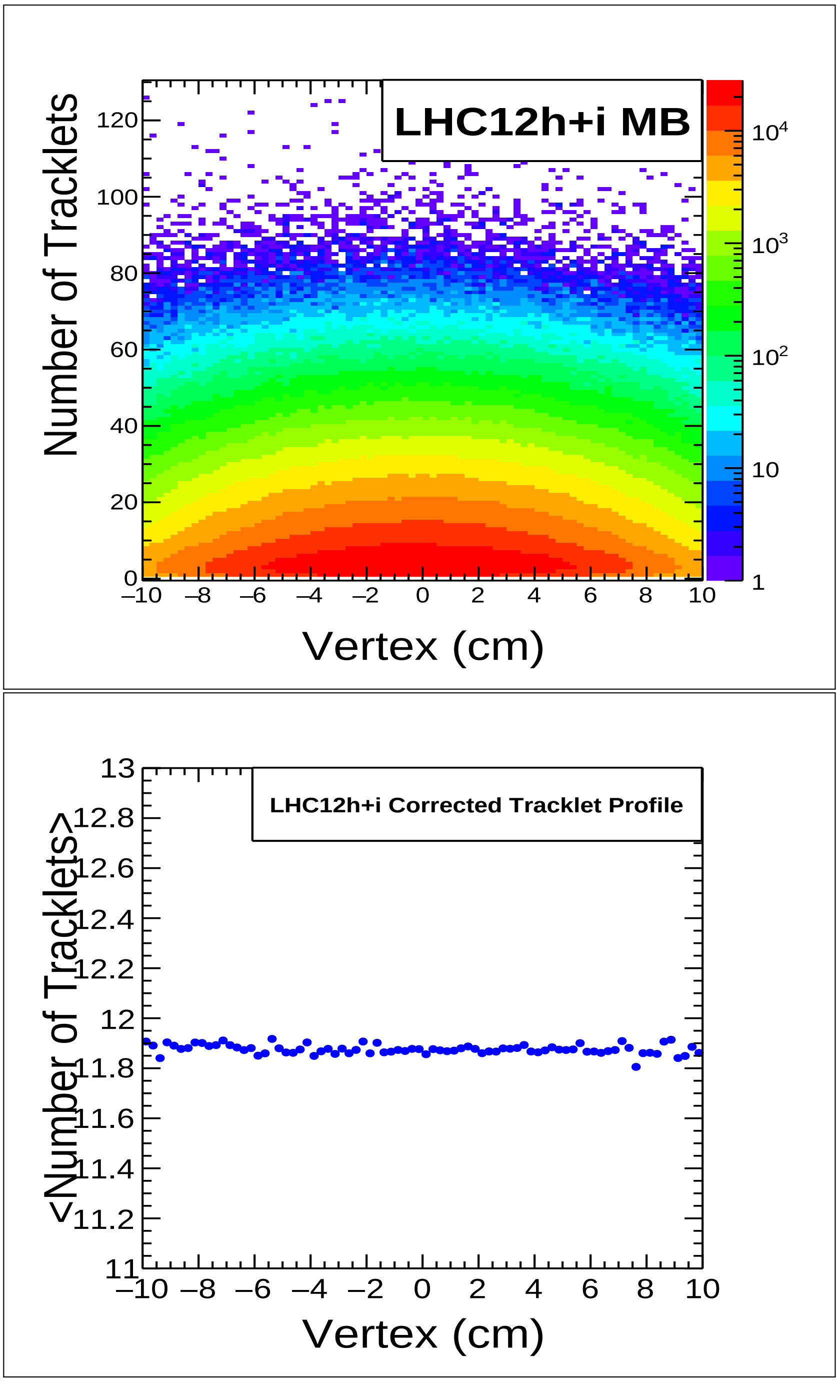

Figure 4.11: Top figure : The multiplicity (number of tracklets) plotted as a function of the vertex position. Bottom figure : The average number of tracklets <Ntracklets> as a function of the vertex position for LHC12h+i MB events

where α is the missing normalisation factor that can be obtained from Monte Carlo simulation (see [MPC01]) and is representative of the SPD efficiency. We therefore consider the relative multiplicity in order to eliminate α assuming that it is independent of the multiplicity. Therefore the relative multiplicity at each bin is computed as;

$$rel.\ N_{tracklets} = \frac{< N^{i}_{tracklets} >}{< N^{tot}_{tracklets} >} \tag{4.5}$$

The number of MB events per given multiplicity bin are given in Table 4.8. The results of the computed relative multiplicity are presented in the next chapter. The following discussion is about the extraction of the single muons.

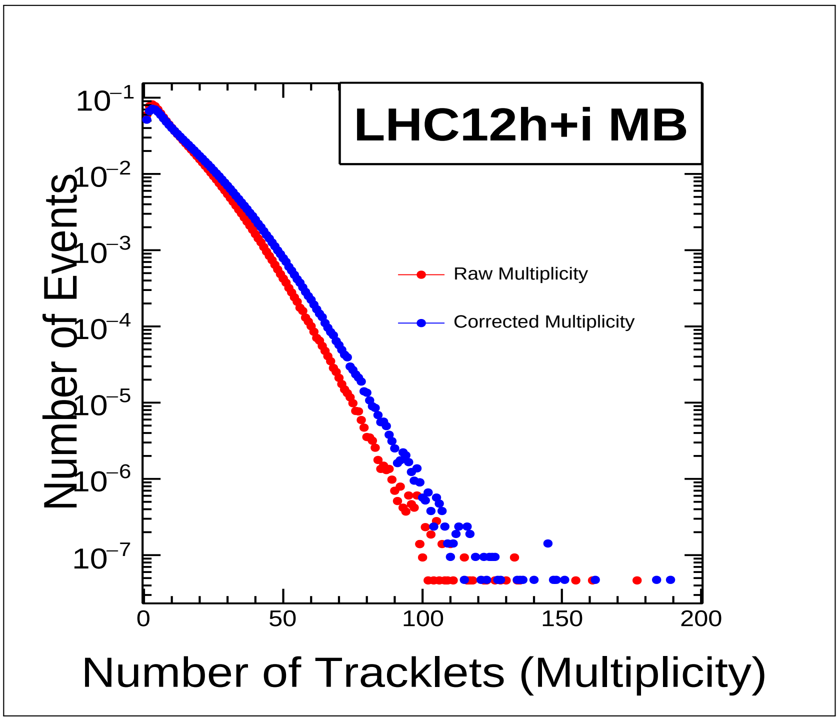

Figure 4.12: Corrected multiplicity distribution (blue) superimposed with the raw distribution (red) normalised to unity.

4.4 Single muon measurements

Muons are measured in the Muon Spectrometer located at forward rapidity in ALICE. As mentioned earlier, the single muon high-p_T trigger CMSH7-S-NOPF-ALLNOTRD is used to select muons of interest in this study. Track cuts are used to reduce various kinds of background in the measurement of muons in the Muon Spectrometer. The following cuts are applied.

- **Geometrical cuts**
  This cut takes into account the acceptance of the Muon Spectrometer which includes the pseudorapidity (η) as well as the exit polar angle with respect to the front absorber, θ_{abs}. Therefore in the analysis all the tracks are reconstructed in the pseudorapidity region -4 < η < -2.5. The cut eliminates all muon tracks outside the spectrometer. The exit polar angle of the muon track at the end of the absorber ($2^{\circ} < \theta_{\text{abs}} < 10^{\circ}$) removes muons emerging at small angles that have crossed the thick beam shield and consequently suffered multiple scattering in the absorber.

Table 4.8: Number of events per given multiplicity bins for MB events

Multiplicity bins	**Number of MB events**
[1,2]	2 493 232
[3,4]	2 988 796
[5,6]	2 630 851
[7,9]	3 077 181
[10,13]	2 977 363
[14,18]	2 559 812
[19,27]	2 585 736
[28,300]	1 790 414
[1,300]	21 103 385

- **Trigger matching**
  This cut requires that each muon track reconstructed in the muon tracking chambers should match the corresponding track in the trigger chambers with a certain p_{T} threshold. All muon tracks considered should have $p_{\mathrm{T}} \gtrsim 4.2$ GeV/c. This reduces hadronic background absorbed in the iron wall.

- **Correlation of the momentum and the distance of closest approach**
  The distance of closest approach (DCA), is the distance between the interaction vertex and the extrapolated muon track in the plane containing the vertex and perpendicular to the beam direction. Owing to the multiple scattering in the front absorber, the DCA distribution of tracks coming from the interaction vertex can be described by a Gaussian function, whose width depends on the absorber material and is proportional to $\frac{1}{p}$, where p is the muon momentum. The beam-induced background[2] does not follow this trend, hence it can be rejected by applying a cut on the product p x DCA, at 5 or 6 times the standard deviation of the Gaussian distribution depending on run conditions of the period being analysed.

---

[2] Particles produced due to interactions in the beam pipe near the IP

The single muon p_{T} distribution, shown in Figure 4.13, gives information on the momentum and number of single muons. The following is implemented in the analysis task to extract the single muon p_{T} distribution;

```
bool aretheregoodmuons = kFALSE;
for ( Int_t iTracks = 0; iTracks < fAOD->GetNumberOfTracks();
 iTracks++ ) {
AliAODTrack* track = dynamic_cast<AliAODTrack*>
 (fAOD->GetTrack(iTracks));
if (!track) {
printf("ERROR: Could not receive track %d\n", iTracks);
continue;
}
 if (!fMuonTrackCuts->IsSelected(track)) continue;
data[kPt]         = track->Pt();
aretheregoodmuons = kTRUE;
 // fill for _each_ muon
//*******************
fHn->Fill(data);
}// end loop on AOD tracks
```

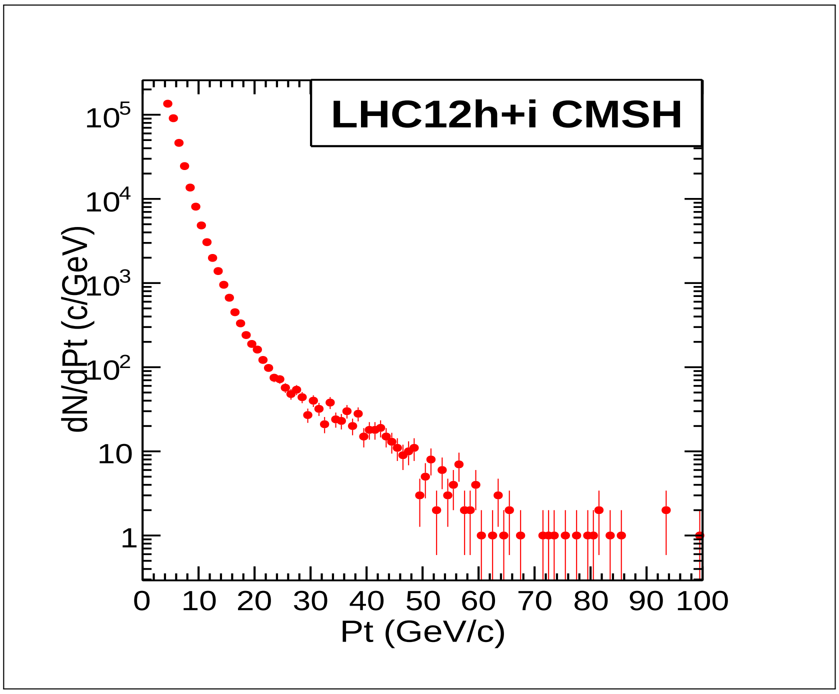

Figure 4.13: The high-p_{T} single muon distribution for periods LHC12h+i.

Using the multiplicity bins discussed in section 4.2.1, we extract the number of single muons from heavy flavour (c and b hadrons) decay from the inclusive single muon

p_{T} distribution shown in Figure 4.13. The inclusive single muon p_{T} distribution consists of hadronic muons (muons from the decay of π and K), heavy flavour muons (muons from c and b decay) and those from $W^{\pm}$ and Z bosons. All these components dominate different regions of the inclusive p_{T} spectra [ALI05b]; hadronic muons dominate at $p_{\mathrm{T}} < 6$ GeV/c, heavy flavour muons are dominant in the intermediate region $6 < p_{\mathrm{T}} < 20$ GeV/c while W and Z bosons dominate the high p_{T} region above 30 GeV/c. Thus, the signal, i.e. the number of single muons from heavy flavours, is extracted in the region $6 < p_{\mathrm{T}} < 20$ GeV/c. The number of muons at each multiplicity bin interval is shown in Table 4.9. Therefore, the total number of single muons in the p_{T} region $6 < p_{\mathrm{T}} < 20$ GeV/c is 106 868 and these can be inferred as heavy flavour muons.

Table 4.9: Number of events and muons with $6 < p_{\mathrm{T}} < 20$ GeV/c per given multiplicity bin for LHC12h+i CMSH events

Multiplicity bins	**Number of CMSH events**	**Number of muons ($6 < p_{\mathrm{T}} < 20$ GeV/c)**
[1,2]	579 891	488
[3,4]	868 698	2501
[5,6]	926 767	3 323
[7,9]	1 355 621	7 018
[10,13]	1 685 912	11 962
[14,18]	1 854 821	16 863
[19,27]	2 448 024	27 971
[28,300]	2 439 937	36 742
[1,300]	12 159 671	106 868

The measured number of muons depends on the performance of the detector during data taking period. The performance of the detector is influenced by its acceptance and efficiency (A x ϵ). This includes the tracking and trigger efficiency as well as the alignment due to variations of positions of detector elements (see Chapter 3, section 3.2.5.8). Therefore it is necessary to correct the measured number of muons for acceptance and efficiency (A x ϵ). The correction factor for A x ϵ is obtained by performing

Monte Carlo simulations.

The complete structure of the analysis task, AliAnalysisTaskPtCMSH.cxx is shown in Appedix A.2.

4.4.1 Monte Carlo simulations

The main aim is to evaluate the Acceptance x efficiency (A x ϵ) of the Muon spectrometer which takes into account the position of the trigger and tracking chambers with respect to the entire ALICE detector. For this purpose we need the get the shape of the p_{T} and η differential cross sections by simulating the production cross section of heavy flavour (c and b hadrons) in pp collisions at 8 TeV using the Fixed Order Next to Leading Logarithms[3] (FONLL) [CGN98] code in AliRoot. The differential cross section calculation was done using CTEQ6.6 Parton Distribution Functions (PDFs) [CTEQ]. As the aim of the simulation was to produce a differential cross section signal for heavy flavours in pp collision, therefore, the following processes were considered in the simulation using FONLL, which is accessible via web [CGN97];

$$p + p \to c + X$$

$$p + p \to b + X$$

and their subsequent decays into single muons through the following processes;

$$c \to 70\% D^0 + 30\% D^+ \to \mu + X$$

$$b \to \mu + X$$

$$b \to D \to \mu + X$$

The p_{T} and η differential cross sections extracted in the simulation are plotted in Figure 4.14 where black points represent the sum of all contributing processes. The sum of the cross sections was then fitted with the function given in equation 4.6 for the p_{T} and equation 4.7 for the η. These functions are chosen because they give a good fit for the sum, particularly in the p_{T} and η range of interest. Figure 4.15 shows the sum of all the contributions (in blue) and the fit function (in green). The p_{T} fit function describes the FONLL cross section calculation well in the range $0 < p_{\mathrm{T}} < 20$ GeV/c where muons from c and b dominate while the η fit function also describes the FONLL calculation well in the range -4 < η < -2.5 which is the geometrical acceptance of the Muon spectrometer.

$$p0\left(10^{x(p1\times(1-10^{(xp2)})+p3)} \times \frac{1}{x^{p4}} \times (p5 + xP6 + x^2p7)\right) \tag{4.6}$$

$$p0 + xp1 + x^2p2 + x^4p3 + x^6p4 + x^8p5 \tag{4.7}$$

---

[3] Code for calculating the differential heavy quark production cross section in pp collisions.

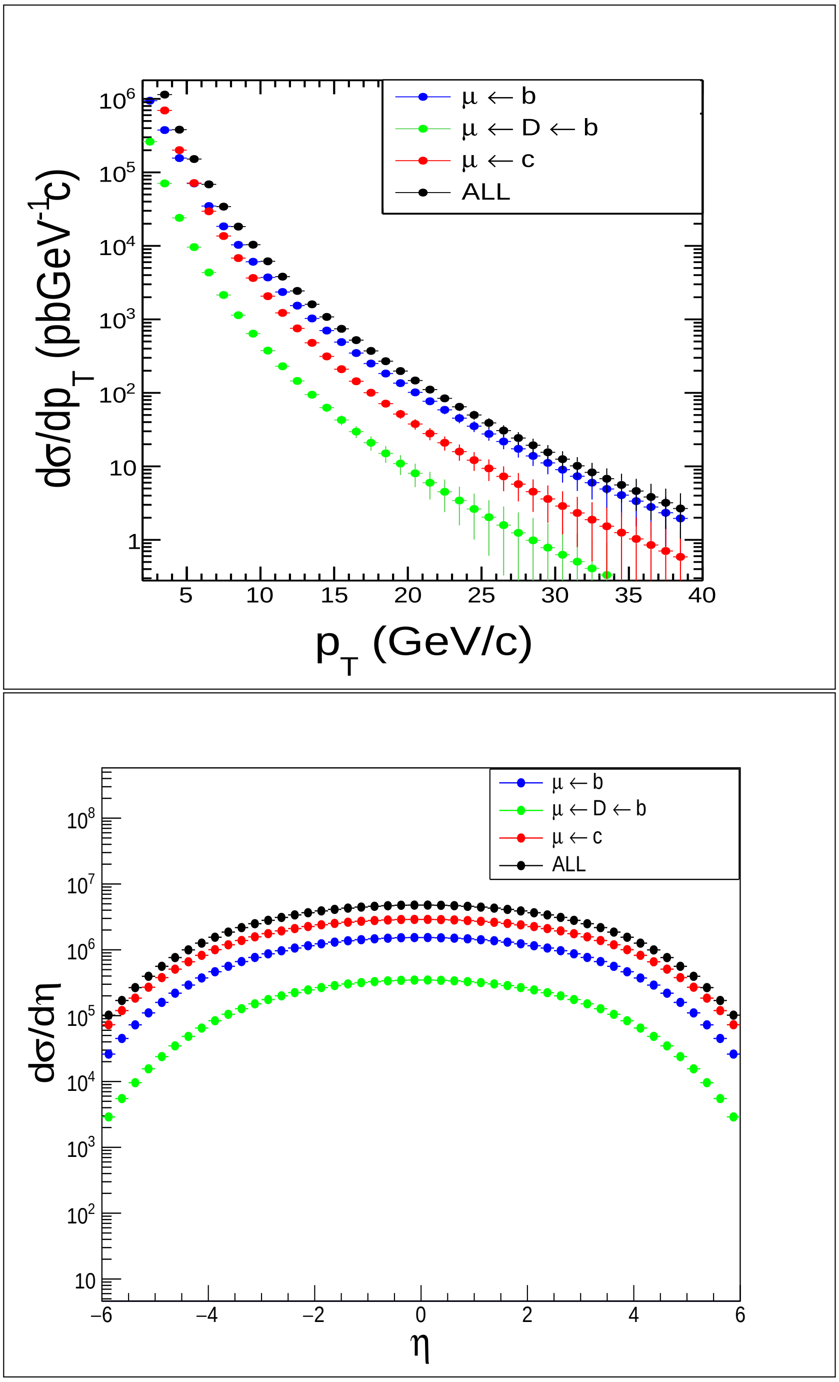

Figure 4.14: Differential production cross-sections for heavy flavour (c and b quarks) muons as a function of p_T (top figure) and η (bottom figure) for p-p collisions at 8 TeV obtained from FONLL [CGN98] event generator.

The parameters p0 to p7 (equation 4.6) as well as p0 to p5 (equation 4.7) are then used as input in MC to reproduce the p_T and η distributions which represents as ideally (100%) efficient Muon Spectrometer. This is done using a simulation macro sim.C in AliRoot. Here we obtain what is called the generated p_T and η spectra.

```
simulator.SetDefaultStorage(VAR_OCDB_PATH);
 if ( VAR_OCDB_SNAPSHOT ){
simulator.SetCDBSnapshotMode("OCDB_sim.root");
```

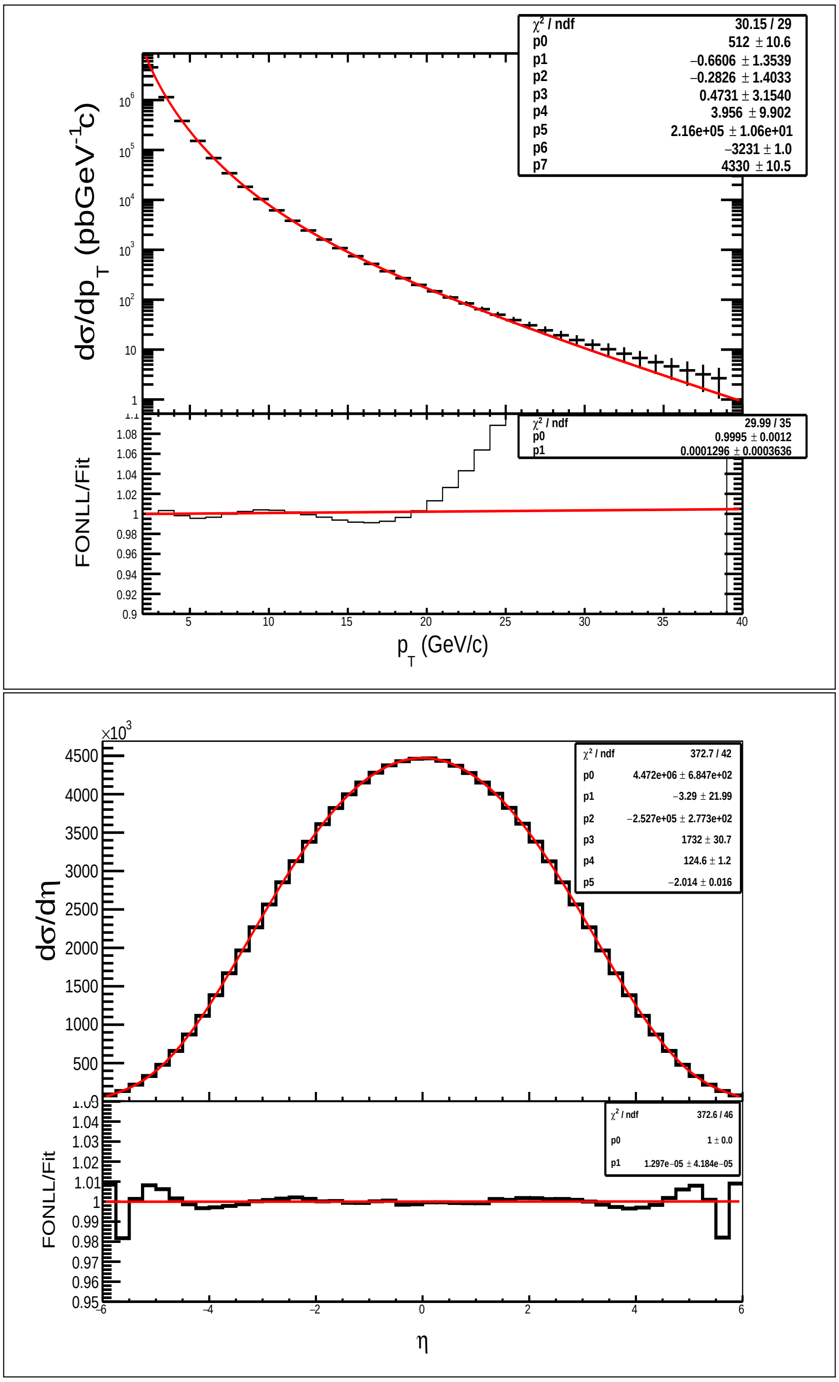

Figure 4.15: The sum of the differential p_{T} and η distributions (in black) with the fit functions (in red). Top figure shows the sum of all differential cross sections fitted with the function given in equation 4.7 for the η distribution and 4.6 for the p_{T} distribution. Bottom figures shows the ratio of the sum (in black) of the differential cross sections to the fit function.

```
 }  if ( ! VAR_PURELY_LOCAL ) { simulator.SetSpecificStorage
("MUON/Align/Data",VAR_SIM_ALIGNDATA); simulator.UseMagFieldFromGRP();
if ( VAR_USE_ITS_RECO ){simulator.SetSpecificStorage
 ("ITS/Align/Data", "alien://Folder=/alice/simulation/2008/v4-15-
 Release/Ideal"); simulator.UseVertexFromCDB(); }}
```

The complete sim.C macro is given in Appendix A.7. To take into account the tracking and trigger efficiencies, we utilise realistic detector configuration (calibration runs) during LHC12h and LHC12i data taking periods. The calibration database are stored in the Offline Calibration Data Base (OCDB) accessible via AliRoot [OCDB]. A reconstruction macro, rec.C, given in Appendix A.8, is used to retrieve this calibration information and to reproduce the shape of the reconstructed p_{T} distribution. This is done as follows in the rec.C macro;

```
reco.SetDefaultStorage("raw://");
reco.SetCDBSnapshotMode(Form("alien:///alice/data/2012/LHC12i/%09d/
ESDs/muon_calo_pass2/OCDB.root",run));

AliCDBManager* man = AliCDBManager::Instance();
man->SetDefaultStorage("alien://folder=/alice/data/2012/OCDB");
man->SetSpecificStorage("GRP/GRP/Data",Form("local://%s",
gSystem->pwd()));
man->SetSpecificStorage("MUON/Align/Data","alien://folder=/alice
/simulation/2008/v4-15-Release/Residual");
man->SetSpecificStorage("MUON/Calib/RecoParam","alien://folder=/ali
ce/data/2012/OCDB",5,0);
```

The resulting generated (ideal detector) and reconstructed (realistic detector) p_{T} and η distributions are then used to determine the acceptance x efficiency (A x ϵ) of the detector which is obtained by dividing the generated p_{T} and η distributions by the reconstructed. The A x ϵ obtained is then used to correct the number of muons shown in Table 4.9 to obtain the number of muons produced in the events in each multiplicity bin.

4.5 Acceptance x efficiency results

The two periods, LHC12h and LHC12i are analysed seperately for the A x ϵ because the conditions of the Muon Spectrometer are dependent on the period of data taking. Figure 4.16, shows the generated and the reconstructed p_{T} distributions for the two periods.

The efficiency of the spectrometer for the two periods is determined by taking the ratio between the reconstructed and the generated p_{T} and η distributions. Figure 4.17, shows the A x ϵ in p_{T} while Figure 4.17 shows the A x ϵ in η for periods LHC12h and LHC12i.

Since we are interested in the measurement of muons with $6 < p_{\mathrm{T}} < 20$ GeV/c, we compute the efficiency by taking the average of the efficiency plots in Figure 4.17 in this region of p_{T} and we obtain an efficiency of 68.5% for LHC12h and 71.5% for periods LHC12i CMSH events. The difference in the A x ϵ is due to the variation of the detector status with the period of data taking as mentioned above. The efficiency in η is also shown in Figure 4.17.

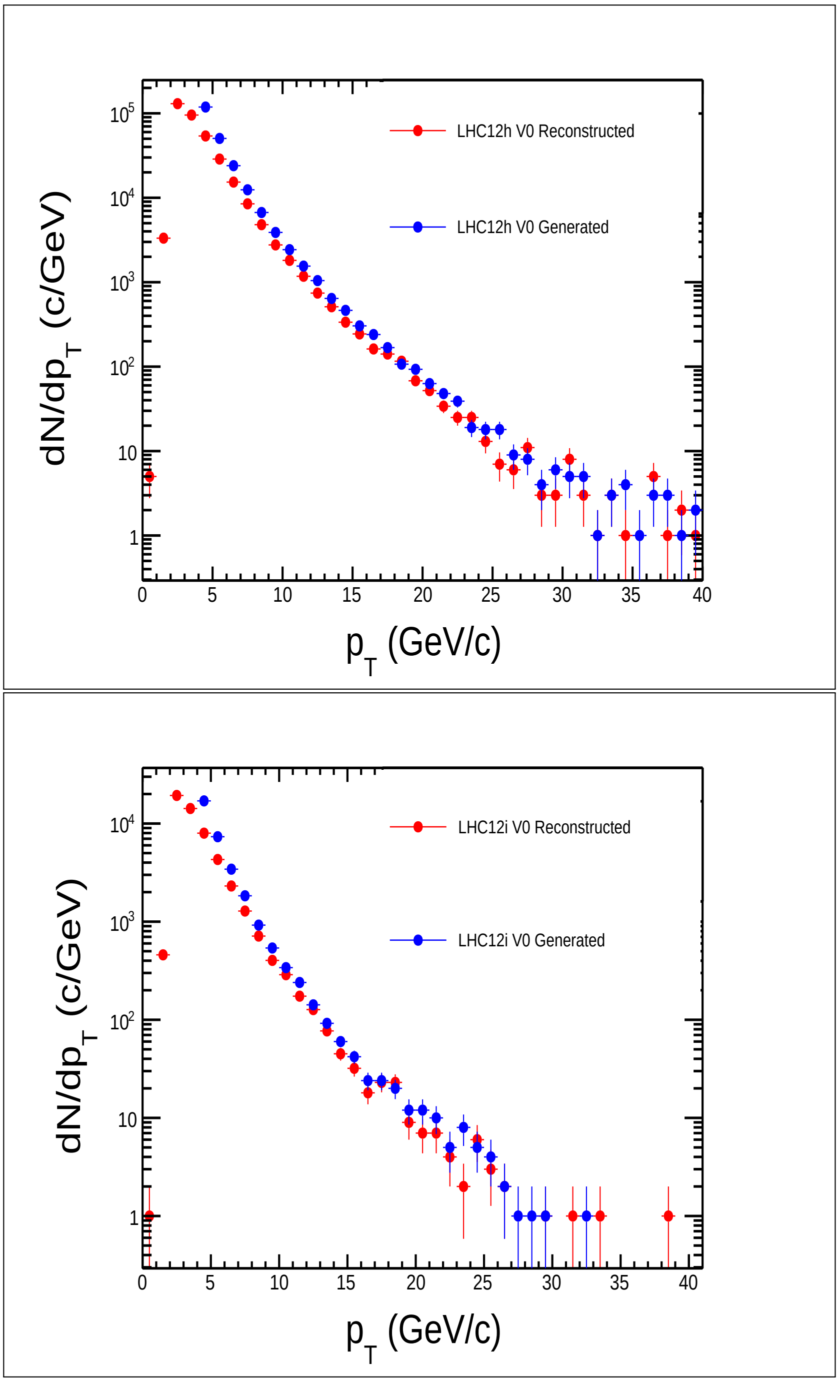

Figure 4.16: The generated (blue) and reconstructed (red) p_{T} distributions for periods LHC12h and LHC12i.

4.6 Muon measurement correction

The efficiency values obtained above are used to correct the number of measured muons to obtain the actual number of muons produced per events. This is done as follows;

$$corrected\ number\ of\ muons = \frac{number\ of\ measured\ muons}{A\ x\ \epsilon} \tag{4.8}$$

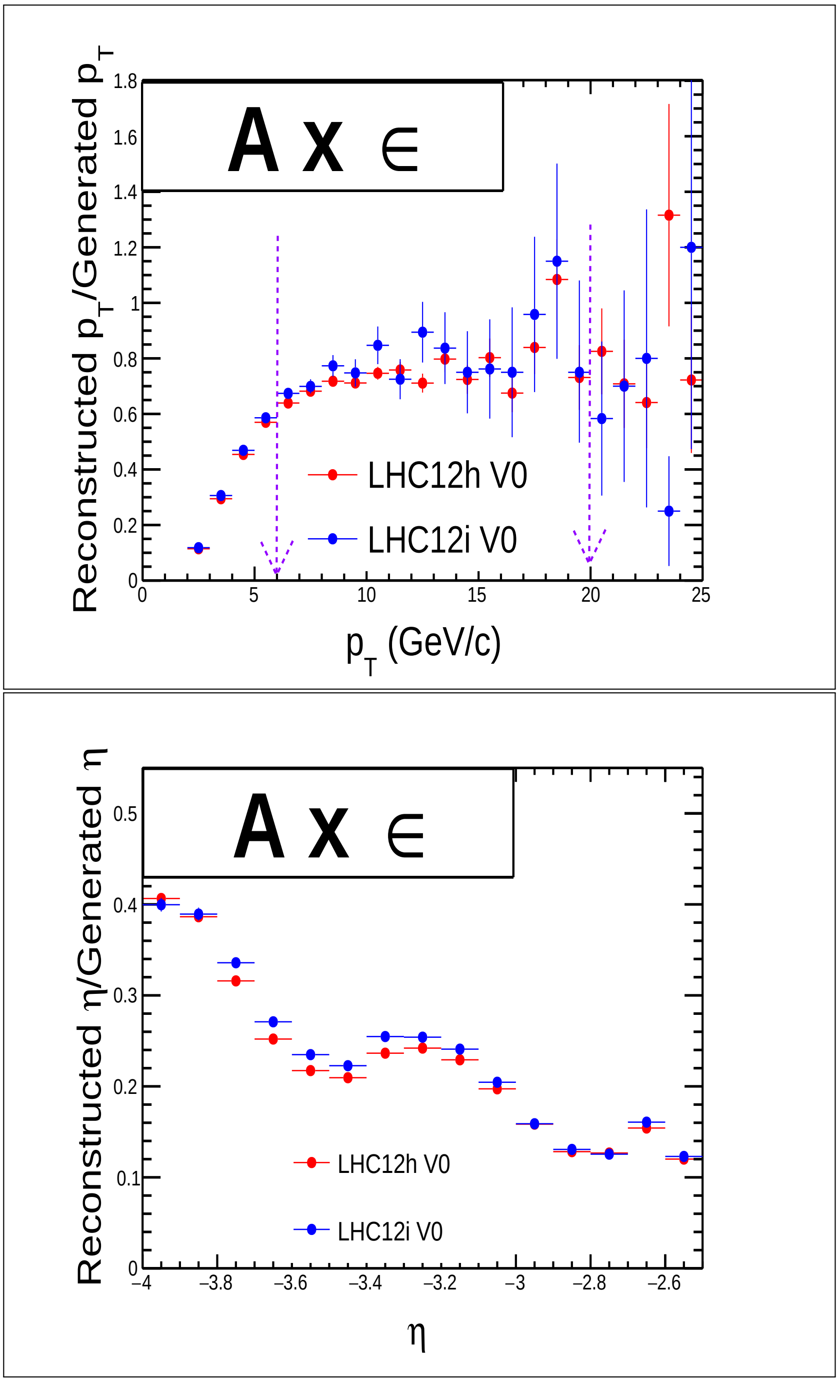

Figure 4.17: The A x ϵ of the muon spectrometer for periods LHC12h and LHC12i CMSH events, the top figure shows the efficiency in p_{T} and the marked region ($6 < p_{\mathrm{T}} < 20$ GeV$/c$) is averaged to get the efficiency of measured muons from heavy flavour decays. The bottom figure is the A x ϵ in the acceptance of the muon spectrometer $-4 < \eta < -2.5$.

The muons are extracted per multiplicity bins discussed in Section 4.3 and the corrected number of muons is shown in Table 4.10.

Table 4.10: The number of muons before and after correction for periods LHC12h and LHC12i with $6 < p_{\mathrm{T}} < 20$ GeV/c

Mult bins	**Measured LHC12h**	**Corrected LHC12h**	**Measured LHC12i**	**Corrected LHC12i**	**Total corrected**
[1,2]	344	502.19	144	201.39	703.59
[3,4]	1846	2 694.89	655	916.08	3 610.97
[5.6]	2833	4 135.77	490	685.31	4 821.08
[7,9]	6009	8 772.26	1009	1 411.19	10 183.45
[10,13]	10306	15 045.26	1656	2 316.08	17 361.34
[14,18]	14536	21 220.44	2327	3 254.55	24 474.98
[19,27]	24094	35 173.72	3877	5 422.38	40 596.10
[28,300]	31745	46 343	4997	6 988.81	53 331.88

The following chapter will discuss the results obtained in the analysis.

Chapter 5

Discussion of results

The aim was to investigate the correction of the yield of muons from decay of heavy flavours with the charged-particle multiplicity. In this chapter we discuss the results obtained in the analysis described in Chapter 4.

5.1 Charged particle multiplicity results

The raw multiplicity of charged particles (Figure 4.2) has been measured using the number of reconstructed tracklets in the optimised region of the SPD, taking into account the cuts given in Table 4.3. This raw multiplicity has been plotted as a function of the vertex position (Figure 4.3), then taking the average of the results in order to see if corrections for SPD acceptance are necessary, i.e. extraction of the tracklet profiles, see Figure 4.4 and Figure 4.6. Accordingly, corrections were then applied to obtain the tracklet profile shown in Figure 4.11 and the corrected multiplicity distribution shown in Figure 4.12. As the corrected multiplicity is not the ”true” multiplicity, a missing factor (α) was extracted via MC simulations and found to be independent of the multiplicity - therefore, assumed negligible. Under this assumption, the charged-particle multiplicity, normalized to the average multiplicity could be plotted. This relative mutliplicity computed using equation 5.1 was sliced into 8 bins. The relative multiplicity at the i^{th} bin is given by;

$$rel.\ N^{i}_{tracklets} = \frac{< N^{i}_{tracklets} >}{< N^{tot}_{tracklets} >} \tag{5.1}$$

and the results are given in Table 5.1. They represent the x-coordinates of the final plot against the yield of muons from the decay of heavy flavours.

5.2 Heavy flavour muon results

The yield of muons is defined as the number of muons per MB event as shown in equation 5.2. The number of events is extracted as discussed in Chapter 4, section 4.3 and are shown in Table 4.10. We present a self normalised yield, which is obtained by computing the yield of heavy flavour muons in each multiplicity bin, as shown in equation 5.2, and the total yield, shown in equation 5.3 and then taking the ratio of the yield to the total yield in each bin.

Table 5.1: The average number of tracklets per multiplicity bin and the relative multiplicity

Mult bins	$<\mathbf{N^{i}}_{\mathbf{tracklets}}>$	$\frac{<N^{\mathbf{i}}_{\mathbf{tracklets}}>}{<N^{\mathbf{tot}}_{\mathbf{tracklets}}>}$
[1,2]	1.59	0.09
[3,4]	3.52	0.20
[5.6]	5.50	0.31
[7,9]	7.99	0.45
[10,13]	11.47	0.65
[14,18]	15.94	0.90
[19,27]	22.64	1.28
[28,300]	37.63	2.13
[1,300]	17.67	

$$Y^{i} = \frac{N^{i}_{\mu}}{(A\ x\ \epsilon)_{i} \cdot N^{i}_{CMSH} \cdot f_{i}} \tag{5.2}$$

$\mathrm{Y^{i}}$ is the yield computed at the i^{th} bin;
$\mathrm{N^{i}}_{\mu}$ is the number of muons in the i^{th} bin
$(\mathrm{A\ x}\ \epsilon)_{\mathrm{i}}$ is the A x ϵ in the i^{th} bin;
$\mathrm{N^{i}}_{\mathrm{CMSH}}$ is the number of CMSH events
$\mathrm{f_{i}}$ is the normalisation factor to pass from number of MB events to CMSH events in the i^{th} bin;

$$Y^{tot} = \frac{N^{tot}_{\mu}}{(A\ x\ \epsilon)_{tot} \cdot N^{tot}_{CMSH} \cdot f_{tot}} \tag{5.3}$$

$\mathrm{Y^{tot}}$ is the total yield
$\mathrm{N^{tot}}_{\mu}$ is the total number of muons
$(\mathrm{A\ x}\ \epsilon)_{\mathrm{total}}$ is the total A x ϵ of the muon spectrometer in the region $6 < p_{\mathrm{T}} < 20$ GeV/c;
$\mathrm{N^{tot}}_{\mathrm{CMSH}}$ is the total number of CMSH events
$\mathrm{f_{tot}}$ is the normalisation factor to pass from number of MB events to CMSH events

Assuming that $(\mathrm{Ax}\epsilon)_{\mathrm{tot}}$ and $\mathrm{f_{tot}}$ do not depend on the multiplicity, the self normalised yield of muons may be given as;

$$\frac{Y_{i}}{Y_{tot}} = \frac{N^{i}_{\mu}}{N^{tot}_{\mu}} \cdot \frac{N^{tot}_{CMSH}}{N^{i}_{CMSH}} \tag{5.4}$$

The self normalised yield of heavy flavour muons in each multiplicity bin is shown in Table 5.2. Therefore the total number of CMSH events ($\mathbf{N^{tot}}_{\mathbf{CMSH}}$) and the number of muons ($\mathbf{N^{tot}}_{\mu}$) in the region $6 < p_{\mathrm{T}} < 20$ GeV/c are;

$\mathbf{N^{tot}}_{\mathbf{CMSH}} = 12\ 159\ 173$ and $\mathbf{N^{tot}}_{\mu} = 155\ 083.19$ respectively.

Table 5.2: The number of events and yield of high-p_{T} single muons

Mult bins	**Number of events** ($\mathbf{N^{i}}_{\mathbf{CMSH}}$)	**Corrected muons** $\frac{N^{\mathbf{i}}_{\mu}}{A\ x\ \epsilon}$	$\frac{Y^{\mathbf{i}}}{Y^{\mathbf{tot}}}$ **rel. yield**
[1,2]	579 891	703.39	0.095
[3,4]	868 698	3 610.97	0.325
[5.6]	926 767	4 821.08	0.408
[7,9]	1 355 621	10 183.45	0.589
[10,13]	1 685 912	17 361.34	0.807
[14,18]	1 854 821	24 474.98	1.035
[19,27]	2 448 024	40 596.10	1.301
[28,300]	2 439 439	53 331.88	1.714

5.3 Correlation of the yield of heavy flavour muons with the charged-particle multiplicity

The relative yield of heavy flavour muons as a function of the relative charged-particle multiplicity is shown in Figure 5.1.

The preliminary results of this study shown in Figure 5.1 show that the yield of

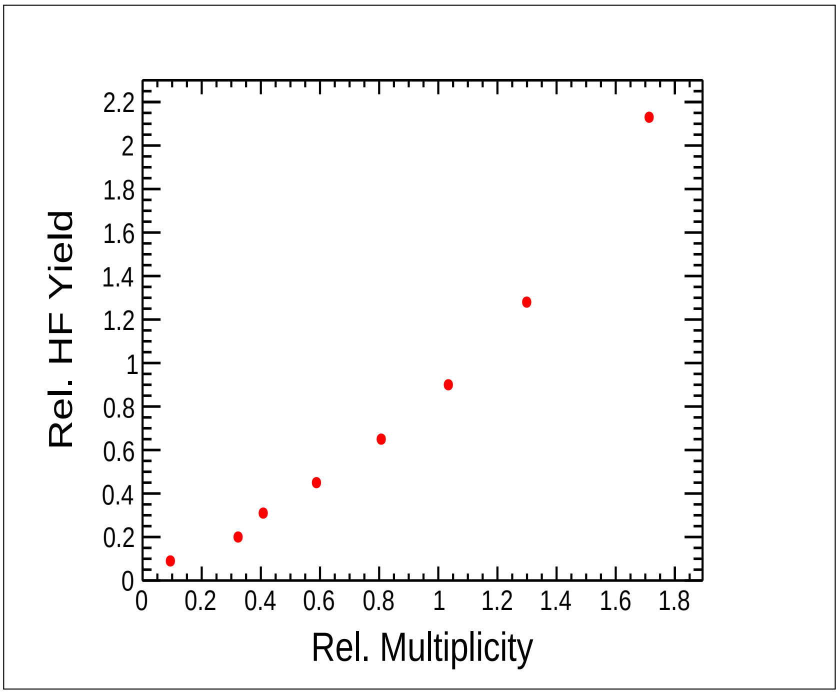

Figure 5.1: The yield of heavy flavour muons as a function of charged-particle multiplicity

heavy flavour decay muons measured in the forward rapidity of ALICE is increasing with the charged-particle multiplicity. This increase might be due to MPI discussed in Chapter 1 and 2, where it was discussed that the multiplicity of charged particles is a direct measure of the number of partonic interactions in the pp events. The high-p_{T} muons of interest in this study are those produced in the region $6 < p_{\mathrm{T}} < 20$ GeV/c, a region in which single muons from the decay of heavy flavours (c and b) are dominant (assuming the contribution of W bosons is negligible below $p_{\mathrm{T}} \sim 20$ GeV/c) [ALI05b]. Therefore, if MPIs affect hard processes where these are produced then the yield of heavy flavour decay muons should scale with the number of partonic collisions and the observed correlation will result.

In Chapter 6 is the summary and conclusions.

Chapter 6

Summary and conclusions

In this study we investigated the correlation of the yield of muons from heavy flavours with charged-particle multiplicity in pp collisions at 8 TeV at forward rapidity with ALICE.

In Chapter 1 we demonstrated, through a review of the previous studies that ALICE, due to its pseudorapidity coverage with respect to other LHC experiments, is competent in the measurements of heavy flavours and charged-particle multiplicity in pp collisions at LHC energies. In previous measurements conducted by ALICE a linear increase was observed for the yield of J/Ψ [COL06] and open charm (D meson) production as a function of charged-particle multiplicity [HFP07]. However, this increase was not reproduced by model predictions, in particular, those describing MPIs. It was concluded that other studies of the production of heavy quarks versus multiplicity are necessary in order to shed more light on the mechanisms influencing these productions. Our study was motivated by these findings.

After the introduction we gave a short description of the theoretical background in Chapter 2, followed by details of the experimental setup, specifically the ALICE Muon Spectrometer in Chapter 3. Essential outline of run conditions and selection criteria applied to obtain the data sample were also given.

The analysis strategy was presented in Chapter 4 where we explained the criteria employed to select events and muon tracks from the data sample ultimately analysed in order to determine the charged-particle multiplicity and heavy flavour muon production. Detailed information on data analysis was provided. This comprised of the techniques used in the measurement of charged-particle multiplicity as well as on the extraction of the yield of single muons measured in the forward rapidity ($-4 < \eta < -2.5$) and integrated in the range $6 < p_{\mathrm{T}} < 20$ GeV/c, the region in which muons from the decay of heavy flavours dorminate, assuming the contribution of W bosons is negligible at $p_{\mathrm{T}} < 20$ GeV/c. Subsequently, present corrections done to take into account the detector acceptance and efficiency.

The results obtained in this study were presented in Chapter 5. In Figure 5.1 it was observed that the yield of heavy flavour muons increases with increasing charged-particle multiplicity. This indicated a strong dependency of the production of heavy flavours to multiplicity. Although the results are preliminary, however, they show the same trend as seen in [COL06] and [HFP07].

The results presented in this thesis are preliminary as they do not include pile-up studies as well as statistical and systematic uncertainties. As an outlook, we aim to study pile-up and systematic uncertainties which will be included and presented as final result. Also, an analysis of data collected during high multiplicity runs in pp collisions at 13 TeV by ALICE in RUN 2 of the LHC in 2015 will be interesting to compare with current results.

Appendix A

Runlists, analysis, simulation and reconstruction Files

A.1 LHC12h and LHC12i Runlists

Below are the runlists of the data considered in this study i.e. LHC12h and LHC12i muon_calo_pass2 AliAOD runs.

LHC12h	**runlist**							
189576	189577	189578	189596	189601	189603	189605	189607	189610
189611	189616	189621	189623	189641	189642	189647	189648	189650
189654	189658	189659	189685	189687	189694	189696	189697	189698
190150	190212	190214	190215	190216	190240	190242	190244	190304
190305	190307	190337	190340	190341	190342	190386	190388	190389
190390	190392	190416	190417	190418	190419	190895	190898	190903
190904	190968	190970	190979	190981	190983	190984	191129	191227
191229	191230	191232	191242	191244	191245	191247	191248	191234
191450	191451	192072	192073	192095	192128	192136	192140	192141
192172	192174	192177	192194	192197	192199	192200	192201	192205
192246	192468	192471	192499	192505	192510	192534	192535	192542
192548	192729	192731	192732	192202	192492	192004	190393	190969
189608	189612	189656	190209	190336	191231			

LHC12i	**runlist**							
192772	192775	192778	192779	192822	192824	193004	193005	193007
193008	193010	193011	193014	193047	193049	193051	192820	

A.2 AliAnalysisTaskPtCMSH.cxx

Below is the analysis task used to obtain the p_{T} multiplicity and the vertex distribution from the analysed data.

It has three main methods, the UserCreateOutputObjects where the multiplicity and p_{T} histograms are created, UserExec where the events and tracks are selected and histograms are filled accordingly and lastly, the Terminate Option where the output of the analysis in the form of histograms is extracted. A header file AliAnalysisTaskCMSH.h, shown in Appendix A.3 is used to declare all the functions, files and histograms used in the analysis task. As mentioned above, the data analysed in this study is stored on the ALICE grid and the analysis is also done on the ALICE grid (see Section 3.5), the analysis task should be adapted for use on the grid. This is done by selecting the correct combination of grid packages, ROOT, AliRoot and AliPhysics[1] versions appropriate for submitting analysis tasks on the grid. The CreateAlienHandler.C, shown in Appendix A.4, is used to set the grid packages as well as the path to the data files to be analysed.

```
#include "TChain.h"
#include "TTree.h"
#include "TH1F.h"
#include "TH1D.h"
#include "TH2F.h"
#include "TAxis.h"
#include "TRandom.h"
#include "TLegend.h"
#include "THnSparse.h"
#include "TCanvas.h"
#include "TFile.h"
#include "AliAnalysisTask.h"
#include "AliAnalysisManager.h"
#include "AliAODEvent.h"
#include "AliESDEvent.h"
#include "AliAODTrack.h"
#include "AliESDInputHandler.h"
#include "AliAODInputHandler.h"
#include "AliMuonTrackCuts.h"
#include "AliMuonEventCuts.h"
#include "AliAnalysisTaskPtCMSH.h"
#include "AliAODTracklets.h"
#include "AliMultiplicity.h"
#include "AliAnalysisTaskMuonCollisionMultiplicity.h"
#include "AliCounterCollection.h"
// example of an analysis task creating a p_t spectrum
// Authors: Panos Cristakoglou, Jan Fiete Grosse-Oetringhaus,
//Klein-Boesing
```

---

[1] A grid software that stores analysis macros used for different physics analysis in ALICE.

```
//Modified by S. Mhlanga to be able to extract the multiplicity & the
// HF muons for the study
// Reviewed: A.Gheata (19/02/10)
ClassImp(AliAnalysisTaskPtCMSH)

AliAnalysisTaskPtCMSH::AliAnalysisTaskPtCMSH(const char *name, TH1D
*hinput) : AliAnalysisTaskSE(name),
ftrclasses(0), fAOD(0), fOutputList(0), fNtracklets(0), fHn(0),
fMuonTrackCuts(0), fMuonEventCuts(0), hmultprofile(0),
Nrand(0), fEventCounter(0) {}
if( hinput ) hmultprofile = new TH1D(*hinput);
Nrand = new TRandom();
fMuonTrackCuts = new AliMuonTrackCuts(Form("TrackCuts_%s",name),
"TrackCuts");
fMuonEventCuts = new AliMuonEventCuts(Form("EventCuts_%s",name),
"event");

fMuonEventCuts = new AliMuonEventCuts(Form("EventCuts_%s",name),
"event");
// Define input and output slots here
// Input slot #0 works with a TChain
DefineInput(0, TChain::Class());
// Output slot #0 id reserved by the base class for AOD
// Output slot #1 writes into a TH1 container
DefineOutput(1, TList::Class());
}
//______________________________________________________________________
void AliAnalysisTaskPtCMSH::UserCreateOutputObjects()
{
// Create histograms
fOutputList = new TList();
fOutputList->SetOwner();
fEventCounter = new AliCounterCollection("EventCounter");
fEventCounter->AddRubric("event","MUON/ANY");
fEventCounter->AddRubric("trigger",10000);
fEventCounter->AddRubric("run",100000);
fEventCounter->Init();
int bins[kNvars] = {100,60,80,300,2};
double min[kNvars] = {0.,-6.,-10,0,-2};
double max[kNvars] = {100.,6.,10,300,2};
fNtracklets = new TH2F("Ntracklets","Ntracklets",bins[2],min[2],max[2],
bins[3],min[3],max[3]);
fHn = new THnSparseD("hn","hn",kNvars,bins,min,max);
fOutputList->Add(fHn);
fOutputList->Add(fNtracklets);
fOutputList->Add(fEventCounter);
PostData(1, fOutputList);
```

```
}
void AliAnalysisTaskPtCMSH::NotifyRun()
fMuonTrackCuts->SetRun(fInputHandler);
void AliAnalysisTaskPtCMSH::UserExec(Option_t *)
{
// Main loop called for each event
// check if the event pass the muon-event selection
if (! fMuonEventCuts->IsSelected(fInputHandler)) return;

// retrive the AOD event
//*********************
fAOD = dynamic_cast<AliAODEvent*>(InputEvent());
if (!fAOD) {
printf("ERROR: fAOD not available\n");
return;
}
// trigger classes selection
//*************************
TString trclasses = fAOD->GetFiredTriggerClasses();
if( ! trclasses.Contains(ftrclasses) ) return;
// count events
//**************
fEventCounter->Count(Form("event:MUON/trigger:%s/run:%d",
trclasses.Data(),fCurrentRunNumber));
// check for a good vertex
//***********************
const AliAODVertex* trkVtx = fAOD->GetPrimaryVertex();
if (!trkVtx || trkVtx->GetNContributors()<=0) return;
TString vtxTtl = trkVtx->GetTitle();
if (!vtxTtl.Contains("VertexerTracks")) return;
//   Float_t zvtx = trkVtx->GetZ();
AliAODVertex *vz = fAOD->GetPrimaryVertexSPD();
if (vz->GetNContributors()<=0) return;
TString vtxTyp = vz->GetTitle();
Double_t cov[6]={0};
vz->GetCovarianceMatrix(cov);
Double_t zRes = TMath::Sqrt(cov[5]);
if (vtxTyp.Contains("vertexer: Z")&&(zRes>0.25)) return;// resol. cut
if (TMath::Abs(trkVtx->GetZ() - vz->GetZ())>0.5) return; //difference
//between the main vertex and the SPD
if ( vz->GetZ() < -10. || vz->GetZ() > 10. ) return;
// count the tracklet multiplicity
//*******************************
Int_t multiplicity = 0;
AliAODTracklets *tracklets = fAOD->GetTracklets();
Int_t nTracklets = tracklets->GetNumberOfTracklets();
for (Int_t nn = 0; nn < nTracklets; nn++){
```

```
// consider only tracklets in the good eta range
Double_t theta = tracklets->GetTheta(nn);
Double_t eta = -TMath::Log(TMath::Tan(theta/2.0));
if ( TMath::Abs(eta) > 1.0) continue; // Eta Cut implemented here
multiplicity += 1;
} // end tracklets loop
if ( multiplicity < 1 ) return; // skip event with 0 tracklets
// correction for the SPD acceptance
// if hmultprofile is not present the correction is not applied
//****************************************************************
double corrfactor = 1.;
if( hmultprofile) corrfactor = hmultprofile->GetMaximum()/hmultprofile
->GetBinContent(hmultprofile->FindBin( vz->GetZ() ));
cout << "Nref = " << hmultprofile->GetMaximum() << endl;

//poisson randomization
//*********************
double deltaN = (corrfactor * multiplicity) - multiplicity;
//difference between corrected and the measured number of tracklets
int missingtracklets = Nrand->PoissonD(TMath::Abs(deltaN));
cout << "Number of missing tracklets = " << missingtracklets << endl;
int corrmult = multiplicity + missingtracklets; //correct tracklets
// fill the multiplicity vs vertex histogram
//******************************************
fNtracklets->Fill(vz->GetZ(),corrmult);
// informations about muons
//************************
// create data array used to fill the THnSparse fHn
Double_t data[kNvars];
data[kMult] = corrmult;
data[kVz]   = vz->GetZ();
bool aretheregoodmuons = kFALSE;
for ( Int_t iTracks = 0; iTracks < fAOD->GetNumberOfTracks();
iTracks++ ) {
AliAODTrack* track=dynamic_cast<AliAODTrack*>(fAOD->GetTrack(iTracks));
if (!track) {
printf("ERROR: Could not receive track %d\n", iTracks);
continue; }
if (!fMuonTrackCuts->IsSelected(track)) continue;
data[kPt]         = track->Pt();
data[kEta]         = track->Eta();
data[kCharge] = track->Charge()/3;
aretheregoodmuons = kTRUE;
// fill for _each_ muon
fHn->Fill(data);
}PostData(1, fOutputList);
}
```

```
void AliAnalysisTaskPtCMSH::Terminate(Option_t *)
{
// Draw result to the screen
// Called once at the end of the query

// get first part of trigger name
TString naming = this->GetName();
naming.Resize( naming.First("_") );

// prepare string for naming stuff
TString name;

// retrieve the output list
//***************************
fOutputList = dynamic_cast<TList*> (GetOutputData(1));
if (!fOutputList) {
printf("ERROR: Output list not available\n");
return;
}

SetStyle(kFALSE);

// get output histograms/containers from the list
//***********************************************

fNtracklets = (TH2F*)fOutputList->FindObject("Ntracklets");
fEventCounter = (AliCounterCollection*)fOutputList->
FindObject("EventCounter");
fHn = (THnSparse*)fOutputList->FindObject("hn");

// print event conter information
fEventCounter->Print("event");

// Tracklet multiplicity vs Vertex position

name = naming + "_Multip";
TCanvas *c6 = new TCanvas(name.Data(),name.Data(), 10,10,510,510);
c6->cd(1)->SetLogz();
fNtracklets->GetXaxis()->SetTitle("Vertex (cm)");
fNtracklets->GetYaxis()->SetTitle("Number of tracklets ");
fNtracklets->GetYaxis()->SetTitleOffset(1.5);
fNtracklets->GetXaxis()->CenterTitle(1);

fNtracklets->SaveAs(Form("%s_2D.root",naming.Data()));
fNtracklets->Draw("colz");
fNtracklets->SaveAs(Form("%s_2D.root",naming.Data()));
```

```
name = naming + "_hprof";
TH1D *hp = new TH1D(name.Data(), "hp",80, -10,10);
double mean = 0;
TH1D* h1;
for(int j = 0; j<80;j++){
h1 = (TH1D*)fNtracklets->ProjectionY("_px",j+1,j+1,"");
h1->SetName(Form("%i",j));
mean = h1->GetMean(1);
hp->SetBinContent(j+1,mean);
}
hp->SetLineColor(kBlack);
hp->Draw("same");

hp->SaveAs(Form("%s_fproj.root",naming.Data()));

//+++++++++++++++++++++++++++++++++++++++++++++++++++
// Tracklet multiplicity distribution


name = naming + "_multiplicity";
TCanvas *c1 = new TCanvas(name.Data(), name.Data(), 10,10,510,510);
c1->cd(1)->SetLogy();
TH1D* hist1 = fNtracklets->ProjectionY();
name = naming + "_h_multiplicity";
hist1->SetName(name.Data());
hist1->SetTitle("Tracklet multiplicity");
hist1->GetXaxis()->SetTitle("Ntracklets");
hist1->GetYaxis()->SetTitle("Number of Events");
hist1->GetYaxis()->SetTitleOffset(1.5);
hist1->GetXaxis()->SetTitleOffset(1.0);
hist1->GetXaxis()->CenterTitle(1);
hist1->Draw("");
hist1->SaveAs(Form("%s_multi.root",naming.Data()));

//+++++++++++++++++++++++++++++++++++++++++++++++++++
// vertex distribution
name = naming + "_vertex";
TCanvas *ccc = new TCanvas(name.Data(), name.Data(), 10,10,510,510);
ccc->cd(1)->SetLogy();
TH1D* histvz = fNtracklets->ProjectionX();
name = naming + "_h_vertex";
histvz->SetName(name.Data());
histvz->SetTitle("vertex distribution");
histvz->GetXaxis()->SetTitle("vertex position (cm)");
histvz->GetYaxis()->SetTitle("Entries");
histvz->GetXaxis()->CenterTitle(1);
histvz->Draw();
```

```
// muon pT distribution
name = naming + "_canvas_pT";
TCanvas *c12 = new TCanvas(name.Data(), name.Data(), 10,10,510,510);
c12->cd(1)->SetLogy();
//   fHn = (THnSparse*)fOutputList->FindObject("hn");
fHn->GetAxis(kMult)->SetRangeUser(0,300);

name = naming + "_transverse_momentum";
TH1D* hist2 = fHn->Projection(kPt, name.Data());
//   fHn->GetAxis(kPt)->SetRangeUser(0,100);

hist2->GetXaxis()->SetTitle("Pt (GeV/c)");
hist2->GetYaxis()->SetTitle("dN/dPt (c/GeV)");
hist2->GetYaxis()->SetTitleOffset(1.5);
hist2->GetXaxis()->SetTitleOffset(1.0);
hist2->GetXaxis()->CenterTitle(1);

hist2->Draw();
double integral =  hist2->Integral(6,30);
/   cout << "integral= "<< integral << endl;
hist2->Draw("E1");
hist2->SaveAs(Form("%s_corrpt.root",naming.Data()));

// muon Yield vs multiplicity

Int_t multLimits[] = {0,8,13,16,20,25,300}; //multiplicity bin limits
const Int_t kNumMultLimit = 6; // the number of multiplicity bins + 1

//Let's define the pT integration limits
Float_t pTmin = 6.;  // in GeV/c
Float_t pTmax = 20.;  // in GeV/c

// getting the pT of the muons in the multiplicity bins:
Int_t pTbinMin = fHn->GetAxis(kPt)->FindBin(pTmin);
Int_t pTbinMax = fHn->GetAxis(kPt)->FindBin(pTmax);

//pT distribution plots
name = naming + "_canvas_pT_in_mult_bins";
TCanvas *c13 = new TCanvas(name.Data(), "pT distributions in different
multiplicity bins", 10,10,510,510);
c13->cd(1)->SetLogy();
TH1 *hframe =
c13->cd(1)->DrawFrame(0.,0.9,80., hist2->GetMaximum(),naming.Data() );

// multiplicity bins loop starts here.
for( int imult = 0; imult < kNumMultLimit; imult++){
```

```
// definition of the multiplicity limits
Int_t minMultLimit = multLimits[imult]+1;
Int_t maxMultLimit = multLimits[imult+1];

// set the range for the kMult axis
fHn->GetAxis(kMult)->SetRangeUser( minMultLimit, maxMultLimit);

TH1D* hist3 = fHn->Projection(kPt, Form("%s_pt_mult_%d",
naming.Data(),imult));
hist3->SetLineColor( imult+1);
hist3->Draw("esame");

// integrating in 6 < pT < 20 GeV/c to get no. of muons within this pT
range
double integral1 =  hist3->Integral( pTbinMin, pTbinMax);

}// end of the  loop on multiplicity bins

}
```

A.3 AliAnalysisTaskPtCMSH.h

```
#ifndef AliAnalysisTaskPtCMSH_cxx
#define AliAnalysisTaskPtCMSH_cxx
class TH1F;
class TH2F;
class AliAODEvent;
class AliMuonTrackCuts;
class AliMuonEventCuts;
class THnSparse;
class TString;
class AliCounterCollection;
#include "AliAnalysisTaskSE.h"
class AliAnalysisTaskPtCMSH : public AliAnalysisTaskSE {
public:
AliAnalysisTaskPtCMSH() : AliAnalysisTaskSE(),
ftrclasses(0), fAOD(0), fOutputList(0), fNtracklets(0), fHn(0),
fMuonTrackCuts(0), fMuonEventCuts(0), hmultprofile(0), Nrand(0),
 fEventCounter(0)
//Constructor
AliAnalysisTaskPtCMSH(const char *name, TH1D *hinput = 0x0);
//Destructor
virtual ~AliAnalysisTaskPtCMSH() {}
virtual void   UserCreateOutputObjects();
virtual void   NotifyRun();
virtual void   UserExec(Option_t *option);
virtual void   Terminate(Option_t *);
enum{kPt,kEta,kVz,kMult,kCharge,kNvars};
void SetTriggerClasses(TString st){ ftrclasses = st;  }
AliMuonTrackCuts* GetMuonTrackCuts() { return fMuonTrackCuts; }
AliMuonEventCuts* GetMuonEventCuts() { return fMuonEventCuts; }
virtual void SetStyle(Bool_t graypalette);
private:
TString ftrclasses;  //<
AliAODEvent                 *fAOD;    //! ESD object
TList                       *fOutputList; //! Output list
TH2F                        *fNtracklets; //!
THnSparse                *fHn;         //!
TH1D *hmultprofile;
TRandom *Nrand;
AliMuonTrackCuts* fMuonTrackCuts;
AliMuonEventCuts* fMuonEventCuts;
AliCounterCollection* fEventCounter;
AliAnalysisTaskPtCMSH(const AliAnalysisTaskPtCMSH&);
AliAnalysisTaskPtCMSH& operator=(const AliAnalysisTaskPtCMSH&);
ClassDef(AliAnalysisTaskPtCMSH, 1);
};#endif
```

The 3 macros that follow, namely the CreateAlienHandler.C, the runGrid.C and the AddTask.C are used to enable the analysis task to be submitted on the ALICE grid where the analysis of the data is done.

A.4 CreateAlienHandler.C

```
AliAnalysisGrid* CreateAlienHandler()
{
AliAnalysisAlien *plugin = new AliAnalysisAlien();
plugin->SetRunMode("full");

// Set versions of used packages
plugin->SetAPIVersion("V1.1x");
plugin->SetROOTVersion("v5-34-08-7");
plugin->SetAliROOTVersion("v5-06-12");
plugin->SetAliPhysicsVersion("vAN-20150410");

//////////////////////
// Analysis on grid //
//////////////////////
// Declare input data to be processed.
plugin->SetGridDataDir("/alice/data/2012/LHC12i/");

// Set data search pattern
plugin->SetRunPrefix("000");
plugin->SetDataPattern("*ESDs/muon_calo_pass2/AOD/*/AliAOD.root");
// ...then add run numbers to be considered
const char *runListName = "runlist_12i_V0_144mods.txt";
if(!runListName) {
cout << "run list file name not found!!!" <<endl;
return NULL;
}
ifstream runListFile;
runListFile.open((char*)runListName);
Int_t runNr;
if (runListFile.is_open()) {
while (kTRUE){
runListFile >> runNr;
if(runListFile.eof()) break;
cout<<runNr<<"\n";
plugin->AddRunNumber(runNr);
} }
else {
cout << "run list file "<<runListName<<" not found..." <<endl;
return NULL;
}
runListFile.close();
```

```
// Define grid work directory where all files will be copied.

plugin->SetGridWorkingDir("multiplicity_task_new_corrmax");
plugin->SetFileForTestMode("aod.txt");

// Declare grid output directory. Relative to working directory.
plugin->SetGridOutputDir("multiplicity_task_new_corrmax");


// Declare the analysis source files names separated.
plugin->SetAnalysisSource("AliAnalysisTaskPtCMSH.cxx
AliAnalysisTaskPtCMSH.h");

plugin->SetAdditionalLibs("libCORRFW.so libPWGmuon.so");

plugin->SetAnalysisMacro("MyAnalysis.C");

// Optionally add include paths
plugin->AddIncludePath("-I.");
plugin->AddIncludePath("-I$ALICE_ROOT/include");
plugin->AddIncludePath("-I$ALICE_PHYSICS/include");
plugin->SetMergeViaJDL();
return plugin;
}
```

A.5 runGrid.C

```
void runGrid()
{
// Load common libraries
gSystem->Load("libCore.so");
gSystem->Load("libTree.so");
gSystem->Load("libGeom.so");
gSystem->Load("libVMC.so");
gSystem->Load("libPhysics.so");
gSystem->Load("libMinuit.so");
gSystem->Load("libSTEERBase");
gSystem->Load("libESD");
gSystem->Load("libAOD");
gSystem->Load("libANALYSIS");
gSystem->Load("libANALYSISalice");
gSystem->Load("libCORRFW");
gSystem->Load("libPWGmuon");
// Use AliRoot includes to compile our task
gROOT->ProcessLine(".include $ALICE_ROOT/include");
gROOT->ProcessLine(".include $ALICE_PHYSICS/include");
gSystem->AddIncludePath("-I.");
// Create and configure the alien handler plugin
gROOT->LoadMacro("CreateAlienHandler.C");
AliAnalysisGrid *alienHandler = CreateAlienHandler();
if (!alienHandler) return;
// Create the analysis manager
AliAnalysisManager *mgr = new AliAnalysisManager("testAnalysis");
// Connect plug-in to the analysis manager
mgr->SetGridHandler(alienHandler);
gROOT->LoadMacro("AliAnalysisTaskPtCMSH.cxx++g");
// input handler
AliAODInputHandler* aodH = new AliAODInputHandler();
aodH->SetCheckStatistics(kTRUE);
mgr->SetInputEventHandler(aodH);
gROOT->LoadMacro("AddTask.C");
AddTask( "CMSH7-S-NOPF-MUON", kFALSE );
AddTask( "CINT7-S-NOPF-ALLNOTRD", kFALSE );
AddTask( "CMSL7-S-NOPF-ALLNOTRD", kFALSE );
// Enable debug printouts
mgr->SetDebugLevel(0);
if (!mgr->InitAnalysis())
return;
mgr->PrintStatus();
// Start analysis
mgr->StartAnalysis("grid"); // Use this for grid
};
```

A.6 AddTask.C

```
#if !defined(__CINT__) || defined(__MAKECINT__)
#include "TString.h"
#include "AliAnalysisManager.h"
#include "AliAnalysisDataContainer.h"
#include "AliMuonTrackCuts.h"
#include "AliMuonEventCuts.h"
#include "AliAnalysisTaskPtCMSH.h"
#endif
AliAnalysisTaskPtCMSH *AddTask(TString trigger, Bool_t useMC){
AliAnalysisManager *mgr = AliAnalysisManager::GetAnalysisManager();
if (!mgr) {
::Error("AddtaskSingleMu", "No analysis manager to connect to.");
return NULL;
}
// open input file
TFile *inf = TFile::Open("/CINT7_fproj.root"); \\ open Raw tracklet
profile
TH1D *hinputprofile = (TH1D*) inf->Get("CINT7_hprof");
hinputprofile = (TH1D*) hinputprofile->Clone("profile");
hinputprofile->SetDirectory(0);
inf->Close();
//  my task
TString naming = trigger;
naming.ReplaceAll("-","_");
AliAnalysisTaskPtCMSH *task = new AliAnalysisTaskPtCMSH(Form(
"%s_Task",naming.Data()), hinputprofile);
// specific setting for my task
Bool_t isMC = kFALSE;
task->GetMuonTrackCuts()->SetFilterMask (
AliMuonTrackCuts::kMuEta |AliMuonTrackCuts::kMuThetaAbs |
AliMuonTrackCuts::kMuPdca | AliMuonTrackCuts::kMuMatchHpt);
task->GetMuonTrackCuts()->SetIsMC(useMC);
task->GetMuonTrackCuts()->Print("mask");
task->GetMuonTrackCuts()->SetPassName("muon_calo_pass2");
task->GetMuonTrackCuts()->SetAllowDefaultParams(kTRUE);
task->GetMuonTrackCuts()->ApplySharpPtCutInMatching(kTRUE);
task->GetMuonEventCuts()->SetFilterMask ( AliMuonEventCuts::
kPhysicsSelected | AliMuonEventCuts::kSelectedTrig | AliMuonEventCuts
::kGoodVertex );
task->GetMuonEventCuts()->SetVertexMinNContributors(1);
task->GetMuonEventCuts()->SetVertexVzLimits(-10., 10.);
task->GetMuonEventCuts()->SetTrigClassPatterns(trigger.Data(),
"0MSH:13");
mgr->AddTask(task);
AliAnalysisDataContainer *cinput = mgr->GetCommonInputContainer();
```

```
AliAnalysisDataContainer *coutput3 =
mgr->CreateContainer(Form("chist_%s",naming.Data()), TList::Class(),
AliAnalysisManager::kOutputContainer, Form("MSH_corr.root:%s",
naming.Data()));
mgr->ConnectInput(task, 0, cinput);
mgr->ConnectOutput(task, 1, coutput3);
return task;
}
```

A.7 sim.C

Below is the simulation macro that is used to reproduce the p_{T} and η distributions that would be obtained if the Muon spectrometer was 100 % efficient.

```
void sim(Int_t nev=VAR_EVENTS_PER_JOB)
{
#if defined(__CINT__)
gSystem->Load("VAR_LHAPDF");      // Parton density functions
if (TString("VAR_GENERATOR").Contains("pythia6",TString::kIgnoreCase))
{
std::cout << "Setting up Pythia6 required env. variables" << std::endl;
VAR_PYTHIA6_INCLUDES
VAR_PYTHIA6_SETENV
}
else  gSystem->Load("libpythia6");     // Pythia 6.2 (for decayer)
if (TString("VAR_GENERATOR").Contains("pythia8",TString::kIgnoreCase))
{
VAR_PYTHIA8_INCLUDES
VAR_PYTHIA8_SETENV
        }
        #endif
if ( VAR_PURELY_LOCAL) {
TGeoGlobalMagField::Instance()->SetField(new AliMagF
("Maps","Maps", -1., -1, AliMagF::k5kG));
}
AliSimulation simulator;
simulator.SetRunQA("MUON:ALL");
simulator.SetRunHLT("");
        if ( VAR_USE_ITS_RECO )
{
simulator.SetMakeSDigits("MUON T0 VZERO"); // T0 & V0 for trigger
 efficiencies
simulator.SetMakeDigitsFromHits("ITS"); // ITS to propagate the
simulated vertex
simulator.SetMakeDigits("MUON T0 VZERO FMD");
}
else
{
simulator.SetTriggerConfig("MUON");
simulator.SetMakeSDigits("MUON");
simulator.SetMakeDigits("MUON");// ITS"); // ITS to propagate the
simulated vertex
}
simulator.SetDefaultStorage(VAR_OCDB_PATH);
if ( VAR_OCDB_SNAPSHOT )
```

```
{
simulator.SetCDBSnapshotMode("OCDB_sim.root");
}
if ( ! VAR_PURELY_LOCAL ) {
simulator.SetSpecificStorage("MUON/Align/Data",VAR_SIM_ALIGNDATA);
simulator.UseMagFieldFromGRP();
if ( VAR_USE_ITS_RECO )
{
simulator.SetSpecificStorage("ITS/Align/Data",
 "alien://Folder=/alice/simulation/2008/v4-15-Release/Ideal");
simulator.UseVertexFromCDB();
}
}
TStopwatch timer;
timer.Start();
simulator.Run(nev);
timer.Stop();
timer.Print();
}
```

A.8 rec.C

Below is the reconstruction macro used to reproduce the p_{T} and η distribution taking into account the actual detector conditions run by run for pp collisions at 8 TeV in 2012.

```
void rec(){
AliReconstruction reco;
reco.SetRunQA("MUON:ALL");
reco.SetCleanESD(kFALSE);
reco.SetStopOnError(kFALSE);
reco.SetDefaultStorage("raw://");
if ( 0 )
{ reco.SetRunReconstruction("VZERO T0 MUON ITS FMD");
}
else
{        reco.SetRunReconstruction("MUON");
}
AliCDBManager* man = AliCDBManager::Instance();
man $\rightarrow$ SetDefaultStorage("alien://folder=
/alice/data/2012/OCDB");
man $\rightarrow$ SetSpecificStorage("GRP/GRP
/Data",Form("local:// %s",gSystem->pwd()));
man $\rightarrow$ SetSpecificStorage("MUON/Align
/Data","alien://folder=/alice/
simulation/2008/v4-15-Release/Residual");
man $\rightarrow$ SetSpecificStorage("MUON/Calib
/RecoParam","alien://folder
=/alice/data/2012/OCDB",5,0);
reco.SetRunPlaneEff(kTRUE);
reco.SetUseTrackingErrorsForAlignment("ITS");
reco.SetSpecificStorage("ITS/Align/Data","alien://
folder=/alice/simulation/2008/v4-15-Release/Residual");
reco.Run();
}
```

Bibliography

[A+01] ALICE Collaboration. *Journal of Instrumentation*, 3:S08002, 2008.

[A+02] ALICE Collaboration. *Journal of Instrumentation*, 5:P03003, 2010.

[A+03] ATLAS Collaboration. *New Journal of Physics*, 13:053033, 2011.

[A+04] ALICE Collaboration. *Journal of High Energy Physics*, 11:065, 2012.

[A+05] ALICE Collaboration. *Physics Letters*, B727:371–380, 2013.

[AB+01] S. M. Sanches Jr, D. A. Fogaca, F. S. Navarra *Journal of Physics Confrence Series 630 012028*.

[AB+02] Ulrich Heinz, Maurice Jacob *arXiv:nucl-th/0002042v1* .

[AB+03] M. Gyulassy *arXiv:nucl-th/0403032v1* .

[AB+04] Gines Martinez Garcia *arXiv:nucl-th/1304.1452v1* .

[AB+05] Fu-Minh Liu, Klaus Werner *arXiv:1106.5909v1 [hep-ph]* .

[AB+06] Gines Martinez Garcia *arXiv:nucl-th/1304.1452v1* .

[AB+06] The ALICE Collaboration *arXiv:1112.2082v3 [hep-ex]* .

[AB+07] Dirk Zerwas *Journal of Physics Conference Series 485 012011* .

[ABS] Matthieu Lenhardt. `https://indico.cern.ch/event/114069/session/6/contribution/46/attachments/45279/65157/Vienne2011-Lenhardt_v3.pdf` 2011.

[ABT] Indranil Das. `https://indico.cern.ch/event/269667/session/7/contribution/20/attachments/483514/668683/Autun_Indra_Charmonia_Bottomonia.pdf`

[ALI01] The ALICE Collaboration. ALICE Figure Repository. 2013 `https://aliceinfo.cern.ch/Figure/node/3402`.

[ALI02] The ALICE Collaboration, *Journal of Physics G: Nuclear and Particle Physics,* 30,1517-1763, 2004.

[ALI03] The ALICE Collaboration. `http://aliceinfo.cern.ch/Offline/AliRoot`. 2011.

[ALI04] Worldwide LHC Computing Grid. `http://wlcg-public.web.cern.ch/tier-centres`.

[ALI05a] The ALICE Collaboration. *Physics Letters B. 2012.01.063*, 2012.

[ALI05b] Conesa Del Vaile, Zaida. *HAL Id: tel-00198703,* 2008.

[ALI06] The ALICE Collaboration. *Journal of Physics G: 32(10):1295, 2006.*

[ALI07] The ALICE Collaboration. *CERN-LHCC-99-032.*

[ALI08] The ALICE Collaboration *ALICE Technical Design Report 2,* 1999.

[ALI09] The ALICE Collaboration *ALICE Technical Design Report 4*, 1999.

[ALI010] The ALICE Collaboration. *Physics Letters B708 (2012) 265-275.* 2012.

[ALI011] The ALICE Collaboration *CERN-LHCC-2003-062, ALICE-TRD-10.* 1999.

[ALI012] The ATLAS Collaboration. *arXiv:1109.0525 [hep-ex].* 2012.

[ALI013] The ATLAS Collaboration. *arXiv:1003.3124 [hep-ex].* 2010.

[ALI013a] The ATLAS Collaboration. *arXiv:1012.5104 [hep-ex].* 2010.

[APO94] J. Apostalakis. `http://wwwasdoc.web.cern/wwwasdoc/geant_html3/geantall.html`.

[ATL01] The ATLAS Collaboration. *Journal of Instrumentation,* Vol. 3, no. S08003. 2008.

[B+11] The ALICE Collaboration. *ANL-HEP-PR-11-65.* 2011.

[BC03] R Bailey and Paul Collier. *LHC-PROJECT-NOTE-323.*

[BCG+14] X. Buffat, R. Calaga, R. Giachino, W. Herr, G. Papotti,. *arXiv:1410.5695 [physics.acc-ph],* 2014.

[BEH+11] N. Brambilla, S. Eidelman, B.K. Heltsley, R. Vogt, G.T. Bodwin, *et al*, *The European Physical Journal C71:1534*, 2011.

[BET13] Siegfried Bethke. *Progress in Particle and Nuclear Physics, 58:351–386,* 2013.

[BEV12] Francesco Bossù. *The ALICE muon spectrometer: trigger detector performance and readiness for the first physics measurements.* `http://inspirehep.net/record/1186163/files/CERN-THESIS-2012-073.pdf`

[BNL12] M. Richter. *CERN-THESIS-2009-189.*

[BRU95] R Brun `http://root.cern.ch/ch/,1995`.

[CAR01] P. Giubellino. A Morsh. G Paic J-P Revol. K Safarik, *et al. Journal of Physical Review D, 9:3471-3495,* 1974

[CAS07] J Castillo. `https://cds.cern.ch/record/1047110/files/p127.pdf`.

[CBN13] C Christensen and B Nielsen. *International Journal of Modern Physics E16 (2007) 2432-2437,* Sep 2013.

[CER01] Michael Richmond. `http://spiff.rit.edu/richmond/asras/lhc/lhc.html#lhc`.

[CER02] CERN PhotoLab *LHC-PHO-1998-349-1.*

[CGN97] Matteo Cacciari, Mario Greco, and Paolo Nason. `www.lpthe.jussieu.fr/~cacciari/fonll/fonllform.html`.

[CGN98] Matteo Cacciari, Mario Greco, and Paolo Nason. *Journal of High Energy Physics, 9805:007*, 1998.

[CHS07a] John M. Campbell, J. W. Huston, and W. J. Stirling. *Report on Progress in Physics., 70:89*, 2007.

[CHS07b] John M. Campbell, J. W. Huston, and W. J. Stirling. *Report on Progress in Physics.*, 70:89, 2007.

[CMS01] The CMS Collaboration. *Journal of Instrumentation, 03:S08004,* 2008.

[CMS02] The ALICE Collaboration. *Journal of Physics Conference Series 509 (2014) 012081* 2008.

[CNV05] Matteo Cacciari, Paolo Nason, and Ramona Vogt. *Physical Review Letters*, 95:122001, Sep 2005.

[COL01] The ALICE Collaboration. *ALICE Technical Design report: Detector for high momentum PID.* Technical Design Report, ALICE 1998. `http://inspirehep.net/record/483568?ln=en`

[COL02] The ALICE Collaboration *ALICE Technical Design report of the time-of-flight system (TOF).* Technical Design Report. ALICE, CERN, Geneva, 2000. `http://inspirehep.net/record/541223?ln=en`

[COL03] The ALICE Collaboration. *ALICE forward detectors: FMD, TO and VO: Technical Design Report.* Technical Design Report, ALICE. 2004. `https://cds.cern.ch/record/781854`.

[COL04] The ALICE Collaboration. *Journal of Physics G: Nuclear and Particle Physics 30(11):1517*, 2004.

[COL05] The ALICE Collaboration. *CERN-ATS-2011-050 :3 p.* 2011.

[COL06] The ALICE Collaboration. *Physics Letters B712:165–175*, 2012.

[COL07] The ALICE Collaboration. *International Journal of Modern Physics A20:1430044,* 2014.

[COL08] The ALICE Collaboration. *Nuclear Instruments and Methods in Physics Research , A741:130–162,* 2014.

[COO] The ALICE Collaboration `https://edms.cern.ch/document/406391/2`.

[CSS89] John C. Collins, Davison E. Soper, and George F. Sterman. *Advanced Service Direct High Energy Phys., 5:1–91,* 1989.

[CTEQ] P. Nadolsky *et al. arXiv:0802.0007 [hep-ph].*

[ETS] Ethan Siegel. `http://scienceblogs.com/startswithabang/2011/04/26/higgs-at-the-lhc-rumors-and-ge/`

[FER05] A. Fasso A. Ferrari, P.R. Sala and J. Ranft. *CERN-2005-010.* 2005.

[FWD01] F. Wilczek, B Devine. Fantastic Realities (2006), World Scientific,. p.85, ISNB 981-256-649-X.

[FWD02] F. Wilczek, B Devine (2006), World Scientific, p.400ff, ISNB 981-256-649-X.

[FWD03] M. Veltman (2003), World Sientific. World Scientic, pp.45-47, ISNB 918-238-149-X.

[FWD04] T. Yulsman (2002). CRS Press. p. 55, ISNB 0-7503-0765-X.

[GMS05] Grigorian, A. and Grossiord, J. Y. and Gulkanian, H. and Tieulent, *et al. HAL Id: in2p3-00025208,* 2005.

[GOR10] Jan Fiete Grosse-Oetringhaus and Klaus Reygers. *Journal of Physics, G37:083001*, 2010.

[GW73] David J. Gross and Frank Wilczek. *Physical Review Letters, 30:1343–1346*, 1973.

[HFP01] R. Averbeck *arXiv:0910.2364v1[hep-ph].*

[HFP02] The ALICE Collaboration *Journals of High Energy Physics 07(2012) 191.*

[HFP03] The ALICE Collaboration *Physical Reviews D86, 112007 (2012).*

[HFP04] The ALICE Collaboration *European Physical Journal C74 (2014) 2974.*

[HFP05] The ALICE Collaboration *Physics Letters B738 (2014) 97.*

[HFP06] The ALICE Collaboration *Physics Letters B740 (2015) 105-117.*

[HFP07] The ALICE Collaboration *Journals of High Energy Physics 09 (2015) 148* .

[HFP08] The ALICE Collaboration *Physical Review Letters 109, 112301 (2012).*

[HFP09] The ALICE Collaboration *Physics Letters B708 (2012) 265* .

[HFP10] The ALICE Collaboration *Journals of High Energy Physics 01 (2012) 128.*

[HFP11] The ALICE Collaboration *Journals of High Energy Physics 1207 (2012) 19.*

[HFP12] The UA5 Collaboration *Z. Phys C43 (1989) 357.*

[HFP13] The UA5 Collaboration *Journals of High Energy Physics 2010 (2010) 02041.*

[HFP14] The UA5 Collaboration *Physics Letters B738 (2014) 97.*

[HIG01] ATLAS Collaboration Observation of a new particle in the search of the Standard Model Higgs boson with the ATLAS detector at the LHC, *Physics Letters B716, (2012) 1-29.*

[HIG02] CMS Collaboration Observation of a new boson at a mass of 125 GeV with the CMS experiment at the LHC, *Physics Letters B716, (2012) 30.*

[HFP02] The ALICE Collaboration *Journal of Physics: Conference Series 535 (2014) 012012.*

[HXM94] Xin-Nian Wang, Miklos Gyulassy *Computer Physics Commununications 83:307, arXiv:nucl-th/9502021.*

[IAN11] Edmond Iancu. *arXiv:1205.0579 [hep-ph].*

[JAK14] Karl Jakobs. *arXiv:1206.7024 [hep-ex].*

[JPL15] J. P. Lansberg *arXiv:1209.0331v2 [hep-ph].*

[KAR07] Frithjof Karsch. *High Energy Physics - Phenomenology /0701210*, 2007.

[LHC01] ALICE Collaboration. *Journal of Instrumentation*, 3:S08001, 2008.

[LHC12] Alemany *et al. LHC-OP-ES0019 rev 4.0,* 2011.

[LHC98] LHCb Collaboration. *Technical Proposal* Tech. Proposal. CERN, Geneva, 1998.

[MPC01] M. Marchisone, private communication `https://indico.cer.ch/event/443543/contribution/1/attachments/1151653/09Sep2015_pagHFM.pdf`.

[MPT01] T. Sjostrand, S. Mrenna, P. Skands. *Journals of High Energy Physics 2006 (2006) 05 026.*

[MPT02] A. Moraes. *ATLAS Note ATL-COM-PHYS-2009-119 (2009).*

[MPT03] M. G. Albrow *et al. arXiv:hep-ph/0610012v1 (2006).*

[MUSP] Cynthia Hadjidakis. `https://twiki.cern.ch/twiki/bin/viewauth/ALICE/MuonTracking`.

[NAS03] Paolo Nason. *High Energy Physics - Phenomenology /0301003.* 2003.

[OCDB] R. Grosso. `http://aliweb.cern.ch/Offline/Activities/ConditionDB.html#SimulReco`.

[PAC14] Yvonne Pachmayer. *Nuclear Instruments and Methods in Physics Research A766 (2014) 292-295. arXiv:1402.3508 [physics.ins-det].*

[PAL07] Sanjoy Pal. `https://cds.cern.ch/record/1453791`.

[PNP01] C.J. Maxwell. *arXiv:hep-ph/0611120v1 [hep-ph].*

[POL73] H. David Politzer. *Physical Review Letters, 30:1346–1349, 1973.*

[PSH$^+$02] J. Pumplin, D. R. Stump, J. Huston, *et al. Journal of High Energy Physics 07:012*, 2002.

[PRJ96] R.Engel, J.Ranft *Phys. Rev.D54:4244-4262, 1996. arXiv:hep-ph/9509373.*

[PST13] Sjostrand, Torbjorn *et al. Journal of High Energy Physics 0605:026,* 2006.

[RIG13] Francesco Riggi. *European Physical Journal C68 (2010) 345.*

[RNWG07] G. Renault, B.S. Nielsen, J. Westergaard, and J.J. GaardhOJe. *International Journal of Modern Physics, E16:2413–2418*, 2007.

[SCH08] Cynthia Hadjidakis. `https://twiki.cern.ch/twiki/bin/viewauth/ALICE/MuonTracking`,

[SCH09] The ALICE Collaboration *Journals of Physics Conference Series 509 (2014) 012081.*

[SER02] Cicalo, C. `https://cds.cern.ch/record/790000`, 2002.

[SMO] Wikipedia, the free encyclopedia. `https://en.wikipedia.org/wiki/Standard_Model`.

[SQU79] E. J. Squires The bag model of hadrons. *Reports on Progress in Physics 42 1187*, 1979.

[SRA01] Sudhir Raniwala. *Journal of Physics G: Nuclear and Particle Physics 35 (2008) 104165 (4pp),* 2008.

[SW07] Peter Z. Skands and Daniel Wicke. *The European Physical Journal, C52:133–140,* 2007.

[SWO98] D Swoboda. Technical Report *ALICE-INT-1999-06.*, CERN, Geneva, 1998.